UNIVERSITAT POLITÈCNICA DE CATALUNYA
BARCELONATECH
Departament de Teoria del Senyal
i Comunicacions

High-Resolution Space-Borne and Ground-Based SAR Persistent Scatterer Interferometry for Landslide Monitoring

Author

Rubén Iglesias González

Thesis Advisors

Jordi J. Mallorquí Franquet
Xavier Fàbregas Cànovas

A Thesis submitted to the Universitat Politècnica de Catalunya (UPC) in partial fulfillment of the requirements for the degree of DOCTOR OF PHILOSOPHY

Ph.D. program on Signal Theory and Communications
Remote Sensing Laboratory (RSLAB) Group
Barcelona, September 2015

6

Chapter 6
GB-SAR PSI

The way to compensate APS and to improve GB-InSAR performance by means of polarimetric optimization have been introduced in Chapters 4 and 5, respectively. We are now in conditions of presenting the final development of the GB-SAR processing chain to the estimation of the linear component of displacement, but also its non-linear component. Indeed, this development is based on the adaptation of CPT algorithm (seen in Chapter 3) to work with the fully-polarimetric zero-baseline data provided by the RiskSAR sensor.

The content of this Chapter corresponds to the following publications:

R. Iglesias, A. Aguasca, X. Fabregas, J. Mallorqui, D. Monells, C. López-Martínez, and L. Pipia, "Ground-based Polarimetric SAR Interferometry for the Monitoring of Terrain Displacement Phenomena - Part I: Theoretical Description," *Selected Topics in Applied Earth Observations and Remote Sensing, IEEE Journal of*, vol. 8, no. 3, pp. 980-993, Mar. 2015.

R. Iglesias, A. Aguasca, X. Fabregas, J. Mallorqui, D. Monells, C. López-Martínez, and L. Pipia, "Ground-based Polarimetric SAR Interferometry for the Monitoring of Terrain Displacement Phenomena - Part II: Applications," *Selected Topics in Applied Earth Observations and Remote Sensing, IEEE Journal of*, vol. 8, no. 3, pp. 994-1007, Mar. 2015.

The first paper is based on a theoretical description of the whole GB-SAR processing chain. First, a full description of the radar architecture of the RiskSAR sensor, highlighting the main advantages of working with FMCW radars, is given. Then, the different GB-SAR operation modes are described. Once a certain area is selected to carry out a monitoring, two different operation modes, referred to as continuous and discontinuous, may be considered. This choice is translated in different GB-InSAR processing strategies.

For the sake of generality, the processing chain is explained for the more complex case, i.e, under the discontinuous operation mode. The Short-Term Processing (STP) and the Long-Term Processing (LTP) are hence presented in order to explain the main differences between compensating APS over GB-SAR images acquired within the same measurement day or with a certain temporal baseline (roughly a month in this case). Finally, the adaptation of the CPT is presented to the accurate estimation of both, the linear displacement rate and the time-series for GB-SAR measurements.

The second paper presents the application of the GB-SAR processing chain described in the former for the monitoring of *El Forn de Canillo* using the GB-SAR fully-polarimetric data set of *El Forn de Canillo* presented in Section 1.4.3 of Chapter 2. The interferograms employed for the GB-SAR PSI processing are listed in Section G.2 of Appendix G. This part focuses in the more applicable aspects of the processing, such as the measurement logistics or the necessity to project LOS displacements along the real ground displacement direction (introduced in Section 3.5 of Chapter 3). Moreover, the main differences when facing landslide monitoring applications with respect to a standard urban subsidence phenomenon are largely discussed. For that purpose, an example of urban subsidence monitoring over the village of *Sallent*, northeastern of Spain, is studied in detail. A total of 9 X-band fully-polarimetric images, from June 2006 to March 2007, collected by the RiskSAR sensor are employed for this comparison.

As it will be shown, the displacement results obtained show a high agreement with the ground truth data available, thus demonstrating the capabilities of GB-SAR sensors for this type of applications. Compared with PSI space-borne solutions, GB-SAR sensors present several advantages due to the zero-baseline configuration of the instrument. The revisiting-time is no longer a constraint due to the employment of a terrestrial platform. They offer the possibility to fit the illumination angle in order to maximize the detection of real ground displacement in the LOS direction. Finally, and the most important, since APS may be perfectly estimated and compensated for, lower numbers of images are required in order to achieve reliable non-linear estimations of the ground displacement phenomena. Compared with traditional in-field monitoring devices and techniques, including total stations, DGPS, geological mapping, geophysical prospection, topographic leveling, extensometers, inclinometers and piezometers, GB-SAR solutions have demonstrated to provide higher densities and to be very efficient in order to cover larger areas for long periods at lower cost.

ATTENTION ¡

Pages 155 to 182 of the thesis containing the article:

Ground-Based Polarimetric SAR Interferometry for the Monitoring of Terrain Displacement Phenomena

Rubén Iglesias, *Student Member, IEEE*, Albert Aguasca, *Member, IEEE*, Xavier Fabregas, *Member, IEEE*, Jordi J. Mallorqui, *Senior Member, IEEE*, Dani Monells, *Student Member, IEEE*, Carlos López-Martínez, *Senior Member, IEEE*, and Luca Pipia

are available at the editor's web

Part I: Theoretical Description
http://ieeexplore.ieee.org/xpl/articleDetails.jsp?arnumber=6982213

Part II: Applications
http://ieeexplore.ieee.org/xpl/articleDetails.jsp?arnumber=6981929

7

Chapter 7

Selection of Persistent Scatterers by means of TSSC

In the previous Chapter the whole GB-SAR processing chain has been presented for the efficient monitoring of slow-moving landslides by means of GB-SAR PSI techniques. Nonetheless, all the results referred to the GB-SAR case along this PhD work has been addressed to the coherence stability approach. What is the reason for that?

As seen in Section 3.2 of Chapter 3, the reliability of displacement estimation mainly depends on reaching an adequate selection of PSCs. There are mainly two criteria available in the literature for the estimation of pixels' dispersion, these are the coherence stability [22, 26] technique and the PS approach [19]. As seen, the former makes use of the estimated coherence maps from the multi-looked interferograms, which can be directly related with the standard deviation of the interferometric phase. The ML used, which basically consists of applying a boxcar window, reduces the resolution of the interferograms

depending on the averaging factor employed. This fact impacts in the pixel selection step, leading to an inherent reduction of the resolution during the detection of persistent scatterers. For this reason, this approach is typically addressed as low-resolution PSI. The latter relates the phase dispersion of those scatterers presenting high values of SNR with the D_A estimator [19], which basically corresponds to a measure of the pixels' amplitude stability. Pixels stable in amplitude are assumed to be reliable in phase. Since the multi-looking of data is not required in that case, the resolution of the original images is preserved during the detection of PSCs. For this reason, this method is typically addressed as full-resolution PSI.

The choice of the pixel selection criterion basically depends on the number of acquisitions at disposal, on the resolution required and on the nature of the scenario to be monitored. On the one hand, the coherence stability method ensures accurate estimations of the phase statistics even when a reduced number of SAR images is available. In contrast, the PS approach demands a larger number of SAR images to be reliable, typically more than 20 [19]. On the other hand, the coherence stability criterion performs better over environments with predominance of distributed targets, this is when multiple scatterers are present within a resolution cell. In contrast, the PS approach is mainly employed for the detection of deterministic point-like targets, such as man-made structures, which are not affected by geometrical decorrelation and speckle noise as there is a single dominant scatterer within the resolution cell. There is hence a clear limitation when the full-resolution of SAR images requires to be preserved, in order to exploit the point-like scatterers within the the illuminated scenario, and the number of images available is small.

One interesting example arises from the use of GB-SAR sensors when these are employed to carry out a discontinuous monitoring of affected areas, which is the case of this PhD Thesis. As explained, this operation mode consists of revisiting the area of interest during different measurement days at regular intervals and it is typically addressed for the monitoring of slow-displacement rate phenomena, where performing a continuous monitoring is inefficient and costly. In that case, it is usual revisiting the AOI the least possible number of times in order to avoid increasing the cost of the monitoring. In this case, reaching the minimum number of images required by the D_A approach is usually not accomplished, limiting the application of full-resolution PSI.

Another clear example of this appears when SAR images of the so-called new family of X-band SAR sensors, like the German TerraSAR-X and TanDEM-X satellites [53], [54] or the Italian constellation Cosmo-Skymed [56], are ordered for a certain area monitoring. Despite the improved capabilities of these sensors in terms of resolution and revisiting time, the acquisition of products has become considerably more expensive compared with its predecessors, such as ERS-1/2 or ENVISAT. This fact compromises in many cases the acquisition of a large number of SAR images with the lowest time lapses, since it considerably increases the cost of the monitoring and can make PSI techniques to loose a competitive advantage against other surveying techniques. This is clearly the case of monitoring slow-moving phenomena, in which a large number of SAR images acquired in a short period of time do not provide new information. While it is true that the greater the number of images, the better the APS and non-linear displacement component estimation, reliable estimations can be achieved with reduced data sets if the extension of the non-linear displacement is lower compared with the APS correlation window. Finally, it must

be recalled that in presence of large spatial baselines, understanding large as closer to the critical baseline, a big amount of coherence maps under the coherence stability approach turn out some interferograms to be useless due to the geometrical decorrelation [19]. A full-resolution PSI processing results mandatory in all these cases in order to take benefit of the high-resolution provided by these sensors, even when a reduced set of SAR images is available.

In order to overcome this limitation of classical PSI techniques, a new approach based on exploiting the spectral properties of point-like scatterers is presented in this Chapter. This method takes advantage of the so-called Coherent Scatterer (CS), presented in [191], but including the temporal axis in the detection. The rationale is to estimate which targets exhibit a high spectral correlation coefficient along the multi-temporal set of SAR images available. This estimation is referred to as TSSC. Those targets fulfilling this condition will be directly related to as point-like scatterers and, consequently, as persistent scatterers suited for the PSI processing.

The content of this Chapter corresponds to the following publications:

R. Iglesias, J. J. Mallorqui, and P. López-Dekker, "DInSAR Pixel Selection Based on Sublook Spectral Correlation Along Time," *IEEE Transactions on Geoscience and Remote Sensing*, vol. 52, no. 7, pp. 3788-3799, Jul. 2014.

R. Iglesias, D. Monells, C. López-Martínez, J. J. Mallorqui, X. Fabregas, and A. Aguasca, "Polarimetric Optimization of Temporal Sublook Coherence for DInSAR Applications," *Geoscience and Remote Sensing Letters, IEEE*, vol. 12, no. 1, pp. 87-91, Jan. 2015.

The first paper presents the mathematical formulation of the TSSC approach. In this framework, the concept of Stable Coherent Scatterer (SCS) and the different approaches for the TSSC estimation, these are the Temporal Sublook Coherence (TSC) and the Temporal Sublook Entropy (TSE), are widely discussed. The relationship between the values of the TSSC estimator and the pixels' dispersion is studied. The test area selected to evaluate the TSSC performance corresponds to the city of Murcia (Spain), which is an urban area where subsidence has occurred during the last years. For this purpose, a data set of 51 SAR images, corresponding to the German satellite TerraSAR-X and covering the period from July 2008 to April 2010, has been selected. The large number of images available allows a fair comparison of the final SCSs selected with the well-known PS pixel selection approach. In this context, the benefits of performing a joint TSSC-PS full-resolution PSI when the number of images available is adequate is finally put forward.

In the second paper, the new pixel selection technique is validated in the mountainous environment of *El Forn de Canillo* using the GB-SAR fully-polarimetric data set presented in Section 1.4.3 of Chapter 2. This work seeks to demonstrate the goodness of the TSSC estimator over data sets with a reduced number of SAR images. For the first time in this PhD Thesis, a full-resolution PSI is applied over the GB-SAR data set. Furthermore, this work reveals the benefits of extending the TSSC estimator to work with fully polarimetric data. In this framework, the polarimetric optimization methods referred to as Best, SOM, and ESM (presented in Chapter 5) are adapted to work with the TSC approach in order to improve its performance.

ATTENTION ¡

Pages 186 to 204 of the thesis containing these articles are available at the editor's web:

DInSAR Pixel Selection Based on Sublook Spectral Correlation Along Time. Rubén Iglesias, *Student Member, IEEE*, Jordi J. Mallorqui, *Senior Member, IEEE*, and Paco López-Dekker, *Member, IEEE*

http://ieeexplore.ieee.org/xpl/articleDetails.jsp?arnumber=6620942

Polarimetric Optimization of Temporal Sublook Coherence for DInSAR Applications. Rubén Iglesias, *Student Member, IEEE*, Dani Monells, Carlos López-Martínez, *Senior Member, IEEE*, Jordi J. Mallorqui, *Senior Member, IEEE*, Xavier Fabregas, *Member, IEEE*, and Albert Aguasca, *Member, IEEE*

http://ieeexplore.ieee.org/xpl/articleDetails.jsp?arnumber=6827179

8

Chapter 8

Orbital and Ground-Based High-Resolution PSI Results

In the previous Chapter a new full-resolution pixel selection method has been presented. The method is based on the characterization of the degree of correlation between different sublooks of the image spectrum along a multi-temporal set of SAR images. Those targets exhibiting high values of TSSC are directly related to as point-like scatterers and, consequently, as persistent scatterers suited for the PSI processing.

The objective of this Chapter is twofold. On the one hand, demonstrating the applicability of the TSC approach (which is based on the TSSC estimation relying on the coherence estimator) for full-resolution PSI purposes when a reduced number of either

orbital- or ground-based SAR images is available. Up to the moment, the performance of this approach under this restriction has been only demonstrated for the GB-SAR data set. In this context, the estimation accuracy, the number of pixel candidates, and the final PSI displacement maps retrieved are deeply discussed and compared with the classical approaches, i.e, the coherence stability technique and the PS approach, and for both platforms orbital- and ground-based. On the other hand, a final comparison in *El Forn de Canillo* between the down-slope PSI results, obtained with the space-borne and ground-based SAR data sets presented in Section 1.4.3 of Chapter 2, and the ground truth-available, is put forward. In order to demonstrate the goodness of the TSC approach when a reduced number of images is available, and make a fair comparison with GB-SAR results, only ten images of the TerraSAR-X data set have been employed for the analysis presented.

The content of this Chapter corresponds to the following publication:

R. Iglesias, J. J. Mallorqui, D. Monells, C. López-Martínez, X. Fabregas, A. Aguasca, J. A. Gili, and J. Corominas, "PSI Deformation Map Retrieval by Means of Temporal Sublook Coherence on Reduced Sets of SAR Images," *Remote Sensing*, vol. 7, no. 1, pp. 530-563, Jan. 2015.

As it will be shown in the paper, the persistent scatterers selected with the coherence stability and the TSC approach perfectly matches, being both selections associated to the man-made structures and rocky areas present in the scenario. Moreover, both approaches show a similar performance in terms of PSI displacement results. Nonetheless, the resolution loss inherent to the coherence approach will led to a reduced number of pixels compared with the TSC approach. Recall that having higher densities in this type of applications is a key factor. This fact increases the precision on determining the extension of local displacements patterns, such as the area of *Cal Borró-Cal Ponet*, thus easing the characterization of landslides. Contrarily, the PS approach provides slightly higher pixels' densities compared with the TSC approach (roughly a 10 percent more), but at the expense of including outliers in the final PSI results due to the unreliable estimation of the D_A index. In fact, it is a false improvement as the low number of images makes the selection untruthful, as commented in Section 3.2.3 of Chapter 3.

Regarding RiskSAR and TerraSAR-X down-slope PSI results, it will be shown how they provide consistent measurements, compatible with the available inclinometric records in the lower part of the landslide. However, as seen in Chapter 3, the observations collected with TerraSAR-X, with a larger spatial coverage, reveal some displacements significantly higher in the upper part of the slope, defining some unstable rock areas whose existence had remained unnoticed so far. Field surveys have confirmed the presence of activity indicators in this area, such as recent depressions, structural disturbance or open tension cracks, as presented in Section 1.4.3 of Chapter 1.

remote sensing
ISSN 2072-4292
www.mdpi.com/journal/remotesensing

Article

PSI Deformation Map Retrieval by Means of Temporal Sublook Coherence on Reduced Sets of SAR Images

Rubén Iglesias [1], Jordi J. Mallorqui [1,*], Dani Monells [1], Carlos López-Martínez [1], Xavier Fabregas [1], Albert Aguasca [1], Josep A. Gili [2] and Jordi Corominas [2]

[1] Department of Signal Theory and Communications (TSC), Universitat Politècnica de Catalunya (UPC), Jordi Girona 1-3 (D3), 08034 Barcelona, Spain; E-Mails: ruben.iglesias@tsc.upc.edu (R.I.); dmonells@tsc.upc.edu (D.M.); carlos.lopez@tsc.upc.edu (C.L.-M.); fabregas@tsc.upc.edu (X.F.); aguasca@tsc.upc.edu (A.A.)

[2] Department of Geotechnical Engineering and Geosciences, Universitat Politècnica de Catalunya (UPC), Jordi Girona 1-3 (D2), 08034 Barcelona, Spain; E-Mails: j.gili@upc.edu (J.A.G.); jordi.corominas@upc.edu (J.C.)

* Author to whom correspondence should be addressed; E-Mail: mallorqui@tsc.upc.edu; Tel.: +34-934-017-229; Fax: +34-934-017-232.

Academic Editors: Richard Gloaguen and Prasad Thenkabail

Received: 30 July 2014 / Accepted: 15 December 2014 / Published: 7 January 2015

Abstract: Prior to the application of any persistent scatterer interferometry (PSI) technique for the monitoring of terrain displacement phenomena, an adequate pixel selection must be carried out in order to prevent the inclusion of noisy pixels in the processing. The rationale is to detect the so-called persistent scatterers, which are characterized by preserving their phase quality along the multi-temporal set of synthetic aperture radar (SAR) images available. Two criteria are mainly available for the estimation of pixels' phase quality, *i.e.*, the coherence stability and the amplitude dispersion or permanent scatterers (PS) approach. The coherence stability method allows an accurate estimation of the phase statistics, even when a reduced number of SAR acquisitions is available. Unfortunately, it requires the multi-looking of data during the coherence estimation, leading to a spatial resolution loss in the final results. In contrast, the PS approach works at full-resolution, but it demands a larger number of SAR images to be reliable, typically more than 20. There is hence a clear limitation when a full-resolution PSI processing is to be carried out and the number of acquisitions available is small. In this context, a novel pixel selection method based on exploiting the spectral properties of point-like scatterers, referred to as temporal sublook coherence (TSC),

has been recently proposed. This paper seeks to demonstrate the advantages of employing PSI techniques by means of TSC on both orbital and ground-based SAR (GB-SAR) data when the number of images available is small (10 images in the work presented). The displacement maps retrieved through the proposed technique are compared, in terms of pixel density and phase quality, with traditional criteria. Two X-band datasets composed of 10 sliding spotlight TerraSAR-X images and 10 GB-SAR images, respectively, over the landslide of El Forn de Canillo (Andorran Pyrenees), are employed for this study. For both datasets, the TSC technique has showed an excellent performance compared with traditional techniques, achieving up to a four-fold increase in the number of persistent scatters detected, compared with the coherence stability approach, and a similar density compared with the PS approach, but free of outliers.

Keywords: synthetic aperture radar (SAR); differential SAR interferometry (DInSAR); persistent scatterer interferometry (PSI); temporal sublook coherence (TSC); ground-based SAR (GB-SAR); spotlight; persistent scatterer

1. Introduction

Data acquired from synthetic aperture radar (SAR) sensors allows obtaining all-day, all-weather high-resolution complex reflectivity images of large-scale areas. If SAR images are taken at different times, differential SAR interferometry (DInSAR) techniques allow exploiting phase differences, *i.e.*, the interferograms, between multi-temporal pairs of single look complex (SLC) images in order to retrieve the displacement information of affected areas [1,2] with millimetric precision [3]. The exploitation of the interferometric phase is limited by geometrical and temporal decorrelation phenomena [4]. The presence of hard atmospheric artifacts also compromises the applicability of classical DInSAR techniques.

In order to overcome these limitations, different persistent scatterer interferometry (PSI) techniques have been developed during the last decade [5–15]. In this case, large datasets of multi-temporal SAR data are employed in order to generate multiple phase relationships, allowing the reliable estimation of both the linear and the non-linear component of terrain displacements, as well as the atmospheric phase screen (APS) for each acquisition. Nowadays, there exist a lot of applications showing their validity for monitoring large-scale deformation episodes, as well as providing a useful technique for their geophysical interpretation. Examples of such applications include, among others, modeling surface deformation [16–18], glacier monitoring [19], landslides [20], soil compaction rate [21] or atmosphere estimation [4].

As happened with classical DInSAR, the achievable velocity map reliability also depends on the pixels affected by decorrelation phenomena. The displacement information cannot thus be exploited from all pixels within the illuminated scenario, as only a limited number of them, the so-called persistent scatterers, fulfill the phase quality requirements to be included in the PSI processing.

Two main criteria are available for the estimation of pixels' phase quality: these are the coherence stability [12,18] and the permanent scatterer (PS) approach [6]. The former makes use of the estimated coherence maps from the multi-looked interferograms, which can be directly related with the standard deviation of the interferometric phase. The multi-look (ML) used, which basically consists of applying a boxcar window, reduces the resolution of the interferograms depending on the averaging factor employed. This fact impacts the pixel selection step, leading to an inherent reduction of the resolution during the detection of persistent scatterers. For this reason, this approach is typically addressed as low-resolution PSI. The latter relates the phase dispersion of those scatterers presenting high values of signal-to-noise ratio (SNR) with the amplitude dispersion (D_A) estimator [6], which basically corresponds to a measure of the pixels' amplitude stability. Pixels stable in amplitude are assumed to be reliable in phase. Since the multi-looking of data is not required in that case, the resolution of the original images is preserved during the detection of persistent scatterers. For this reason, this method is typically addressed as full-resolution PSI.

The choice of the pixel selection criterion basically depends on the number of acquisitions at disposal, on the resolution required and on the nature of the scenario to be monitored. On the one hand, the coherence stability method ensures accurate estimations of the phase statistics, even when a reduced number of SAR images is available. In contrast, the PS approach demands a larger number of SAR images to be reliable, typically more than 20 [6]. On the other hand, the coherence stability criterion performs better over environments with the predominance of distributed targets; this is when multiple scatters are present within a resolution cell. In contrast, the PS approach is mainly employed for the detection of deterministic point-like targets, such as man-made structures, which are not affected by geometrical decorrelation and speckle noise, as there is a single dominant scatter within the resolution cell. There is hence a clear limitation when the full-resolution of SAR images requires being preserved to exploit the point-like scatters within the the illuminated scenario and the number of images available is small.

A clear example of this appears when SAR images of the so-called new family of X-band SAR sensors, like the German TerraSAR-X and TanDEM-X satellites [22,23] or the Italian constellation Cosmo-Skymed [24], are ordered for area monitoring. During the last few years, this new family of SAR sensors has led to a scientific breakthrough presenting low revisiting times (up to few days) and improved spatial resolutions (up to the meter), which are providing scientists outstanding amounts of unprecedented X-band SAR data. Nonetheless, the acquisition of these products has become considerably more expensive compared with its predecessors, such as ERS-1/2 or ENVISAT. This fact compromises in many cases the acquisition of a large number of SAR images with the lowest time lapses, since it considerably increases the cost of the monitoring and can make PSI techniques lose a competitive advantage against other surveying techniques. This is clearly the case of slow-moving phenomena monitoring, because large numbers of SAR images acquired in a short period of time do not provide new information. In addition, the high-resolution of the images, the shorter swaths and the multiple modes available make these data be acquired "under demand". This implies that it will be very unlikely to have a historical archive of images of a particular area of interest. Finally, it must be pointed out that in the presence of large spatial baselines, understanding large as closer to the critical baseline, a big amount of coherence maps under the coherence stability approach cause some interferograms to be

useless due to the geometrical decorrelation [6]. A full-resolution PSI processing is mandatory in all of these cases in order to benefit from the high-resolution provided by these sensors, even when a reduced set of SAR data is available.

Another interesting example arises from the use of ground-based SAR (GB-SAR) sensors when these are employed to carry out a discontinuous monitoring of affected areas. This operation mode consists of revisiting the area of interest during different measurement days at regular intervals, and it is typically addressed for the monitoring of slow-displacement rate phenomena, where performing a continuous monitoring is inefficient and costly. Once again, improving the performance of full-resolution PSI techniques when a reduced number of GB-SAR images is available is clearly interesting.

In order to overcome this limitation of classical PSI techniques, a new approach based on exploiting the spectral properties of point-like scatterers has been recently presented in [25]. This method takes advantage of the so-called coherent scatterers (CS), presented in [26], but including the temporal axis in the detection. The rationale is to estimate which targets exhibit a high spectral correlation coefficient along the multi-temporal set of SAR images available. This estimation is referred to as temporal sublook coherence (TSC). Those targets fulfilling this condition will be directly related to as point-like scatterers with reliable phases or following the nomenclature used in [25], as temporally stable coherent scatterers (SCS). To date, the application of PSI techniques by means of TSC has been demonstrated for urban subsidence monitoring using a large number of orbital SAR data. In that case, results have shown a similar performance if compared with the PS approach [25].

The objective of this paper is to demonstrate the applicability of the TSC approach for PSI purposes when a reduced number of SAR images is available. The estimation accuracy, the number of pixel candidates and the final PSI displacement maps retrieved are deeply discussed and compared with the classical approaches described above.

The test site selected to demonstrate the feasibility of the TSC approach corresponds to the slow-moving landslide of El Forn de Canillo, located in the Andorran Pyrenees. Applying PSI algorithms over this type of rural scenario, mostly vegetated, constitutes an extra challenge, in contrast with urban areas, where PSI techniques typically perform better. For this purpose, two datasets are employed. On the one hand, 10 sliding spotlight TerraSAR-X images covering the period from October 2010, to November 2011, are used. On the other hand, 10 X-band images collected during the same period with a frequency modulated continuous wave (FMCW) GB-SAR sensor are employed to complete the study. The inclinometric results available for the maximum displacement area of the landslide, known as Cal Boró-Cal Ponet, are used as ground-truth in order to validate the PSI results obtained.

The paper is structured as follows. Section 2 presents a description of the test site and the datasets employed for the study in order to introduce the reader to the context of this work. In Section 3, the sublook generation and TSC estimation processes are briefly reviewed. A comparison between the TSC and the traditional phase quality estimators is presented at this stage. Section 4 shows the relationship between the TSC metrics and the pixels' phase dispersion. A comparison in terms of pixels selected between the TSC and the classical approaches is presented. Section 5 shows the final displacement maps retrieved by means of the TSC approach. These results are deeply discussed and compared with the ones obtained with the classical approaches. In addition, some ground-truth is shown

in order to validate the displacement results retrieved. The main conclusions and major remarks of the manuscript are given in Section 6.

2. Test Site and Dataset

2.1. Test Site

The test site selected to evaluate the performance of the proposed technique corresponds to the area of El Forn de Canillo (located in the geographical coordinates 42.5610 north latitude and 1.6018 western longitude), which constitutes one of the biggest landslides of the Andorran Pyrenees; see Figure 1a.

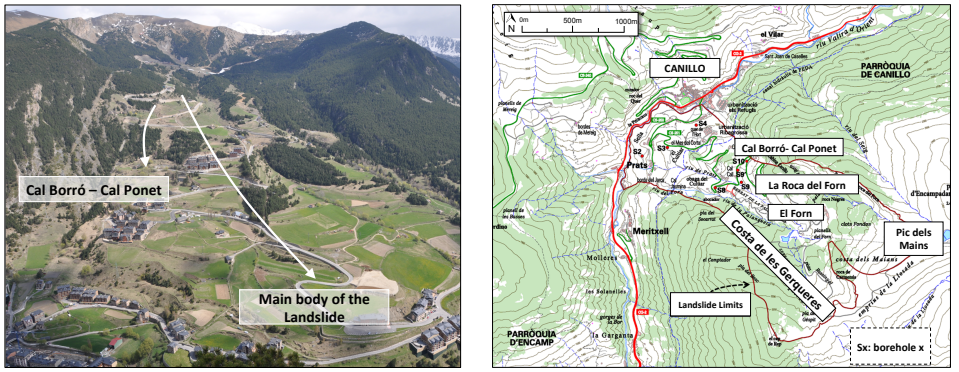

(a) **(b)**

Figure 1. (**a**) General overview of the landslide of El Forn de Canillo; (**b**) landslide limits and location of the in-field monitoring network installed (Points S2 to S10).

The landslide is composed of a sequence of slides and earth-flows with a complex structure, which affects an estimated mass of around 300 Mm^3. In this context, three major sliding units were identified in 1994 by Santacana [27]. The first one corresponds to a slide originated in the area of Pla del Géspit and Costa de les Gerqueres (see Figure 1b), located in the southwest of the landslide, which reached the foot of the hillside. A second unit originated under El Pic de Maians (see Figure 1b) reaching a height of 1640 m, and which overlaps with the previous sliding unit, closing in the Valira River valley. Finally, a new rotational slide with a lower extension originated on the hillside, known as La Roca del Forn (see Figure 1b), in the northeast side of the hillside, has been identified.

The landslide originated due to a decompression phenomenon after the removal of the Valira Glacier, between the years $13,000$ and $16,000$ BP [27]. Throughout the years, the Valira River has been progressively eroding the base of the whole hillside mass without reaching the bedrock, thus originating the landslide [27].

Different observations accumulated during the last few decades have evidenced that the slide mass is still active today, with a residual displacement of few centimeters per year. Concretely, a local failure

in the area, known as Cal Borró-Cal Ponet, located in the northeast extreme of the main body of the landslide, has been recently identified, showing a higher activity coinciding with periods of intense rains and snow melting [28].

In the year 2000, the Andorran authorities promoted several actions for the management of the risk related with the geo-hazard threats associated with landslides, rockfalls and debris flows in the Andorran Pyrenees. Some specific management plans were carried out for the monitoring of El Forn de Canillo. Between the years 2007 and 2009, a network of geotechnical devices, including inclinometers, rod extensometers and piezometers, was installed over the surface of El Forn de Canillo to characterize and understand the dynamics of the landslide. A total of 10 boreholes, referred to as *S2* to *S10* in Figure 1b and reaching a depth between 40 and 60 m, were drilled and equipped with this instrumentation. The measurements provided by these devices have been recently studied with the objective of locating the sliding surfaces and characterizing the displaced material [28].

Unfortunately, some of the boreholes did not reach the needed depth, and consequently, the installed devices did not work properly in some points. Nonetheless, the measurements and observations carried out evidenced that, in addition to a residual movement of the landslide main lobe of some millimeters per year, the most active part corresponds to the secondary landslide of Cal Borró-Cal Ponet, which, between May and June, 2009, registered a velocity up to roughly 2 cm/month [28]. Intense sudden rain events and snow melting were observed during this period. Only those inclinometers reaching the needed depth continue working to date. This is the case of the one referred to as *S10*, located in the maximum displacement rate area of Cal Borró-Cal Ponet, which will be employed to validate the PSI results obtained in this work.

Finally, 3 GB-SAR campaigns carried out by the Institute of Geomatics (Spain) monitored a network composed of 15 corner reflectors over the area of Cal Borró-Cal Ponet. They covered a period of 57 days during fall, 2009, and registered displacements up to 14 mm [29]. This work concluded with the necessity of employing long-term remote sensing studies for the management of the risk related with the landslide of El Forn de Canillo.

2.2. Dataset

In light of all of this evidence, the use of both orbital and ground-based PSI techniques were planned in 2011. The reasons were two-fold. On the one hand, most of the geotechnical devices installed over the landslide surface did not work properly, providing unreliable measures, thus hindering the characterization of the landslide extension and dynamics. On the other hand, conventional geotechnical field measurements present lower densities and worse coverage compared with SAR techniques, which is a key factor in landslide characterization. In this framework, the remote sensing laboratory (RSLab), in collaboration with the Department of Geotechnical Engineering and Geosciences of the Universitat Politècnica de Catalunya (UPC), carried out a one-year monitoring work, from October 2010, to November 2011, employing SAR images acquired with the TerraSAR-X space-borne sensor in sliding spotlight mode and with the UPC's GB-SAR system, referred to as RiskSAR-X. The RiskSAR-X sensor focused on the urbanized area of the landslide, located at the lower part of the sliding mass where the

geotechnical devices were installed, while the sliding spotlight TerraSAR-X images covered the whole landslide extension.

Some important decisions, such as the orbit pass or the GB-SAR location, need to be further commented on at this point. These aspects are especially important in landslide monitoring applications that typically occur in steep topography scenarios, in which the acquisition geometry plays an important role. Minimizing the geometrical distortion effects of SAR imaging and maximizing the detection of the real ground displacement are key factors in order to improve the performance of PSI techniques. The former influences the area illuminated by the SAR sensor and, consequently, the quantity of useful information collected by it. The latter is related to the fact that SAR systems are only able to detect displacements in the line-of-sight (LOS) direction.

Three geometric distortions are present in SAR imaging regardless of the platform nature: the foreshortening, the layover and the shadowing [4]. For the current polar-orbiting SAR orbital sensors, the look direction is either east or west, for the ascending or descending pass, respectively. For this reason, SAR sensors only are able to detect movements along slopes facing either east or west and are almost insensitive to movements in the north or south directions. Since the landslide of El Forn de Canillo is facing west, the descending pass was finally selected to avoid foreshortening and layover phenomena in the illuminated area.

Moreover, it must be taken into account that SAR systems only have sensitivity to detect displacements in the LOS direction. For this reason, detected displacements are rarely the real ones, but a projection of them. In landslide applications, the more realistic assumption regarding the displacement direction consists of considering that it is produced along the steepest gradient of the slope. Again, the descending pass resulted in being more suited for this scenario, since the projection factor between the real displacement and the LOS directions was lower compared with the one provided by the ascending mode.

Unlike space-borne SAR sensors, which are constrained by the orbit pass, GB-SAR sensors allow fitting the sensor location and illumination angle to the specific characteristics of the area of interest. In order to minimize the foreshortening and to maximize the detection of the ground displacements considering that the slide moves along the steepest gradient of the terrain slope, the RiskSAR-X sensor was finally located at the foot of the landslide, 100 m away from the slope. Furthermore, this emplacement also minimized the shaded areas in the SAR images collected. In order to ensure a millimetric repositioning of the instrument to avoid a later co-registration of the data, the system was mounted over a cement base reinforced with a lightweight metallic frame. The RiskSAR-X system was placed on a base at approximately 30 centimeters above the ground to elevate the rail and reduce the impact of the nearby vegetation.

Figure 2 shows a Google Earth image indicating the TerraSAR-X coverage, the area of interest selected for the orbital PSI processing, the RiskSAR-X location and the area illuminated by the GB-SAR sensor. Figure 3a shows a panoramic view of El Forn de Canillo seen from the RiskSAR-X point of view, which is represented in Figure 3b.

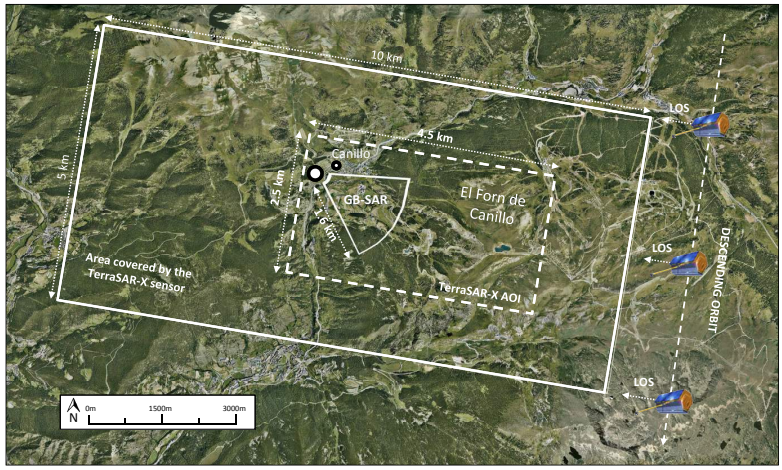

Figure 2. Coverage of the TerraSAR-X and RiskSAR-X sensors over the area of El Forn de Canillo. The solid rectangle indicates the TerraSAR-X coverage: 10 km in range per 5 km in azimuth with a heading of 9.8° with respect to the north. Upper left (42.5896° latitude, 1.5450° longitude), upper right (42.5746° latitude, 1.6649° longitude), bottom left (42.5452° latitude, 1.5348° longitude) and bottom right (42.5302° latitude, 1.6548° longitude). The dashed rectangle indicates the area of interest selected for the orbital PSI processing: 4.5 km in range per 2.5 km in azimuth. The RiskSAR-X location is indicated with the white dot (42.5653° latitude, 1.5921° longitude). The area illuminated by the GB-SAR sensor is indicated with the solid line within the dashed rectangle: 500 m in height, 1600 m in range and 1000 m in width, with a heading of 32° with respect to the north.

(a) **(b)**

Figure 3. (**a**) Panoramic view of El Forn de Canillo from (**b**) the RiskSAR-X point of view.

Regarding the RiskSAR-X characteristics, it is based on the usage of a digital direct synthesizer (DDS) chipset that generates a high rate linear frequency modulated continuous wave (LFM-CW) signal. With this architecture philosophy, the RiskSAR-X sensor is able to perform fast scans, minimizing the effect of troposphere disturbances and reducing the possible amplitude and phase distortions due to target instabilities during the scanning time. Each scan takes approximately from 1 to 2.5 min in single and

fully-polarimetric modes, respectively. The range resolution of the RiskSAR-X sensor is 1.25 m, and as in all GB-SAR sensors, the azimuth or cross-range resolution (the term which is more often employed in GB-SAR geometry) is not constant, ranging from 0.75 m at a near range up to roughly 5 m at the far range of 1500 m. Table 1 presents the sensor setting parameters used during the measurements.

Table 1. RiskSAR-X and Sliding Spotlight TerraSAR-X setting parameters.

RiskSAR-X		**TerraSAR-X (Sliding Spotlight Mode)**	
Sensor Parameter	**Magnitude**	**Sensor Parameter**	**Magnitude**
Carrier Frequency	9.65 GHz	Carrier Frequency	9.65 GHz
Sampling Frequency	81 MHz	Incidence Angle	20–55°;
Pulse Repetition Frequency	20 KHz	Pulse Repetition Frequency	8.2 KHz
Bandwidth	120 MHz	Bandwidth	150 MHz
Deramped Signal Bandwidth	40 MHz	Slant Range Resolution	1.2 m
Transmitted Power	27 dBm	Azimuth Resolution	1.1 m
3dB Antenna Beamwidth	27°	Range Scene Size	10 km
Range Time-Average Factor	128	Azimuth Scene Size	5 km
Synthetic Aperture Length	2 m	Frequency Modulation Rate	*ca.* −5700 Hz/s
Scanning Time: Single-Pol / PolSAR	1/2.5 min	Zero Doppler Scene Duration	3.2 s

The employment of TerraSAR-X images in sliding spotlight is commented on in the following. As stated above, the new family of X-band sensors are demonstrated to improve the monitoring capabilities over man-made structures, such as buildings, bridges, railways and highways, but also over natural corner reflectors, such as rocky areas or bare surfaces. This is directly related to their high spatial resolution, but also to their shorter revisit time, allowing a significant improvement in the temporal and spatial sampling for geo-hazard assessment. The use of the spotlight mode [30] offers a resolution improvement in the azimuth direction (up to 1 m) with respect to the conventional strip-map mode by sweeping the azimuth beam during image acquisition. As will be shown, this resolution improvement will reveal major details, allowing maximization of the detection of persistent scatters. The main characteristics of the TerraSAR-X system in spotlight mode are reported in Table 1.

Since it is well-known that the landslide of El Forn de Canillo is quite stable nowadays, with only some residual movement of the order of 1–3 cm per year, continuous monitoring was considered unfruitful. For this reason, a total of 10 acquisitions collected at the X-band, with a temporal baseline of approximately one month, were finally carried out for both sensors; see Table 2. Notice that the temporal span during the winter is slightly greater. This was done in order to avoid acquiring images when the scenario was covered by snow. The resulting dataset at disposal represents thus a perfect test bed to demonstrate the benefits of employing the TSC approach in the PSI framework when a reduced number of SAR images is available.

Table 2. Timetable of the RiskSAR-X measurements campaigns and the TerraSAR-X acquisitions.

RiskSAR-X Dataset						TerraSAR-X Dataset		
Campaign	**Date**	**Start Time**	**Stop Time**	**No. of Scans**	**Polarization**	**Acquisition**	**Date**	**Polarization**
1	21 October 2010	09:57	12:08	15	HH HV VH VV	1	18 November 2010	HH
2	18 November 2010	17:04	19:13	24	HH HV VH VV	2	29 November 2010	HH
3	9 February 2011	17:00	19:48	33	HH HV VH VV	3	14 February 2011	HH
4	7 April 2011	18:17	23:30	60	HH HV VH VV	4	21 April 2011	HH
5	6 May 2011	10:02	11:47	22	HH HV VH VV	5	13 May 2011	HH
6	25 May 2011	16:09	20:08	50	HH HV VH VV	6	15 June 2011	HH
7	9 June 2011	13:20	16:32	51	HH HV VH VV	7	18 July 2011	HH
8	5 July 2011	08:25	12:24	52	HH HV VH VV	8	20 August 2011	HH
9	6 September 2011	11:49	04:05	88	HH HV VH VV	9	22 September 2011	HH
10	5 October 2011	11:57	16:42	66	HH HV VH VV	10	14 October 2011	HH

Finally, some remarks about the area of interest should be briefly commented. As seen in Figure 1a, El Forn de Canillo is mostly vegetated, containing only some bare surfaces and man-made structures suitable for PSI purposes. Figure 4 illustrates the impact of these characteristics on the amplitude of SAR acquisitions. The figure shows the amplitude of the backscattered signal covering the lower part of the landslide of El Forn de Canillo collected by the RiskSAR-X sensor, expressed in both cartesian (Figure 4a) and polar coordinates (Figure 4b), and the amplitude of the SAR images acquired with the TerraSAR-X sensor operating in spotlight mode corresponding to the whole sliding mass (Figure 4c). This figure evidences the improvement in spatial resolution achieved by the second generation SAR sensors, in particular by the X-band systems working in spotlight mode, which are making SAR images more and more geometrically comparable to optical ones, showing impressive details of the illuminated areas. A poorer spatial resolution may be appreciated for GB-SAR acquisitions mainly due to the cross-range resolution degradation in the far range. Despite this, the man-made structures, bare surfaces and rocky areas may be identified (blue arrows in Figure 4), showing high amplitude levels. Notice also how some forested areas also exhibit high values of back-scattered signal (red arrows in Figure 4). The lower values of amplitude correspond to crop fields, heavy grass areas, shrubberies, *etc*. All of the algorithms explained in this paper are addressed for the polar coordinates reference system.

The fast temporal decorrelation phenomenon present at the X-band over this type of vegetated scenario represents an extra challenge to PSI techniques. The presence of large forested and vegetated areas make difficult the task of obtaining a sufficient network of high-quality phase scatterers for the later reliable displacement map retrieval. In contrast, these complex characteristics of El Forn de Canillo will allow one to easily verify the performance of the SCSs selected, which should correspond with the man-made structures, rocky areas and bare surfaces present in the illuminated area.

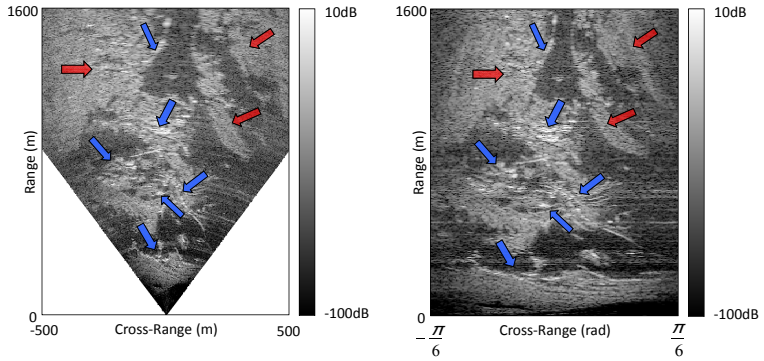

(a) **(b)**

(c)

Figure 4. Amplitude in dB covering the lower part of the landslide of El Forn de Canillo of a SAR image collected by the RiskSAR-X sensor in (**a**) cartesian and (**b**) polar coordinates. The blue arrows refer to man-made structures, while the red arrows refer to high-reflectivity areas related to forested areas, which decorrelate fast at the X-band. (**c**) Amplitude in dB of a SAR image collected by the TerraSAR-X sensor in sliding spotlight mode covering the whole sliding mass.

3. Sublook Generation and Temporal Sublook Coherence Evaluation

This Section presents a brief review of the TSC approach in order to ease the comprehension of the rest of the manuscript. The maps obtained by means of TSC are compared with the traditional phase quality estimators for the GB-SAR and TerraSAR-X datasets described in the previous section.

The objective of the TSC approach is to find the so-called SCS, which refers to those targets that behave as point-like scatterers in terms of the spectrum properties throughout the whole multi-temporal set of SAR images available [25]. This means looking for those targets characterized by a high correlated spectrum in range, azimuth and height for all of the acquisitions. Since some scatterers usually present a non-uniform azimuth scattering pattern, the assumption of the correlated spectrum is typically applied only in the range direction [26].

Working with the spectral properties of point-like scatterers presents clear advantages [25]. In contrast to the PS approach, the TSC is not affected by the possible amplitude fluctuations of point-like scatterers along the temporal axis. The amplitude, thus, plays no role in the TSC estimation, and for this reason, a radiometric calibration of data is not required. Moreover, the resolution of the images is better preserved in comparison with the coherence stability pixel selection approach. Only a loss of a factor of two is produced in the range direction due to the sublook generation process [26]. This resolution loss may be partially overcome using the spatial variant apodization (SVA) filtering technique, as suggested in [25,31]. Finally, due to the nature of the estimator, which is based on exploiting the coherence between different sublooks of the image spectrum, it allows reliable full-resolution detection capabilities, even when a few number of SAR images are at our disposal, as will be demonstrated throughout this manuscript.

The TSC evaluation requires, beforehand, a sublook generation process. A sublook may be defined as a spectrum portion of the full available system bandwidth. This process can be summarized in the following points [26]:

- First of all, the SLC spectrum must be unweighted. SAR images are typically filtered with linear windows in order to reduce the impact of side-lobes. Taking the sublooks directly from the tapered spectra may lead to unbalanced distributions of energy in the sublooks, which could have a negative impact during the later TSC evaluation.
- Once the image spectrum is unweighted, it is divided into two non-overlapping sublooks, which, at the same time, are base-banded to the same center frequency. This step is carried out in order to avoid linear phase terms during the TSC evaluation.
- Each sublook spectrum may be additionally weighted to reduce the side-lobes in the detection.
- An inverse Fourier transform is finally applied to each sublook in order to obtain them in the spatial domain.

Once the sublooks of each image are calculated, the TSC may be evaluated in order to detect SCS, which are directly related to the deterministic point-like scatterers within the area of interest.

Since a pixel-wise product in the space-domain translates into a spectrum correlation in the frequency-domain, the TSC is estimated employing the coherence estimator through the temporal axis among the sublook collections available [25]:

$$T\hat{S}C(i,j) = \frac{\left| \sum_{n=1}^{N_{im}} SL_1(i,j,n) \cdot SL_2^*(i,j,n) \right|}{\sqrt{\sum_{n=1}^{N_{im}} |SL_1(i,j,n)|^2 \cdot \sum_{n=1}^{N_{im}} |SL_2(i,j,n)|^2}} \tag{1}$$

where SL_1 and SL_2 are the complex values from two pixels (i, j) of the first and the second sublook for each acquisition image n, and N_{im} refers to the total number of images. Notice how the spatial averaging used in the traditional approach [26] is now replaced by a temporal averaging [25]. Figure 5 represents the sketch of the TSC flow chart for a generic pixel (i, j).

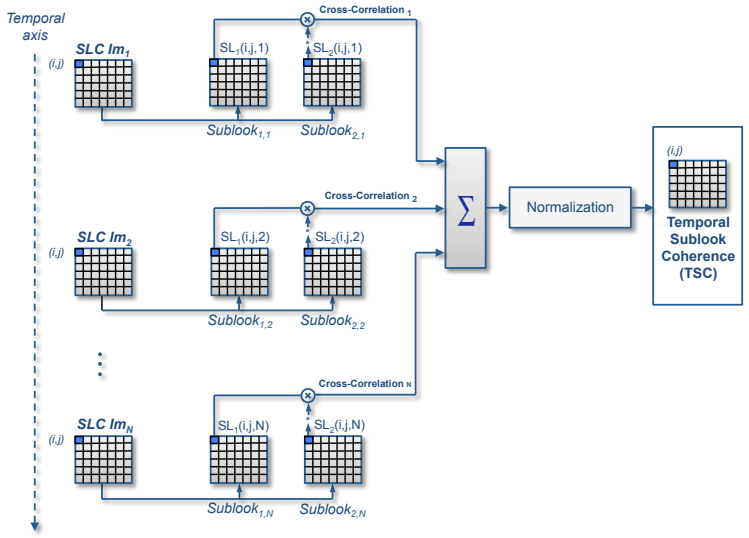

Figure 5. Sketch of the TSC flow chart for a generic pixel (i, j).

Those targets exhibiting high values of TSC within the area of interest, will be directly referred to as SCSs and, consequently, will belong to the final selection of high-quality pixel candidates, or persistent scatterers, for the PSI processing [25].

At this stage, the accuracy of the TSC estimation needs to be commented on in further detail. The reliability of the TSC estimation depends on the number of independent samples involved in the estimation, *i.e.*, the number of images [25]. In fact, the mathematical formulation to characterize the TSC estimation accuracy is totally equivalent to the one developed by Touzi and Lopes in [32] for the classical coherence estimator. The only difference is that now, the spatial averaging is replaced by a temporal one, as indicated above. The probability density function of the TSC magnitude estimator may hence be expressed as a function of the 'true' TSC absolute value and the number of temporal samples involved in the estimation [32]; see Figure 6. As happens with the coherence estimator, the TSC is a biased estimator. Its value is overestimated for low magnitudes of the 'true' TSC values and/or when the number of temporal samples, *i.e.*, the number of SAR acquisitions involved in the estimation, is low. Since the estimation bias is smaller for high values of TSC, where the thresholds are typically set to detect the SCSs, a reliable estimation may be obtained even when a relatively reduced number of SAR images, around 10, is available. This fact provides the TSC estimator a competitive advantage with respect to the PS approach, which requires a larger number of images, typically more than 20, to reach reliable estimations of the D_A and, therefore, of the phase statistics.

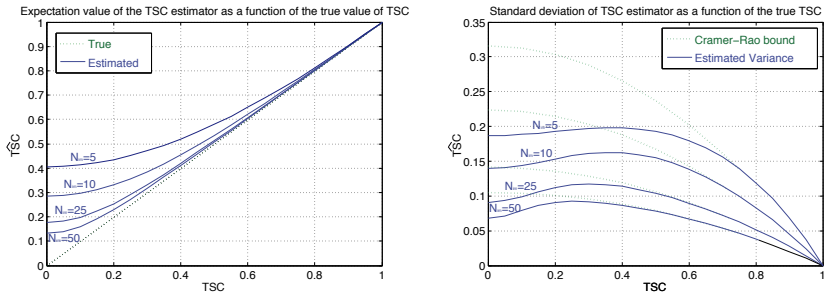

(a) **(b)**

Figure 6. (**a**) Expectation value and (**b**) standard deviation of the TSC estimation as a function of its "true" value, for different numbers of images.

Figures 7 and 8 illustrate the performance of the TSC approach compared with the traditional phase quality estimators for both the ground-based and the orbital datasets described in Section 2, respectively. Figure 7a shows the TSC estimation, while Figure 7a,b shows the temporal mean coherence and the D_A maps, respectively, for the GB-SAR dataset. In parallel, Figure 8a,b,c show the same maps for the TerraSAR-X dataset. Since low D_A values correspond to the highest quality pixels, the color bar has been inverted for the latter. In addition, it is worth mentioning that when using large ML windows, especially with the new family of high-resolution X-band SAR sensors, many stable point-like targets surrounded by non-coherent clutter are unfortunately lost. In order to use the coherence estimator to make a cross-check with the other techniques, a 5×5 ML window has been used to preserve as much as possible the original resolution of images. This ML factor shows a good trade-off between the reliability of the coherence estimator and the preservation of the spatial resolution.

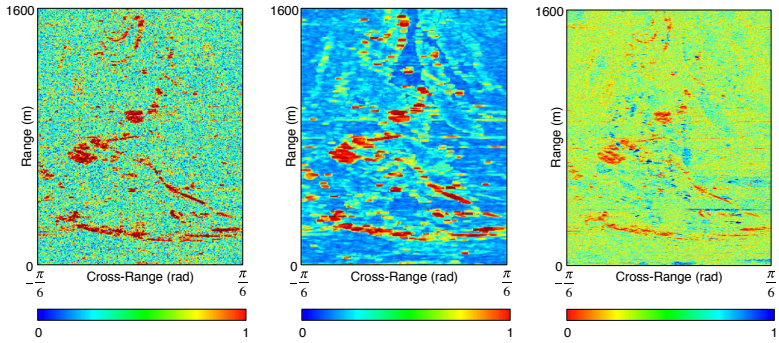

Figure 7. (**a**) TSC; (**b**) mean coherence; and (**c**) D_A maps over El Forn de Canillo test site for the GB-SAR dataset.

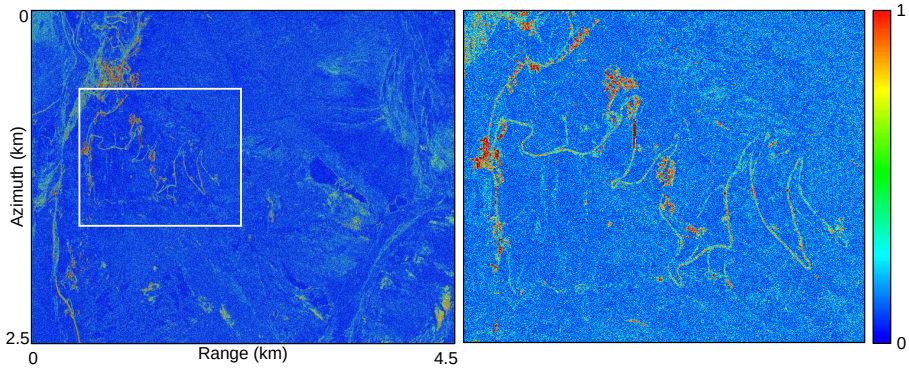

(a)

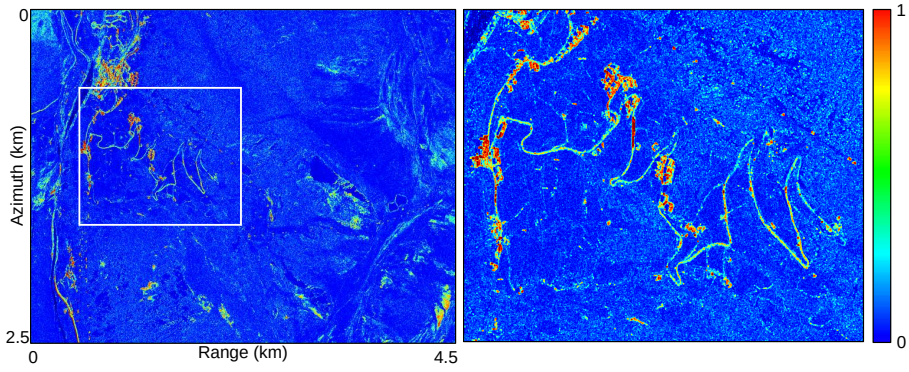

(b)

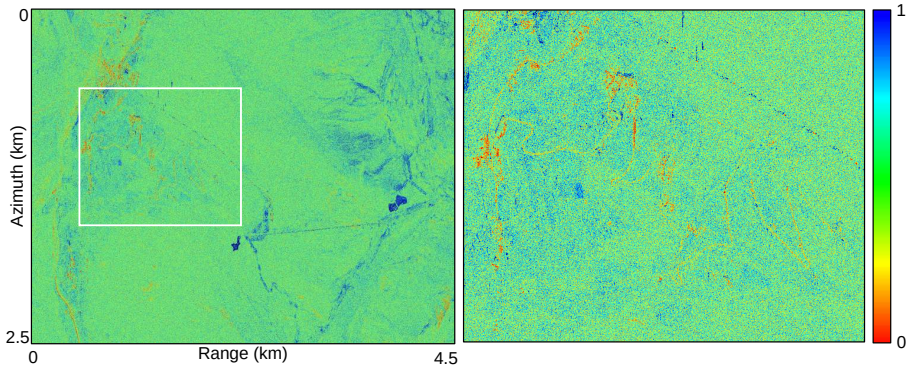

(c)

Figure 8. (**a**) TSC; (**b**) mean coherence; and (**c**) D_A maps over El Forn de Canillo test site for the sliding Spotlight TerraSAR-X dataset. The figures on the right represent a zoom of the area highlighted with a white rectangle in the figures on the left.

As seen before, El Forn de Canillo is mainly a vegetated area only containing a few man-made structures and rocky areas suitable for the PSI processing. In general, the highest quality points detected from all of the estimators correspond with these areas (reddish hue regions). All estimators follow the road, the buildings and the rocky and bare surfaces present in the area of interest for both sensors.

Going into further detail, some considerations deserve special attention. Notice how Figures 7b and 8b evidence the loss of spatial resolution when employing the mean coherence approach. Despite the reduced ML factor employed (5×5), the resolution loss is evident for both sensors. This fact will lead to a significant loss of pixels and details in the later PSI processing, as shown later. Despite this negative aspect, notice how the ML carried out during the coherence estimation reduces the interferometric phase noise, and this fact is translated into a better identification of the persistent scatterers available with respect to the other estimators, which work at full resolution. Due to the intrinsic low-pass filtering related with the ML carried out during the coherence estimation, this approach shows the "cleanest" results. However, this does not mean that some high-quality points surrounded by non-coherent clutter have been lost. Furthermore, Figures 7c and 8c show how the D_A estimator exhibits the worse performance in terms of detection capabilities. In general terms, the D_A estimator presents low values on the man-made structures, as it should be, but also on some low-quality vegetated regions, if compared with the TSC approach. This fact is more noticeable in the TerraSAR-X dataset, where the road in Figure 8c is hardly recognizable, presenting surrounding pixels with low D_A values. Notice how the TSC estimator better preserves the details and presents a better contrast between high-quality and low quality areas. As seen hereinafter, this fact will prevent the inclusion of outliers if the pixel selection thresholds are relaxed in order to improve the pixels' density. This strategy is typically employed to obtain a sufficient network of pixels for reliable PSI processing when the number of high-quality pixels is low, as is the case of this work.

4. Phase Statistics and Pixel Selection Candidates

In order to to establish an adequate threshold to carry out a pixel section of persistent scatterers, the relationship between the TSC metrics and the pixels' phase standard deviation should be calculated. As indicated in [25], this relationship may be obtained through the following simulation. First, a deterministic point-like scatterer is simulated in the spectrum domain, generating an ideal flat-shape function of unitary amplitude. This spectrum is hence corrupted by adding uncorrelated complex circular Gaussian noise in order to degrade its quality. The process is repeated for each image of a simulated dataset. At this point, the standard deviation of the added noise is gradually incremented from 0.05 to 0.95, and for each case, 5000 realizations are performed. The TSC is then calculated, and finally, the spectrum is inverse transformed to the temporal domain in order to evaluate the mean and temporal standard deviation of the target's phase [25].

Figure 9a,b shows the relationship between the estimated TSC and the pixels' phase standard deviation considering 10 images and 30 images, respectively. As seen in the analysis carried out during the estimation accuracy (Figure 6), a larger number of samples involved in the estimation yields to smaller error bars in the phase statistics estimation.

In order to establish equivalent thresholds during the pixel selection step and, thus, make a fair comparison among all methods, the same relationship is calculated for the coherence stability and the D_A approaches, as follows. Figure 9c illustrates the relationship between the estimated coherence and the phase standard deviation following the formulation presented by Touzi and Lopes in [32]. Likewise, Figure 9d,e, shows the relationship between the phase standard deviation and the amplitude dispersion index D_A derived by the numerical simulation stated in [6] considering 10 and 30 images being available, respectively. The values of dispersion in the estimation are represented by the vertical bars, while the solid line represents its mean value. Notice how, again, the quality of the D_A estimation depends on the number of images available, the error bars for the case of having 10 SAR images available being considerably larger.

At this stage, all estimators have been related to the target's phase statistics. An adequate threshold may now be established in order to ensure a specific phase stability during the PSI processing.

Figures 10 and 11 show a comparison in terms of pixels selected between the TSC approach and the classical techniques for the GB-SAR and the TerraSAR-X datasets, respectively. In order to ensure a fair comparison, equivalent thresholds over the phase quality estimators have been established in order to provide the same requirements in terms of phase dispersion according to Figure 9. A threshold of 0.82, which corresponds to a phase standard deviation of roughly 15° (see Figure 9a) has been fixed to the TSC approach. In parallel, a threshold of 0.65 considering a 5×5 ML [32] (see Figure 9c) has been fixed to the mean coherence, and finally, a threshold of 0.25 has been applied to the D_A [6] (see Figure 9d) to produce the same response in terms of phase standard deviation. Figure 12 gives the same information in terms of the number of pixels selected. Notice how the pixels selected with the coherence and the TSC approach correspond with the persistent scatterers present in the area of interest for both datasets, since they perfectly fit the road, the man-made structures and the few rocky and bare surfaces within the illuminated scenario. Notice the resolution loss inherent to the coherence approach, which leads to a reduced number of pixels compared with the TSC and D_A approaches (roughly four-times less). As expected from the study carried out in the previous section, the PS approach provides a greater number of selected pixels (roughly 10 percent more), but including a significant amount of unreliable ones selected over vegetated areas, which are characterized by a high phase dispersion index; see Figures 10 and 11. As seen, the reduced number of SAR images available yields to a poor D_A estimation. At this time, it may be thought that this large number of unreliable pixels identified could be reduced restricting the D_A threshold to lower values, which is only partially true. Figure 11d corresponds to the selection of pixel candidates for the TerraSAR-X dataset employing a more restricted D_A threshold (0.15, which corresponds to 10^o of phase standard deviation). Indeed, almost all of the outliers have disappeared, but the density over the persistent scatterers available has been also drastically reduced. The road and the man-made structures clearly identified in Figure 11a,b are now diluted and hardly detected.

The study carried out in this section evidences once more that a minimum number of 20 images is required in order to produce a reliable D_A estimation. Contrarily, the TSC approach performs well, even when a small dataset of SAR images is available.

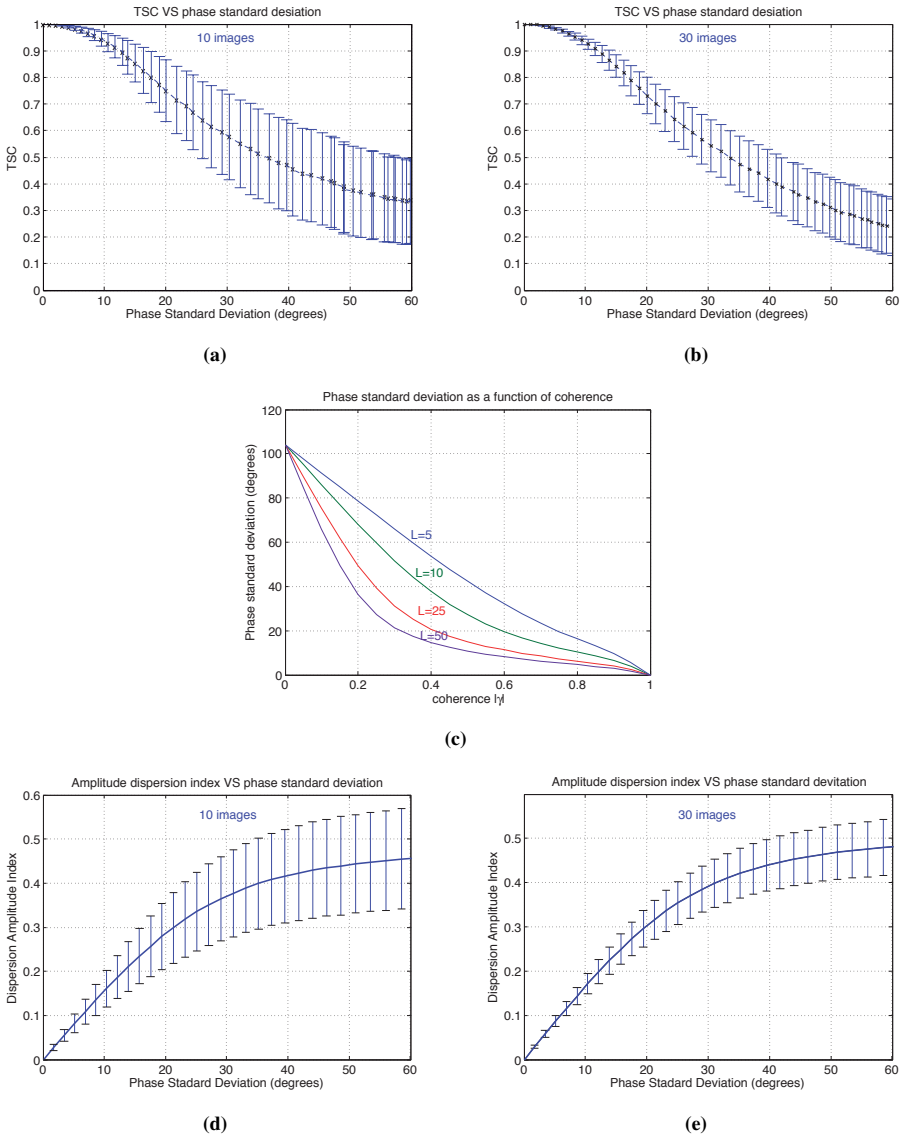

Figure 9. Relationship between TSC and phase standard deviation considering (**a**) 10 and (**b**) 30 SAR images; (**c**) phase standard deviation as a function of coherence for different numbers of multi-look (ML) factors; comparison of the amplitude dispersion index D_A and the phase standard deviation (in degrees) as a function of noise computed by numerical simulation considering (**d**) 10 and (**e**) 30 SAR images available.

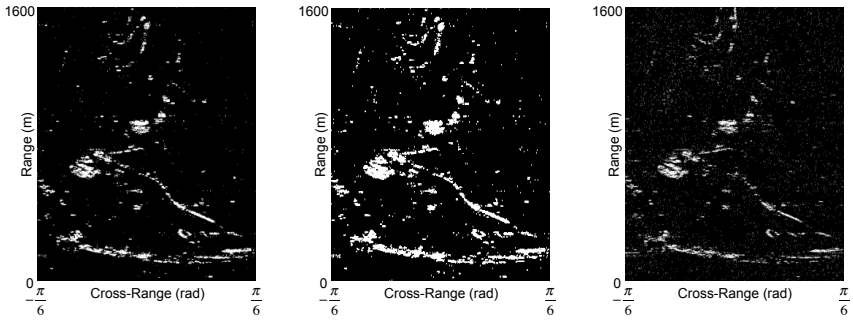

Figure 10. Pixel candidates selected using (**a**) the TSC with a threshold of 0.82; (**b**) the coherence stability with a threshold of 0.65; and (**c**) the D_A with a threshold of 0.25 for the GB-SAR dataset.

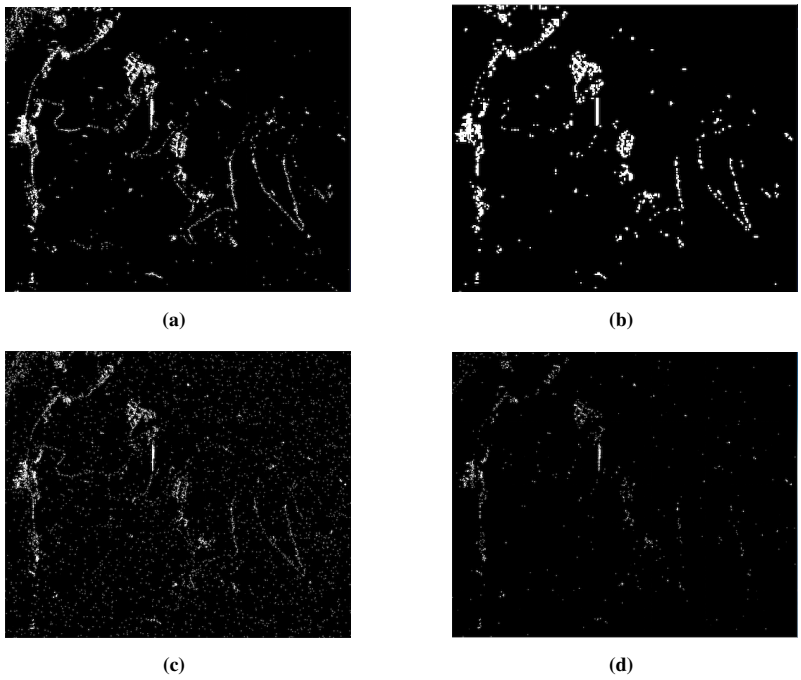

Figure 11. Pixel candidates selected using (**a**) the TSC with a threshold of 0.82; (**b**) the coherence stability with a threshold of 0.65; and the D_A with a threshold (**c**) of 0.25 and (**d**) of 0.15 for the TerraSAR-X dataset.

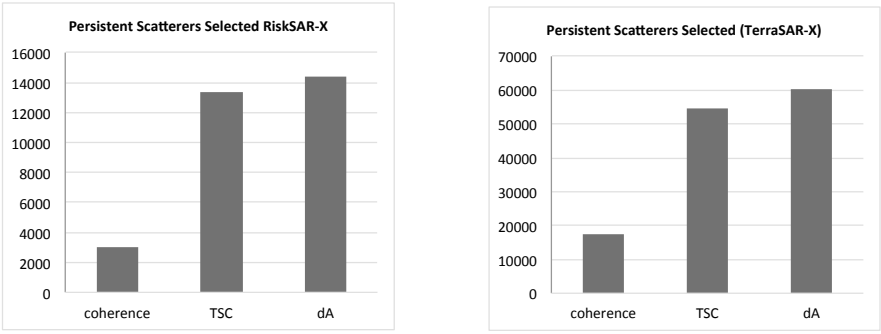

(a) **(b)**

Figure 12. Number of pixel candidates selected using the TSC, the coherence stability and the D_A approaches for (**a**) the GB-SAR and (**b**) the TerraSAR-X datasets.

5. PSI by Means of TSC: Results and Discussion

This section presents the PSI displacement maps obtained with the TSC approach on the test site corresponding to the landslide of El Forn de Canillo for the GB-SAR and the TerraSAR-X datasets described in Section 2. A close comparison, in terms of pixel density and phase quality, with the traditional coherence stability and D_A approaches, is put forward. Finally, some ground-truth data are also presented in order to validate the PSI results obtained.

Beforehand, some remarks about GB-SAR and sliding spotlight interferometry are briefly introduced. The principal steps of the coherent pixel technique (CPT) technique are also reviewed in order to ease the comprehension of the PSI displacement retrieval process employed in this study.

5.1. Interferometric Processing Chain Considerations and CPT Overview

5.1.1. GB-SAR Interferometry

Prior to applying any PSI technique, a pre-processing of GB-SAR data must be carried out in order to improve the quality of the SAR images corresponding to each measurement day and to compensate for the APS present in the long-time interferograms corresponding to the different measurement campaigns.

Considering a total of N daily datasets, each one composed of M_i zero-baseline GB-SAR raw images, with $1 \leq i \leq N$, the process may be summarized in the following two blocks [33]:

- The first block, referred to as short-term processing (STP) [33], basically consists of two steps. The first one is based on carrying out the focus of the raw data. On the one hand, since the RiskSAR-X sensor is based on a LFM-CW radar, the range compression can be carried out with a simple FFT of the time-domain deramped received signal [34,35]. On the other hand, since the cross-range resolution is not constant due to the limited length of the synthetic aperture of GB-SAR sensors, the back-projection technique proved to be the most suited for the azimuth focusing [34].

Once the images has been focused, a temporal averaging of each daily dataset, composed of M_i zero-baseline acquisitions corresponding to the same measurement day i, is carried out in order to improve the SNR of time-stationary targets, leading to a higher quality time-averaged SLC image from each daily dataset corresponding to each measurement campaign. For the dataset used in this paper, 10 time-averaged SLC images will be finally available after this step.

- The following step, referred to as long-term processing (LTP), consists of compensating for the APS present between the different time-averaged SLC images obtained in the previous STP block. From all of the methods available in the literature [33,36–38], the RiskSAR-X makes use of model-based solutions [33]. This kind of solution proved to be very effective, reaching very good performances with no use of extra meteorological data or stable ground control point (GCP) information. The APS estimation and compensation process is a key issue in GB-SAR processing in order to obtain a reliable set of APS-free interferograms suitable for the PSI processing. For the dataset used in this paper, 45 APS-free interferograms are finally available. Finally, to face temporal decorrelation phenomena and enhance the phase quality of interferograms, the processing can be benefited by the exploitation of polarimetric information, such as the one provided by the RiskSAR-X sensor. In classical PSI, only a single-polarimetric channel is considered for the processing. This means that all pixels involved in PSI algorithms belong to the same polarimetric channel. In this context, polarimetric optimization techniques may be employed in order to improve the phase quality of interferograms [39].

5.1.2. Spotlight SAR Interferometry

The azimuth resolution of a SAR image is mainly determined by the characteristics of the azimuth radiation pattern of the antenna. In the conventional strip-map mode, the resolution is roughly half the azimuth length of the antenna and the processing parameters, Doppler centroid and Doppler rate, are azimuth invariant. In this context, the antenna length cannot be arbitrarily reduced without the risk of causing azimuth and/or range ambiguities.

In the sliding spotlight mode, the antenna pointing is constantly steered to maintain the radar footprint illuminating a fixed area on the ground during a time period longer than the conventional SAR aperture interval, thus achieving an azimuth resolution improvement. The steering of the antenna causes the spotlight raw data, as well as the focused image to present a systematic Doppler centroid drift in the azimuth direction. This drift rate f_{DR} of the image spectrum may be calculated from the Doppler values and their zero-Doppler time differences through the first and last azimuth time of the focused scene as follows [30]:

$$f_{DR} = \frac{f_{DC,n} - f_{DC,1}}{t_{DC,n} - t_{DC,1}} \tag{2}$$

where $f_{DC,1}$ and $f_{DC,n}$ account for the first and the last Doppler annotated values in the product and $t_{DC,1}$ and $t_{DC,1}$, their correspondent zero-Doppler corrected times.

This characteristic must be taken into account in the following interferometric processing chain steps: co-registration, resampling and, when applied, common band filtering. Prior to applying these steps, the center frequency of the interpolation kernels in azimuth must consider the Doppler drift or images must be adequately base-banded.

Each azimuth line must hence be demodulated with the following chirp function parameterized with drift rate [30]:

$$c(t) = e^{-j\pi(t-t_{start})^2 f_{DR}} \tag{3}$$

where t_{start} refers to the azimuth start time of the scene.

Once the drift rate is removed, the spectrum is centered on the start Doppler value. Then, the base-banding is performed, as is in the traditional strip-map case, multiplying the image in the spatial domain by a phase ramp in the azimuth parameterized with the zero-Doppler start value. The co-registration, resampling and common band filtering can be now applied. After these steps, both scenes are modulated back to their original frequency bands by multiplying them with the conjugate chirp $c^*(t)$, and classical strip-map PSI techniques may be employed.

5.1.3. The Coherent Pixels Technique

Among the multiple advanced PSI techniques developed in the last decade by the SAR community [5–15], the CPT [18,40] has been employed in this work to carry out the PSI processing.

This technique has been widely exploited during the last decade for studying the temporal evolution of a large number of ground displacements caused by human activities and natural hazards, using SAR data collected by space-borne sensors. The CPT allows the estimation of the linear and non-linear components of displacement, the topographic error of the digital elevation model (DEM) used in the generation of the differential interferograms and the APS from a set of differential interferograms [18,40]. In this framework, the CPT has been recently adapted to work with the zero-baseline fully-polarimetric GB-SAR data provided by the RiskSAR-X sensor. In addition, the TSC approach has been integrated in the pixel selection block, which worked before with the coherence stability and PS approaches.

Once the pixel selection is carried out, the first step of the CPT algorithm consists of performing a Delaunay triangulation of the pixel candidates selected. This strategy allows one to work with phase increments between pixels instead of absolute phases, which present some advantages. On the one hand, the absolute phase of individual pixels is not of practical utility due to the presence of different phase offsets among the set of differential interferograms. On the other hand, it allows minimizing the APS present in interferograms. Finally, if a good distribution of pixel candidates is assumed, the absolute phase increments may be supposed in most of the interferograms to be lower than π radians. The phase unwrapping step may hence be skipped at this stage.

Under the more general approach considering non-zero baseline interferograms, which applies to space-borne SAR data, the interferometric phase increment $\Delta\varphi_{m,n}$ between two connected points P_m and P_n by the triangulation is expressed for the $i-th$ interferogram as [18,40]:

$$\Delta\varphi_{m,n}\left(T_i, B_{n,i}\right) = \frac{4\pi}{\lambda}\cdot T_i \cdot \left(v(x_m, y_m) - v(x_n, y_n)\right) + \frac{4\pi}{\lambda}\cdot \frac{B_{n,i}}{R_i \sin\theta_i}\cdot\left(\varepsilon(x_m, y_m) - \varepsilon(x_n, y_n)\right) + \Delta\varphi_{m,n}^{res} \tag{4}$$

where (x_m, y_m) and (x_n, y_n) refer to the coordinates of the nodes forming the $arc_{m,n}$, $v(x_m, y_m) - v(x_n, y_n)$ and $\varepsilon(x_m, y_m) - \varepsilon(x_n, y_n)$ account for the increment of linear displacement rate and topographic error, λ indicates the wavelength, T_i and $B_{n,i}$ are the temporal and spatial baselines, respectively, R_i is the sensor to target distance, θ_i the incidence angle and $\Delta\varphi_{m,n}^{res}$, referred to as residual phase, refer to the atmospheric, non-linear and noise components of the phase.

For GB-SAR sensors operating under a zero-baseline configuration, the topographic error phase term is not considered. Likewise, there is not any APS contribution in the residue, since it was compensated for previously. The interferometric phase increment expression seen in Equation (4) is hence simplified in the following way:

$$\Delta\varphi_{m,n}(T_i) = \frac{4\pi}{\lambda} \cdot T_i \cdot (v(x_m, y_m) - v(x_n, y_n)) + \Delta\varphi_{m,n}^{res} \tag{5}$$

where, now, $\Delta\varphi_{m,n}^{res}$ accounts only for the non-linear and noise components of the phase.

In order to retrieve the displacement rate, a linear model is defined for each arc of the triangulation. The model is then adjusted to data through the minimization of a cost function, referred to as model adjustment function (MAF). Once the linear displacement rate is obtained, the MAF is evaluated in order to measure the quality of each arc. At this stage, low quality arcs are truncated, and those pixels which remain disconnected are removed. Another, the iteration of the minimization process is carried out with the surviving pixels. The process removes the pixels that do not fit the linear model, which may be caused by strong non-linear displacements in some particular cases. Finally, the absolute values of linear displacement for each pixel are obtained through an integration process, using one or multiple seeds with known behavior as tie points [40].

Finally, it must be pointed out that, regardless of the platform (orbital-, airborne- or ground-based), SAR systems only have sensitivity in the LOS direction. When facing landslide monitoring applications, the real displacement produced has an intrinsic topographic dependence, being related to the local slopes of the area under study. With no *a priori* knowledge, the more realistic kinetic model is based on considering that the surface mostly moves along the steepest gradient of the terrain slope. This information may be obtained from a DEM of the illuminated area. For this reason, results must be down-slope projected prior to its interpretation. Once the displacement vectors are accordingly projected, they are geocoded in map coordinates and may be visualized by using Geographical Information System (GIS) software or a virtual globe viewer.

5.2. PSI Displacement Results

Figures 13 and 14 show the down-slope ground displacement maps of El Forn de Canillo geocoded over a Google Earth image for the RiskSAR-X and the TerraSAR-X datasets, respectively. For the coherence stability method, a threshold of 0.65 has been employed; the PS technique has been carried out using a D_A threshold of 0.25; and finally, a threshold of 0.82 has been employed for the TSC approach. These thresholds are set in order to ensure the use of pixels with similar phase standard deviations in all cases, as seen in the previous section.

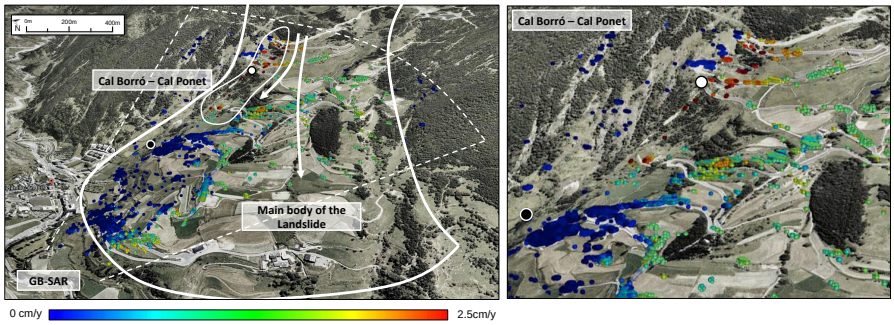

(a)

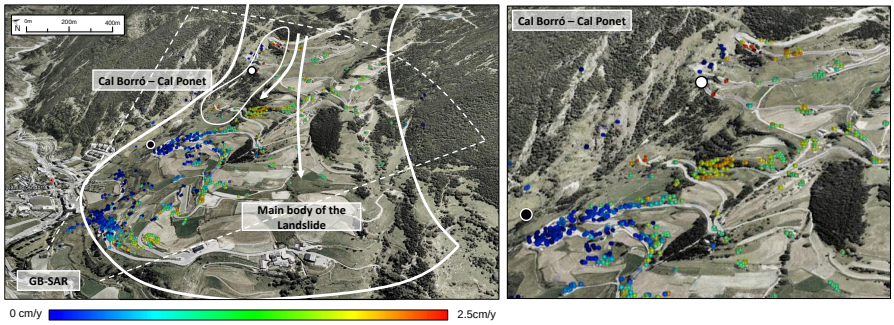

(b)

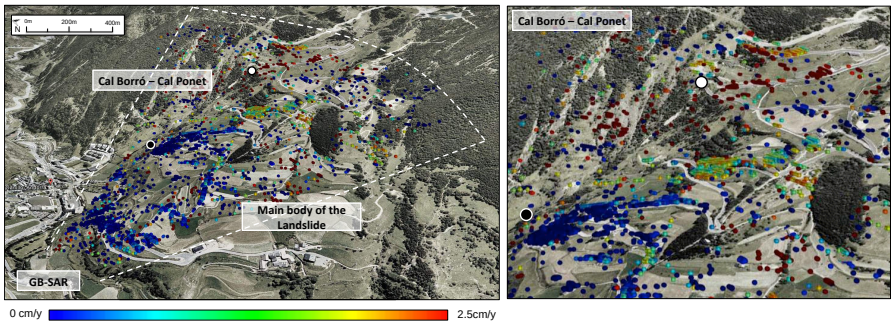

(c)

Figure 13. Geocoded down-slope linear displacement corresponding to El Forn de Canillo using (**a**) the TSC, (**b**) the coherence stability and (**c**) the D_A approach for the GB-SAR dataset. The black spot indicates the location of the seed employed during the integration step. The white spot indicates the location of the inclinometer S10, which will be employed as ground-truth to validate the results.

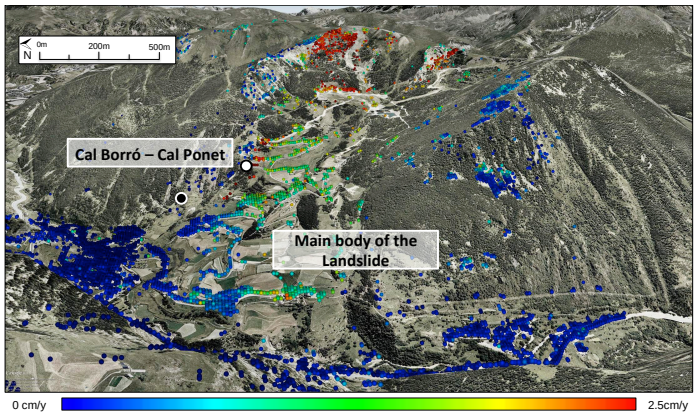

(a)

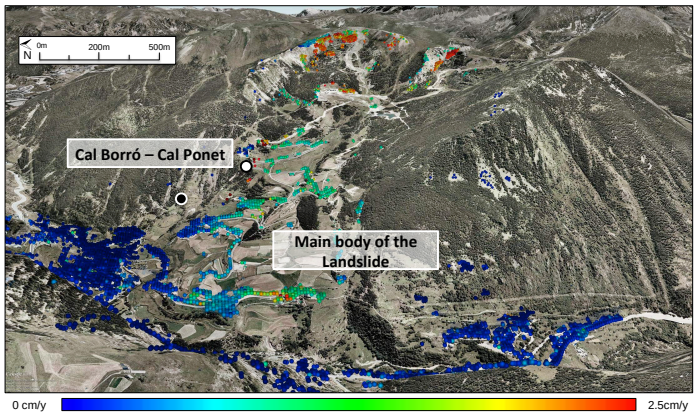

(b)

Figure 14. Geocoded down-slope linear displacement corresponding to El Forn de Canillo using (**a**) the TSC and (**b**) the coherence stability approach for the TerraSAR-X dataset. The black spot indicates the location of the seed employed during the integration step. The white spot indicates the location of the inclinometer S10, which will be employed as ground-truth to validate the results.

First of all, notice how the results in the common area processed by both sensors show a high agreement. As expected, the TSC and the coherence stability approaches are retrieving similar deformation trends, except for the increase in pixel density, especially over the land covers characterized by rocks surrounded by vegetation, which may be appreciated at both sides of the landslide. Recall that the ML processing limits the selection of deterministic point-like scatterers surrounded by non-coherent clutter. The denser results benefit the construction of a more robust network during the minimization and integration processes of the CPT, thus improving the reliability of the PSI results. At a more detailed

level, it must be noticed that the displacement magnitudes obtained by means of the TSC approach reach slightly higher values of displacements compared with the coherence stability results. This difference may be produced by ML carried out during the coherence estimation, which leads to averaging the displacement within the multilooked area.

Although the studies reported throughout the paper prevent the employment of the D_A estimator to perform the pixels selection, a PSI processing has been carried out employing the D_A for the GB-SAR study case. Indeed, the displacement results provided by the PS approach clearly result in being unreliable due to the low number of images available (see Figure 13c) and present a large amount of outliers.

Regarding the interpretation of the displacement maps retrieved, notice how in the lower part of the landslide, the PSI results obtained show a high agreement with the conclusions extracted from the field monitoring campaigns made between 2007 and 2009 presented in [28] (reviewed in Section 2). The displacement maps obtained reveal that the main body of landslide experienced a residual movement of 1–1.5 cm during the measurements interval. In addition, the local slide of Cal Borró-Cal Ponet may be perfectly identified for both sensors, presenting a higher activity of 2–2.5 cm/year.

Finally, some displacement trends, unknown until now, are also revealed in the upper part of the El Forn de Canillo through the TerraSAR-X PSI processing: the crest linking the Pic del Maians to the Pic d'Encampadana and another closer to the area known as Pla del Géspit. These displacements detected exhibit displacements closer to ∼3 cm/year. Unfortunately, the upper part of El Forn de Canillo lacks instruments to compare and validate the measurements obtained with TerraSAR-X. Despite this, the magnitude of displacement rates suggests that the slope should show activity indicators. Some field inspections have been carried out confirming the existence of such indicators as structural disturbance, tension cracks, depressions filled with sediments, covered by vegetation, as well as tilted and rotated blocks, with weathered surfaces.

At this stage, some ground-truth data are presented in order to validate the PSI results obtained. Figure 15 shows the inclinometric results in the borehole *S10*, which corresponds to the maximum displacement rate area of the lower part of the landslide (Cal Borró-Cal Ponet). The location of the borehole S10 is indicated in Figure 1b, seen in Section 2. In addition, this location has been also highlighted with a white spot in the PSI result figures (Figures 13 and 14).

Inclinometers are geotechnical devices for measuring horizontal displacements affecting the shape of a guide casing embedded in the ground. They provide the displacements undergone in two orthogonal planes, and this information allows obtaining the real 3D ground displacement vector of movement. It is worth mentioning that in order to obtain reliable estimations, the end of the guide casing must reach a stable reference. The technique consists of obtaining relative displacements profiles over time by repeating measurements at the same depths. This measures may be compared in order to detect the possible displacements undergone along the different measurement campaigns. Moreover, recording the magnitude of displacements at different reading depths is useful to identify shear bands and different units of movement. The most common way to analyze inclinometric results is based on displaying the cumulative lateral displacement along different depths, starting at the bottom of the casing and integrating increments of displacement for all depths up to the ground surface.

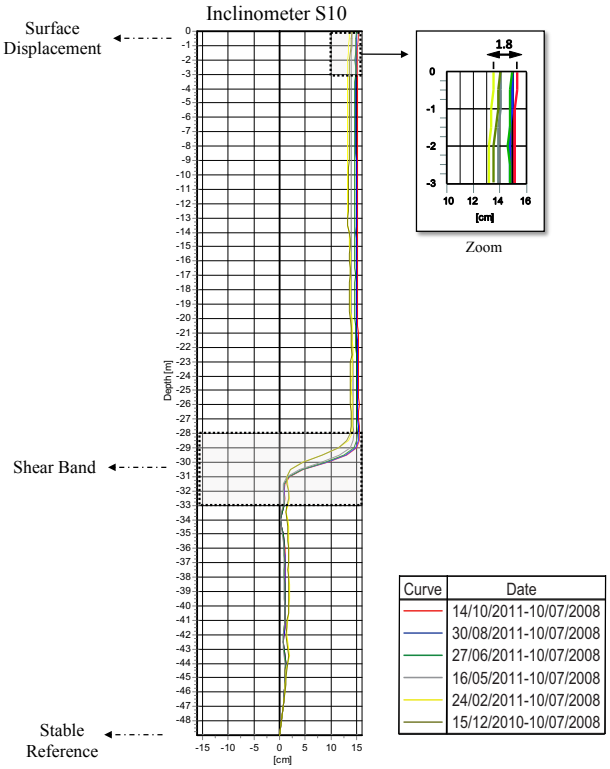

Figure 15. Inclinometric results in the borehole S10 (Cal Borró-Cal Ponet).

Figure 15 illustrates the deformed shape of the inclinometer casing along the borehole for different periods. Concretely, the curves available correspond to the period from December 2010, to October 2011, all referring to July 2008. The profiles plotted correspond to the maximum displacement axis (down-slope direction). Since the displacement is produced along the steepest gradient of the slope, the orthogonal axis did not record any displacement, and for this reason, it has not been represented in the figure. As indicated by the S-shaped plot, the main shear band is located at roughly 30 m under the surface of the landslide. The upper part of the plot has been amplified to compare the inclinometric results with the ones obtained using PSI techniques. The displacement undergone by the inclinometer between the period corresponding from December 2012 to October 2013, coinciding with the PSI processing, corresponds to 1.8 cm. Since the inclinometric results are given in an horizontal plane, these must be divided by the cosine of the slope angle in this area ($\sim$20°) in order to obtain the total down-slope displacement $\sim 1.8\,cm/\cos(20°) = 1.91\,cm$. This is equivalent to a total of roughly 2.3 cm/year. The results provided by the SAR sensors register $\sim$2.5 cm/year in this region, thus showing high agreement with the ground truth available.

As mentioned above, some geological evidence observed recently also corroborates the displacement results retrieved. Figure 16 presents some photographs obtained during several field inspections carried

out during 2013–2014. Figure 16a shows a picture of the interior of a famous house built in the mid-nineteenth century, near the area of maximum displacement of Cal Borró-Cal Ponet. The curved shape of the wall evidences the presence of displacements in the area. Figure 16b shows a picture of several cracks and shear openings along the road pavement, which have also appeared close to this area. Figure 16c shows curved trunks belonging to trees that have been subjected to a progressive tilt at the base, forcing the trunk to adopt this curvature in order to point vertically. These photographs have been taken in the upper part of the landslide. Figure 16d illustrates fresh cracks and openings within the rock mass in the outcrops of the Clots Fondos area, which denote the current activity. Figure 16e shows the detail of the perimeter stone fence that surrounds the area of Prat del Fornet field. The waviness of the formerly straight wall evidences the movements developing in the area.

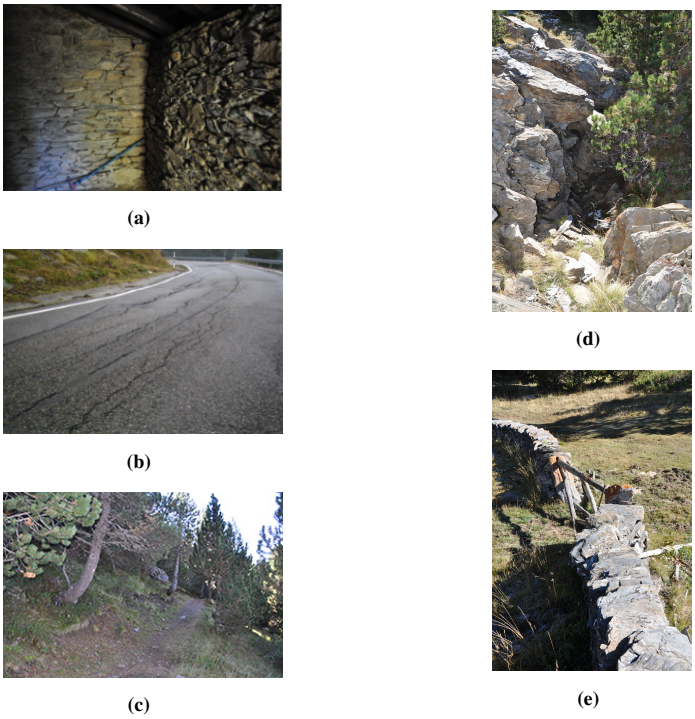

Figure 16. Photographs obtained during the field inspections works carried out during 2013–2014 evidencing the activity of El Forn de Canillo. (**a**) Interior view of the cracked walls of a small farmhouse and (**b**) cracks along road pavement located close to the area of Cal Borró–Cal Ponet; (**c**) curved trunks belonging to trees that have been subjected to a progressive tilt; (**d**) fresh cracks and openings within the rock mass in the outcrops of the Clots Fondos area; (**e**) perimeter stone fence that surrounds the area of Prat del Fornet field.

As illustrated throughout the paper, the coherence stability and the TSC approach are more suitable when a low number of images are at our disposal. Contrarily, the PS approach fails under these boundary conditions due to the unreliable estimation of the D_A. In general terms, it behaves in a similar way compared to the other two methods, but the selection of unreliable pixels as persistent scatterers finally leads to a noisy displacement map with a large number of outliers. The improvement in terms of pixel density provided by the TSC approach with respect to the coherence stability approach hence increases the precision in determining the extension of the deformation and presents clear advantages for characterizing the behavior of the different local slides present in the area of study. These results reveal that the TSC approach presented overcomes the intrinsic limitations of the classical pixel selection approaches: it allows performing a reliable full-resolution pixel selection when a small number of SAR images is available.

6. Conclusions

This paper shows the application of the TSC approach to work over reduced datasets of SAR acquisitions. The performance of this novel estimator has been tested over the slow-moving landslide of El Forn de Canillo using 10 images collected at the X-band during a one-year measurement campaign using the UPC's LFM-CW GB-SAR sensor. To complete the study, 10 sliding spotlight TerraSAR-X acquisitions have been also employed for the study. The type of data and the scenario selected has provided some added value to this work. The test site, mostly vegetated and only containing a few man-made structures, has constituted an extra challenge for the technique. PSI techniques usually perform worse over areas dominated by high temporal decorrelation phenomena.

The estimation accuracy, the number of pixel candidates and the final PSI displacement maps retrieved by means of the TSC approach proposed have been widely discussed in terms of pixel density and reliability. Furthermore, they have been compared with the so-called classical approaches, showing an improved performance on reduced datasets of SAR images. The number of pixels selected with the coherence stability and the TSC approach have been perfectly associated with the man-made structures and rocky areas present in the scenario. Both approaches have shown a similar performance in terms of PSI displacement results. Nonetheless, the resolution loss inherent to the coherence approach has led to a reduced number of pixels compared with the TSC approach (four-times less). Having higher densities in PSI results is a key factor, since it increases the precision of determining the extension of local displacements patterns and eases the characterization of the global displacement behavior. The PS approach has provided slightly higher pixel densities (roughly 10 percent more), but at the expense of including outliers in the final PSI results due to the unreliable estimation of the D_A index. In fact, it is a false improvement, as the low number of images makes the selection untruthful.

RiskSAR-X and TerraSAR-X have provided consistent measurements of the landslide displacements in El Forn de Canillo, which are compatible with the available inclinometric ones. Furthermore, the observations with TerraSAR-X, with greater spatial coverage, have shown that the displacements are significantly higher in the upper part of the slope ($\sim$3 cm/year), defining eventually an unstable rock mass whose existence had remained unnoticed so far. Field surveys have confirmed the

presence of activity indicators in this area, such as recent depressions, structural disturbance and open tension cracks.

In conclusion, the TSC approach has been demonstrated to be an excellent choice to overcome the limitations of classical approaches, when the full-resolution of images is to be preserved and the number of SAR images available is low.

Acknowledgments

This research work has been supported by the project TEC2011-28201-C02-01, funded by the Spanish Ministerio de Ciencia e Inovación (MICINN), and by the Government of Andorra (Edicte de 10/04/2013, Boletín Oficial Principado de Andorra (BOPA) No. 18 de 04/17/2014). The TerraSAR-X data has been provided by the German Aerospace Center (DLR) in the scope of the project GEO0878.

The authors would like to thank the company Euroconsult for the inclinometric results provided for the test site.

Author Contributions

Rubén Iglesias, Jordi J. Mallorqui and Dani Monells developed the methodology, carried out the processing and data analysis and wrote the paper. Carlos López-Martínez made important contributions related with the exploitation of the polarimetric data provided by the GB-SAR sensor and improved the quality of the paper during the writing. Xavier Fabregas contributed in the development of the GB-SAR processing chain. Albert Aguasca developed the RiskSAR sensor and coordinated all GB-SAR measurement campaigns. Josep A. Gili and Jordi Corominas gave a significant contribution to improve the geological knowledge of the landslide of El Forn de Canillo and deeply helped to provide the interpretation of the experimental results.

Abbreviations/Nomenclature

APS atmospheric phase screen

CPT coherent pixel technique

CS coherent scatterers

D_A amplitude dispersion

DDS digital direct synthesizer

DEM digital elevation model

DInSAR differential SAR interferometry

FMCW frequency modulated continuous wave

GB-SAR ground-based SAR

GCP ground control point

LFM-CW linear frequency modulated continuous wave

LTP long-term processing

LOS line-of-sight

MAF model adjustment function

ML multi-look

PS permanent scatterer

PSI persistent scatterer interferometry

RSLab remote sensing laboratory

SAR synthetic aperture radar

SCS stable coherent scatterers

SLC single look complex

SNR signal-to-noise ratio

STP short-term processing

SVA spatial variant apodization

TSC temporal sublook coherence

UPC Universitat Politècnica de Catalunya

Conflicts of Interest

The authors declare no conflict of interest.

References

1. Massonnet, D.; Feigl, K.L. Radar interferometry and its application to changes in the Earth's surface. *Rev. Geophys.* **1998**, *36*, 441–500.
2. Bürgmann, R.; Rosen, P.A.; Fielding, E.J. Synthetic Aperture Radar interferometry to measure Earth's surface topography and its deformation. *Ann. Rev. Earth Planet. Sci.* **2000**, *28*, 169–209.
3. Gabriel, A.K.; Goldstein, R.M.; Zebker, H.A. Mapping small elevation changes over large areas: Differential radar interferometry. *J. Geophys. Res.* **1989**, *94*, 9183–9191.
4. Hanssen, R.F. *Radar Interferometry: Data Interpretation and Error Analysis*; Kluwer Academic Publishers: Dordrecht, The Netherlands, 2001.
5. Ferretti, A.; Prati, C.; Rocca, F. Nonlinear subsidence rate estimation using permanent scatterers in differential SAR interferometry. *IEEE Trans. Geosci. Remote Sens.* **2000**, *38*, 2202–2212.
6. Ferretti, A.; Prati, C.; Rocca, F. Permanent Scatterers in SAR interferometry. *IEEE Trans. Geosci. Remote Sens.* **2001**, *39*, 8–20.
7. Mora, O.; Mallorqui, J.J.; Duro, J. Generation of deformation maps at low resolution using differential interferometric SAR data. In Proceedings of 2002 IEEE International Geoscience and Remote Sensing Symposium, IGARSS '02, Toronto, ON, Canada, 24–28 June 2002.

8. Berardino, P.; Fornaro, G.; Lanari, R.; Sansosti, E. A new algorithm for surface deformation monitoring based on small baseline differential SAR interferograms. *IEEE Trans. Geosci. Remote Sens.* **2002**, *40*, 2375–2383.
9. Werner, C.; Wegmuller, U.; Strozzi, T.; Wiesmann, A. Interferometric point target analysis for deformation mapping. In Proceedings of 2003 IEEE International Geoscience and Remote Sensing Symposium, IGARSS '03, Toulouse, France, 21–25 July 2003.
10. Arnaud, A.; Adam, N.; Hanssen, R.; Inglada, J.; Duro, J.; Closa, J.; Eineder, M. ASAR ERS interferometric phase continuity. In Proceedings of 2003 IEEE International Geoscience and Remote Sensing Symposium, IGARSS '03, Toulouse, France, 21–25 July 2003.
11. Hooper, A.; Zebker, H.; Segall, P.; Kampes, B. A new method for measuring deformation on volcanoes and other natural terrains using InSAR persistent scatterers. *Geophys. Res. Lett.* **2004**, *31*, doi:10.1029/2004GL021737.
12. Lanari, R.; Mora, O.; Manunta, M.; Mallorqui, J.J.; Berardino, P.; Sansosti, E. A small-baseline approach for investigating deformations on full-resolution differential SAR interferograms. *IEEE Trans. Geosci. Remote Sens.* **2004**, *42*, 1377–1386.
13. Hooper, A. A multi-temporal InSAR method incorporating both persistent scatterer and small baseline approaches. *Geophys. Res. Lett.* **2008**, *35*, doi:10.1029/2008GL034654.
14. Fornaro, G.; Reale, D.; Serafino, F. Four-dimensional SAR imaging for height estimation and monitoring of single and double scatterers. *IEEE Trans. Geosci. Remote Sens.* **2009**, *47*, 224–237.
15. Ferretti, A.; Fumagalli, A.; Novali, F.; Prati, C.; Rocca, F.; Rucci, A. A new algorithm for processing interferometric data-stacks: SqueeSAR. *IEEE Trans. Geosci. Remote Sens.* **2011**, *49*, 3460–3470.
16. Massonnet, D.; Briole, P.; Arnaud, A. Deflation of Mount Etna monitored by spaceborne radar interferometry. *Nature* **1995**, *375*, 567–570.
17. Lundgren, P.; Usai, S.; Sansosti, E.; Lanari, R.; Tesauro, M.; Fornaro, G.; Berardino, P. Modeling surface deformation observed with synthetic aperture radar interferometry at Campi Flegrei caldera. *J. Geophys. Res.* **2001**, *106*, 19355–19366.
18. Mora, O.; Mallorqui, J.; Broquetas, A. Linear and nonlinear terrain deformation maps from a reduced set of interferometric sar images. *IEEE Trans. Geosci. Remote Sens.* **2003**, *41*, 2243–2253.
19. Kwok, R.; Fahnestock, M. Ice sheet motion and topography from radar interferometry. *IEEE Trans. Geosci. Remote Sens.* **1996**, *34*, 189–200.
20. Refice, A.; Bovenga, F.; Guerriero, L.; Wasowski, J. DInSAR applications to landslide studies. In Proceedings of IEEE 2001 International Geoscience and Remote Sensing Symposium, IGARSS '01, Sydney, Australia, 9–13 July 2001.
21. Kim, S.-W.; Won, J.-S. Measurements of soil compaction rate by using JERS-1 SAR and a prediction model. *IEEE Trans. Geosci. Remote Sens.* **2003**, *41*, 2683–2686.
22. Buckreuss, S.; Balzer, W.; Muhlbauer, P.; Werninghaus, R.; Pitz, W. The terraSAR-X satellite project. In Proceedings of 2003 IEEE International Geoscience and Remote Sensing Symposium, IGARSS '03, Toulouse, France, 21–25 July 2003.

23. Buckreuss, S.; Roth, A. Status Report on the TerraSAR-X Mission. In Proceedings of 2008 IEEE International Geoscience and Remote Sensing Symposium, IGARSS 2008, Boston, MA, USA, 7–11 July 2008.
24. Venturini, R.; Fois, F.; Sirocchi, G.; Bauleo, A.; Bazzoni, A.; Borgarelli, L.; Capece, P.; Cereoli, L.; Croci, R.; Farina, C.; *et al*. Experimental verification of COSMO-SkyMed SAR capabilities. In Proceedings of 2008 IEEE Radar Conference, RADAR '08, Rome, Italy, 26–30 May 2008.
25. Iglesias, R.; Mallorqui, J.J.; Lopez-Dekker, P. DInSAR pixel selection based on sublook spectral correlation along time. *IEEE Trans. Geosci. Remote Sens.* **2014**, *52*, 3788–3799.
26. Schneider, R.; Papathanassiou, K.; Hajnsek, I.; Moreira, A. Polarimetric and interferometric characterization of coherent scatterers in urban areas. *IEEE Trans. Geosci. Remote Sens.* **2006**, *44*, 971–984.
27. Santacana, N. Estudi dels grans esllavissaments d'Andorra: Els casos del Forn i del vessant d'Encampadana. Ph.D. Thesis, Department of Dynamic Geology, Geophysics and Paleontology, Faculty of Geology, University of Barcelona, Barcelona, Spain, 1994.
28. Torrebadella, J.; Villaró, I.; Altimir, J.; Amigó, J.; Vilaplana, J.M.; Corominas, J.; Planas, X. El Deslizamiento del Forn de Canilloen Andorra. Un Ejemplo de Gestión del Riesgo Geológico en Zonas Habitadas en Grandes Deslizamientos. In Proceedings of VII Simposio Nacional sobre Taludes y Laderas Inestables, Barcelona, Spain, 27–30 October 2009.
29. Crosetto, M.; Monserrat, O.; Luzi, G.; Cuevas-González, M.; Devanthéry, N. Discontinuous GBSAR deformation monitoring. *ISPRS J. Photogramm. Remote Sens.* **2014**, *93*, 136–141.
30. Eineder, M.; Adam, N.; Bamler, R.; Yague-Martinez, N.; Breit, H. Spaceborne spotlight SAR interferometry with TerraSAR-X. *IEEE Trans. Geosci. Remote Sens.* **2009**, *47*, 1524–1535.
31. Iglesias, R.; Mallorqui, J.J. Side-Lobe Cancelation in DInSAR Pixel Selection With SVA. *IEEE Geosci. Remote Sens. Lett.* **2013**, *10*, 667–671.
32. Touzi, R.; Lopes, A.; Bruniquel, J.; Vachon, P. Coherence estimation for SAR imagery. *IEEE Trans. Geosci. Remote Sens.* **1999**, *37*, 135–149.
33. Iglesias, R.; Fabregas, X.; Aguasca, A.; Mallorqui, J.J.; Lopez-Martinez, C.; Gili, J.A.; Corominas, J. Atmospheric phase screen compensation in Ground-Based SAR with a multiple-regression model over mountainous regions. *IEEE Trans. Geosci. Remote Sens.* **2014**, *52*, 2436–2449.
34. Soumekh, M. *Synthetic Aperture Radar Signal Processing: With MATLAB Algorithms*; John Wiley & Sons, Inc.: Hoboken, NJ, USA, 1999.
35. Cumming, I.; Wong, F. *Digital Processing of Synthetic Aperture Radar Data: Algorithms and Implementation*; Artech House: London, UK and Boston, MA, USA, 2005.
36. Pipia, L.; Fabregas, X.; Aguasca, A.; Lopez-Martinez, C. Atmospheric artifact compensation in ground-based DInSAR applications. *IEEE Geosci. Remote Sens. Lett.* **2008**, *5*, 88–92.
37. Leva, D.; Nico, G.; Tarchi, D.; Fortuny-Guasch, J.; Sieber, A. Temporal analysis of a landslide by means of a ground-based SAR interferometer. *IEEE Trans. Geosci. Remote Sens.* **2003**, *41*, 745–752.

38. Iannini, L.; Guarnieri, A.M. Atmospheric phase screen in ground-based radar: Statistics and compensation. *IEEE Geosci. Remote Sens. Lett.* **2011**, *8*, 537–541.
39. Iglesias, R.; Monells, D.; Fabregas, X.; Mallorqui, J.J.; Aguasca, A.; Lopez-Martinez, C. Phase quality optimization in polarimetric differential SAR interferometry. *IEEE Trans. Geosci. Remote Sens.* **2014**, *52*, 2875–2888.
40. Blanco-Sánchez, P.; Mallorquí, J.J.; Duque, S.; Monells, D. The coherent pixels technique (CPT): An advanced DInSAR technique for nonlinear deformation monitoring. *Pure Appl. Geophys.* **2008**, *165*, 1167–1193.

9

Chapter 9
Conclusions

9.1 Main conclusions

This PhD Thesis has been devoted to the evaluation and improvement of space-borne and ground-based PSI techniques for the efficient monitoring of slow-moving landslides. While all the techniques proposed can be generalized, the primary focus of study of this work corresponds to the analysis of the landslide of *El Forn de Canillo*, which constitutes one of the biggest landslides of the Andorran Pyrenees.

For this purpose, a one-year monitoring work, from October 2010 to November 2011, employing SAR images acquired with the German TerraSAR-X satellite in sliding-spotlight mode and with the UPC's GB-SAR system was planned. In this context, the GB-SAR sensor focused on the urbanized area of the landslide, located at the lower part of the sliding mass, where the geotechnical devices were installed, while the sliding-spotlight TerraSAR-X SAR images covered the whole landslide extension.

The main conclusions of the different studies developed in this PhD Thesis may be summarized in the following points:

- **X-band space-borne sliding-spotlight SAR data exploitation**.

  The conventional stripmap interferometric chain has been adapted to work with the sliding-spotlight imaging mode provided by the German satellite TerraSAR-X (as seen in Section 2.2.2 of Chapter 2). In this context, the new observational capabilities offered by this imaging mode have been evaluated for landslide monitoring applications.

  Its improved resolution (up to one meter in both range and azimuth) jointly with its shorter revisiting time (11 days) have allowed the exploitation of unprecedented amounts of persistent scatterers, thus improving the PSI performance over this type of scenarios, compared with its predecessors ERS-1/2, ENVISAT-ASAR or RADARSAT-1, that used medium resolution with lower bandwidths at C-band.

  In this context, space-borne X-band sensors, initially designed for improving monitoring capabilities over man-made structures, such as buildings, bridges, railways or highways, have also demonstrated an outstanding performance over natural reflectors, such as outcrops or exposed rocks.

  In conclusion, advanced high-resolution imaging modes have demonstrated to be fully operational for landslide monitoring applications. The results obtained in this PhD Thesis have shown an improved performance compared with classical stripmap and have demonstrated that this imaging mode is ready to its commercial use in order to ease the monitoring and characterization of complex landslides such as *El Forn de Canillo*.

- **Space-borne PSI improvements**.

  While the classical stripmap interferometric chain has been adapted to work with sliding-spotlight data, some other improvements have been proposed to enhance classical space-borne PSI performance for landslide monitoring:

  – First, an adaptive common-band range spectral filtering relying on local topography has been presented in order to improve the quality of the interferograms involved in the PSI processing (Section 2.4.1.2 of Chapter 2). Since landslides

typically occur over mountainous areas with steep topography and, hence, largely affected by geometrical decorrelation, the coherence of interferograms can be significantly improved by filtering-out the non-common part of range spectra.

- In order to face the large temporal and geometrical decorrelation factors present in this type of scenarios, an enhanced selection of interferograms has been proposed (Section 3.2.1 of Chapter 3). On the one hand, a sub-list of interferograms for the estimation of displacements may be obtained fixing short spatial baseline pairs, but allowing larger temporal ones. On the other hand, a sub-list of interferograms for the estimation of the topographic error may be obtained by fixing short temporal baseline pairs, but allowing larger spatial ones. Both lists are finally combined. The rationale of this method is to avoid the limit situation of selecting interferometric pairs largely affected by both temporal and spatial decorrelation phenomena. This approach has demonstrated to improve the overall mean coherence of the interferograms involved in the PSI processing.
- Classical PSI pixel selection step has been improved by means of SVA technique (Section 3.2.4 of Chapter 3). SAR systems are band-limited in range and azimuth and, for this reason, the PSF has the shape of a bi-dimensional *sinc* function. Moreover, SAR images are slightly oversampled and the contribution of a single target sometimes extends to more than a single resolution cell. This fact makes the main lobe and the side-lobes of high-power scatterers to have a great contribution in areas with a reduced coefficient of backs-scattering. In this framework, a novel usage of the SVA technique has been proposed in order to mitigate these undesired artifacts.
- In order to improve the robustness of the algorithms during the PSI, the employment of redundant networks has been proposed during the triangulation step (Section 3.3.1 of Chapter 3).
- Finally, a down-slope hypothesis assumption has been presented (as seen in Section 3.5 of Chapter 3). SAR systems only have sensitivity to detect displacements in the LOS direction and, for this reason, prior to the interpretation of any PSI product, the detected displacements must be re-projected along the real ground displacement direction. In landslides, this is along the steepest gradient of the terrain slope. In the same context, the application of geometrical filters has been proposed to face the negative impact of SAR distortions, such as foreshortening or layover. The rationale behind this final filtering is to prevent the inclusion of possible outliers in final products.

- **GB-InSAR techniques for GB-SAR discontinuous monitoring**.

  GB-InSAR techniques have been presented in Chapter 4 as an alternative remote sensing solution ideal for landslide monitoring. As seen, the high stability of the platform, the possibility to adapt the revisiting time in function of the displacement phenomena dynamics, and the ability to fit the illumination angle to the specific site geometry, make GB-InSAR techniques an attractive alternative to orbital-based solutions.

  This PhD Thesis has been focused on GB-SAR sensors working under a discontinuous operation mode. This means revisiting the AOI during different measurement days with a certain temporal span. In this context, it has been demonstrated that this *modus operandi* is the most efficient when a slow displacement process is expected. Following this strategy, the maintenance cost and the chance of damages of an unattended the system are drastically reduced. Contrarily, the processing required is more challenging.

  In this framework, the whole GB-InSAR processing chain has been completely described. On the one hand, the STP block has been presented in order to improve the SNR of time-stationary targets, leading to a time-averaged SAR image for each measurement day. On the other hand, the LTP block has been widely described in order to deal with the atmospheric artifacts among the different time-averaged images obtained in the previous step.

  In fact, APS has demonstrated to represent the most relevant artifact of distortion between interferometric GB-SAR pairs and most of the efforts have been addressed to mitigate its negative impact. From all methods available in the literature, model-based solutions have proven to be very effective since they reach accurate estimates of APS with no need of extra meteorological data or stable ground control points. Unfortunately, the techniques available in the literature, based on a spatial homogeneity assumption, fail over scenarios with steep topography. In these areas, high atmospheric disturbances, deeply correlated with the topography and highly dynamic in time, are present. For this reason, a more general APS model accounting for height-dependent components has been presented in this PhD Thesis.

  The new model proposed has been validated comparing real records of APS with simulations obtained through meteorological measurements provided by a weather station. Simulated and real APS have shown a high degree of agreement. In addition, its performance has been tested with short-temporal-span real GB-SAR data. The rationale at this point was analyzing differential interferograms free of displacement disturbances. After applying the technique proposed, the resulting differential phase presented zero-mean value and low phase standard deviation, thus showing the good performance of the proposed approach over real scenarios. The exploitation of polarimetric information has been finally proposed in order to improve the number of reliable pixels during the model construction.

- **Polarimetric optimization techniques**.

  After developing GB-InSAR techniques, mainly focusing in the compensation of height-dependent APS in short-term and long-term interferograms, and prior to the application of PSI algorithms, the application of polarimetric optimization methods has been studied in detail in Chapter 5. The objective has been to improve the phase quality of interferograms with the proper combination of the polarimetric channels available. The different polarimetric optimization methods available in the literature have been evaluated and adapted to the particular characteristics of the data and the pixel selection criteria (coherence stability or D_A).

  In this framework, the simplest method that can be employed corresponds to the so-called Best. This approach is based on selecting the polarimetric channel providing the best value in terms of either coherence or amplitude dispersion. Despite the significant improvement that can be achieved with this approach, it does not completely exploit the potentials of polarimetric data. For this reason, more advanced methods have been evaluated. On the one hand, the ESM approach has been able to reach the best optimized values, since it is based on exploring the complete space of polarimetric combinations. Unfortunately, it requires a high computational cost. On the other hand, the SOM approach, which requires the optimization of lower number of parameters (orientation and ellipcity angles), has demonstrated to perform the optimization process in less time, however, the solutions found are just a subset of the complete space of solutions. As a consequence, the SOM performance is lower, in terms of phase quality and pixels' density, compared with the ESM approach. Finally, the ESM algorithm has been observed to be only valid under the assumption of polarimetric stationarity. When this hypothesis does not apply, the algorithm does not reach the maximum and the optimized differential phase may be affected by this difference in the polarimetric behavior. The SOM approach, which solves the optimization problem in a way closer to a physical interpretation, prevents the inclusion of these outliers.

  In order to face the high computational cost of ESM and SOM, both techniques have been improved with the combination of a coarse search of the global minimum and the use of the CGM algorithm. Following this strategy, the optimum projection vectors have been found much faster, reaching up to six orders of magnitude less, with identical results.

  Regarding the pixel selection strategy, it has been demonstrated how working with the coherence estimator, the optimum projection vector may be optimized at interferogram level for the zero-baseline case, i.e, GB-SAR data. On the contrary, when working with multi-baseline data coming from space-borne sensors the optimum projection vector needs to be identical for all interferograms in order to avoid changes in the phase center. When working at full-resolution with the D_A approach, the projection vector needs to be the same in the whole stack of SAR images, regardless of the platform.

  The optimized stack of interferograms has allowed the selection of a larger number of persistent scatterers, achieving up to a threefold increase of the number of pixel candidates for the GB-SAR case. The overall displacement patterns have shown a similar response in all cases, being the pixels' density the only difference between

the optimized and the standard products. As seen, this fact results of great importance for the delineation and characterization of landslides. The recent launch of the satellites ALOS-2 and Sentinel-1, with polarimetric capabilities, highlights the significance of this topic.

- **GB-SAR PSI**.

  Once the way to compensate APS and to improve GB-InSAR performance by means of polarimetric data exploitation have been studied, the final development of the GB-SAR PSI processing chain for the estimation of the linear component of displacement, but also its non-linear component, has been presented in Chapter 6. This development has been based on the adaptation of CPT to work with the fully-polarimetric zero-baseline data provided by the RiskSAR sensor.

  The usefulness of GB-SAR PSI techniques for landslide monitoring applications have been put forward over the test site of *El Forn de Canillo*. The key processing steps, taking into account the particularities of this type of natural environments with steep topography, have been highlighted comparing its performance with a nominal study case affected by urban subsidence. Finally, the obtained displacement maps have been validated with in-field ground truth data. The reliability of GB-SAR solutions has thus been demonstrated, showing an impressive performance to hazard assessment and risk management.

  Compared with space-borne solutions, GB-SAR PSI presents several competitive advantages due to the zero-baseline configuration of the instrument. On the one hand, the revisiting time is no longer a constraint due to the employment of a terrestrial platform. On the other hand, they offer the possibility to fit the illumination angle in order to maximize the detection of real ground displacement in the LOS direction. Anyway, this is strongly dependent on the characteristics of the site and in some cases it could not be possible. Finally, since APS may be perfectly estimated and compensated for by means of model-based techniques, lower numbers of images are required in order to assess the non-linear estimation of the ground displacement process.

  Contrarily, GB-SAR products offer a poorer coverage compared with the ones obtained with space-borne platforms. Moreover, if a continuous monitoring is employed, there is an unavoidable loss of the availability of the instrument (since it is intrinsically blocked to its application in a single scenario). The maintenance cost or possible damages of an unattended the system represent other disadvantages.

  Compared with traditional in-field monitoring devices and techniques, GB-SAR solutions have demonstrated to provide higher densities and to be very efficient in order to cover larger areas for long periods at lower cost.

- **Full-resolution PSI over reduced data sets of SAR images**

  Finally, with the objective of performing a full-resolution PSI when a reduced number of SAR images is available, a new PSI approach has been presented in Chapter 7. As commented along this PhD Thesis, the high-resolution capabilities of the new generation of sensors have lead to breakthrough in the way of studying displacement phenomena. Nonetheless, the acquisition of these products have become considerable more expensive, compromising in many cases the acquisition of a large

number of images with the lowest time lapses. Moreover, the study of slow-rate displacement phenomena, such as the one studied in this PhD Thesis, does not require the planning of large amounts of SAR data since it clearly results unfruitful. This is the case of the GB-SAR data set available in this PhD Thesis, composed by 10 GB-SAR acquisitions, which is enough to follow the slow-rate displacement expected in the landslide of *El Forn de Canillo*. Unfortunately, it has been demonstrated how classical approaches present an intrinsic limitation in this case.

In this framework, the development a new phase quality estimator, referred to as TSSC, has been presented to obtain full-resolution PSI products over reduced data sets of SAR images. In this context, the estimation accuracy, the number of pixel candidates and the final PSI displacement maps retrieved by means of the TSSC approach proposed have been widely discussed in terms of pixels' density and reliability for both urban and natural environments. In addition, an extension of the TSC approach to work with the Best, ESM, and SOM polarimetric optimization methods has been also put forward.

The proposed approach has been compared with the so-called classical approaches showing an improved performance. Going into further detail, the pixels selected with the coherence stability and the TSSC approach have been perfectly associated with the man-made structures and natural persistent scatterers present in the landslide of *El Forn de Canillo*. Both approaches have shown similar displacement results. Nonetheless, the resolution loss inherent to the coherence approach has led to a reduced density in the results compared with the TSSC approach. Moreover, high-quality pixels surrounded by non-coherent clutter have been inevitably lost under the coherence stability approach, once again, due to the multi-look factor employed. Finally, the PS approach has presented a big amount of outliers in final PSI displacement maps due to the unreliable estimation of the D_A index.

In conclusion, the TSSC approach has demonstrated to be an excellent choice to overcome the limitations of classical approaches when the full-resolution of images wants to be preserved and the number of SAR images available is low. As seen, working at full-resolution with the new generation of X-band sensors is a key factor to increase the density of measurements. This fact allows an intrinsic improvement in the precision to delineate the extension of local displacements patterns and ease the characterization of complex landslides.

- **Displacement results over *El Forn de Canillo***

  RiskSAR and TerraSAR-X sensors have provided consistent displacement results over the landslide of *El Forn de Canillo* (presented in Chapter 8), which are compatible with the available inclinometric ones (presented in Section 1.4.3 of Chapter 1). The displacement maps obtained reveal that the main body of the landslide has experienced a residual down-slope displacement of $1 - 1.5$ cm/year during the interval of measurements. In addition, the local slide of *Cal Borró-Cal Ponet* has been perfectly identified with both sensors, presenting a higher activity of $2 - 2.5$ cm/year (as seen in Chapter 8).

  In order to illustrate the high agreement between the results obtained with both sensors by means of temporal evolution, the down-slope time-series over the maximum displacement rate area of *Cal Borró-Cal Ponet* is finally presented, see Fig. 9.1. As

done in Chapter 8, only 10 images have been employed for the TerrSAR-X case in order to make a fair comparison between both sensors. On the one hand, Fig. 9.1a shows the time-series obtained with the GB-SAR data set (presented previously in Chapter 6). On other hand, Fig. 9.1b shows the time-series obtained with the TerraSAR-X data set. The solid line represents the temporal evolution taking as reference the first date. In order to ease the comparison between the GB-SAR and TerraSAR-X results, an overall offset of 0.44 cm (corresponding to the displacement recorded by the GB-SAR sensor for the first TerraSAR-X acquisition date) has been applied to the TerraSAR-X time-series. The result is represented with a dashed line in Fig. 9.1b. A high agreement can be appreciated between both time-series. Notice that the displacement observed is characterized by some non-linear component in both cases, exhibiting some acceleration and stabilization during the period of measures. These periods coincide with the fall (from October to November 2010) and spring (from February to May 2011), when the major rainfall and snow melting events were produced. In the last period of the graph (September 2011), coinciding again with autumn's arrival, the landslide seems to accelerate again.

Finally, the information collected with TerraSAR-X, with greater spatial coverage, has revealed some displacements significantly higher in the upper part of the slope (3 cm/year). Field surveys have confirmed the presence of activity indicators in this area, such as recent depressions, structural disturbance and open tension cracks.

9.2 Future research lines

Several research lines can be thought of as a continuation of the work developed during this PhD Thesis that make use of the conclusions drawn from it.

- **Staring-spotlight imaging mode evaluation**.

  The improvement of resolution in SAR imaging is allowing the development of innovative applications, even for purposes that few years ago relied only on optical sensors. The benefits of employing high-resolution SAR imaging for landslide monitoring applications have been demonstrated in this PhD work using sliding-spotlight SAR images provided by the TerraSAR-X sensor. This imaging mode has allowed a significant improvement in the monitoring capabilities over man-made structures, but also in the exploitation of natural stable reflectors, such as outcrops or exposed rocks.

  In this context, TerraSAR-X has demonstrated to be a pioneer in several space innovative modes like the Terrain Observation by Progressive Scans (TOPS) imaging mode, space-borne bistatic SAR (with its twin satellite, TanDEM-X), or digital beam-forming [140]. One of the last milestones reached has been the acquisition of staring-spotlight SAR data, available since October 2013. As seen in this PhD Thesis, spotlight imaging mode is characterized by an azimuth steering that points the antenna pattern to keep the radar footprint illuminating a fixed spot on the ground. In this context, staring-spotlight is the pure spotlight mode providing the best possible azimuth resolution [140]. The sliding-spotlight imaging mode employed in this PhD Thesis (unique spotlight imaging mode available at 2011 when the monitor-

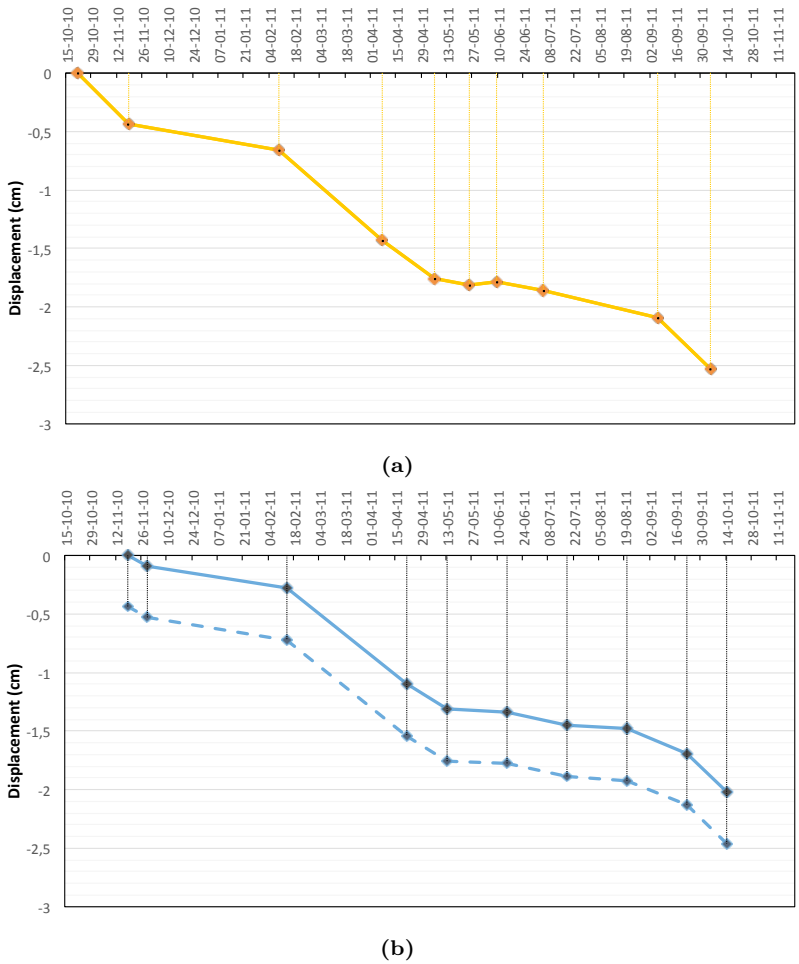

Figure 9.1: Down-slope time-series obtained over the area of *Cal Borró-Cal Ponet* with (a) the RiksSAR and (b) the TerraSAR-X sensor operating in sliding-spotlight imaging mode, employing only 10 images for both sensors. The solid line in (b) represents the TerraSAR-X time-series taking as reference the first date. The dashed line illustrates the same temporal evolution after applying an overall offset of 0.44 cm, which corresponds to the displacement recorded by the GB-SAR sensor for the first TerraSAR-X acquisition date.

ing of *El Forn de Canillo* was planned) applies a slower antenna steering in order to increase the azimuth scene size. Indeed, this fact worsens the azimuth resolution with respect to the staring-spotlight mode. Contrarily, the staring-spotlight imaging mode exploits the maximum azimuth steering capabilities of TerraSAR-X sensor reaching a steering range of $\pm 2°$ and thus achieving an azimuth resolution of 16 cm [192].

In this framework, the exploitation of staring-spotlight data could be an exciting future research line, since there are only few works published showing its potential for PSI applications. Fig. 9.2 shows a zoom of a reflectivity image of a

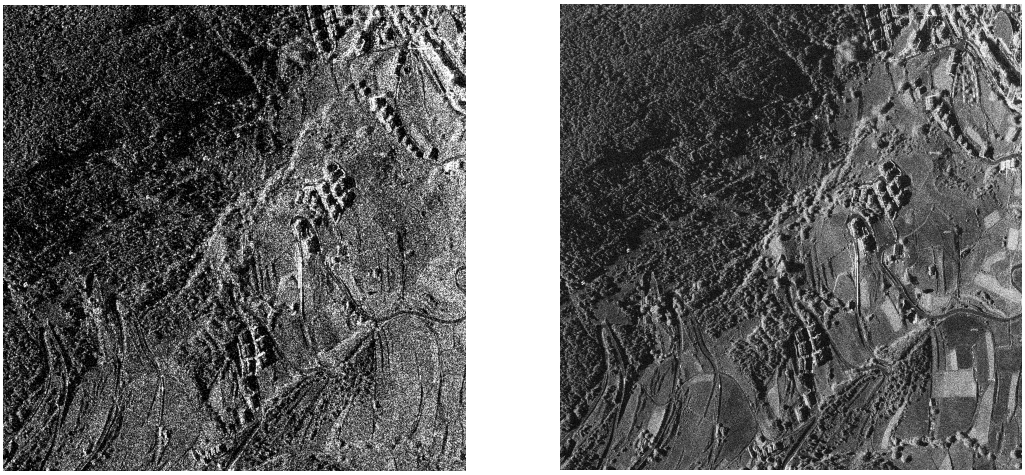

(a) **(b)**

Figure 9.2: Zoom of a reflectivity image of the TerraSAR-X staring-spotlight acquisition acquired over *El Forn de Canillo*, with 21 cm azimuth resolution and 58 cm slant-range resolution, compared with one of the sliding-spotlight images employed in this PhD work. (a) Sliding-spotlight and (b) staring-spotlight imaging modes.

TerraSAR-X staring-spotlight acquisition acquired over *El Forn de Canillo*, with 21 cm azimuth resolution and 58 cm slant-range resolution, compared with one of the sliding-spotlight images employed in this PhD work. The impressive details and its improved capabilities in terms of resolution predict a step further in the detection and characterization of landslides.

- **Sentinel-1 data exploitation**.

  A completely different, but complementary strategy, could be the exploitation of Sentinel-1 data. Sentinel-1 is a two satellite constellation, designed and developed by ESA and funded by the European Commission (EC), with the prime objective of providing C-Band SAR data continuity following the retirement of ERS-2 and the end of the ENVISAT mission. Sentinel-1 constellation provides an improved revisit time (12-day repeat orbit cycle with one satellite), a large geographical coverage and rapid data dissemination to support operational applications, such as land monitoring or emergency services. The first satellite of the constellation, Sentinel-1A, was launched on April 2014, while the second satellite, Sentinel-1B, is scheduled for 2016. This latter will improve the revisiting time of the constellation up to 6 days.

  The default acquisition mode of Sentinel-1 for land services corresponds to the interferometric wide swath or TOPS [193–196]. In this acquisition mode, the radar beam scans back and forth three times within a single swath, referred to as sub-swaths, resulting in a higher quality and homogeneous image throughout the swath, compared with scanSAR. This mode provides a swath width of 250 km and a ground-resolution of 5×20 m.

  Since Sentinel-1 routinely provides free data and information products of large-

scale areas, its exploitation could be an interesting research line. This PhD Thesis has been devoted to demonstrate the benefits of employing high-resolution sensors with improved resolution capabilities for landslide monitoring applications. A more complete strategy could be using Sentinel-1 data to monitor large-scale areas prone to be affected by landslides (for instance the whole Pyrenees) and then order the monitoring of the detected areas with a high-resolution sensor such as TerraSAR-X.

In this context, one of the most challenging aspects in TOPS interferometry is the fact that the acquired data have large Doppler Centroid variations within the same burst [196]. These large Doppler variations introduce strong requirements in the co-registration accuracy to avoid phase discontinuities at burst edges. For this reason, the first task should be adapting the interferometric chain PRISAR to the particularities of TOPS SAR Interferometry, as done in this PhD Thesis with the sliding-spotlight imaging mode.

- **Joint exploitation of point-like and distributed scatterers**.

  As showed along this PhD Thesis, mainly due to decorrelation phenomena, displacement information can be only exploited over the persistent scatterers within the illuminated scenario. In this framework, the different strategies to detect persistent scatterers, i.e, the coherence stability and the PS approach, has been evaluated. In order to overcome the limitation of the PS technique when a few number of images is low, a new full-resolution PSI approach based on the exploitation of the coherence between different sublooks of the image spectrum has been presented. Despite the good performance of the TSSC technique to carry out full-resolution PSI when a reduced number of SAR images is available, this approach only allows the selection of deterministic point-like scatterers. With the arrival of the new generation of space-borne SAR sensors, with improved resolution capabilities, it has been demonstrated that a big amount of point-like scatterers (such as man-made constructions, outcrops, exposed rocks, etc.) may be also found in natural environments. This fact allows to outperform, in terms of density, any low-resolution PSI based on coherence estimation since it requires the multi-looking of data, thus degrading the original resolution of images. Despite this negative aspect, it is true that averaging data spatially over statistically homogeneous areas increases the SNR of images and thus the PSI performance. The question is therefore, what if both type of scatterers, distributed and point-like ones, are exploited in the same PSI processing?

  In this context, different denoising filtering strategies, typically employed in image processing applications to reduce additive Gaussian noise, are being adapted for SAR applications. Some examples are Non-Local Interferometric SAR (NL-InSAR) [197–199], SqueeSAR [30] or Binary Partition Tree (BPT) [200, 201], which are demonstrating an excellent performance under multiplicative speckle noise conditions. The rationale of these techniques is to improve the interferometric phase quality over statistically homogeneous areas without compromising the identification of point-like scatterers. In other words, these techniques allow the exploitation of both distributed and deterministic point-like scatterers within the same PSI processing.

  A possible future line would hence be exploring the impact of these filtering tech-

niques, using either high-resolution space-borne or GB-SAR data, over natural environments such as *El Forn de Canillo*, in order to test if some persistent scatterers may be rescued. In fact, some works may be found in the literature showing the performance of such techniques in this type of applications [30, 202–204]. Despite the nice impact in the retrieval of PSI linear displacement maps, such techniques lead to some problems during the time-series estimation (mainly due to the adaptive filtering employed) and its performance needs to be further investigated.

- **Improving APS estimation and compensation step**

  Reaching an adequate compensation of APS is a key issue for the reliability of PSI products. In this context, further investigation is required for both orbital and ground-based sensors:

  - Space-borne sensors. As seen in Section 3.4.2 of Chapter 3, both tropospheric stratification and turbulent mixing processes have been addressed at the same time. The methodology followed has been based on carrying out a filtering process, taking advantage of the particular temporal and spatial frequency behaviors of APS. In order to compensate the rapid tropospheric artifacts present in mountainous environments, the correlation window has been reduced to $500 - 250$ m meters (depending on the interferogram).

    In this context, the use of semi-empirical models, such as the solution adopted for the GB-SAR sensor, is a promising strategy in order to exploit the existent correlation between APS and height. The main advantage of such techniques is that they do not require the use of any external data. Unfortunately, its use is still an open issue in space-borne SAR sensors and requires further investigation. One possible research line could be evaluating and comparing its performance with the solution adopted in this PhD Thesis.

  - Ground-based sensors. In Chapter 4 a model-based technique accounting for high atmospheric disturbances, deeply correlated with the topography, has been presented. The technique proposed has shown an excellent performance in the mountainous environment of *El forn de Canillo*, but its performance over large-scale areas is yet unknown. A future work line could be the extension of the technique proposed in this work for the monitoring of large-scale scenarios characterized by several kilometers in range.

- **FastGB-SAR acquisition mode evaluation**

  The scanning time is a key issue in the performance of GB-InSAR techniques. As seen in Section 1.3.2.2 of Chapter 1, initially, GB-SAR sensors were based on VNA solutions. This type of architecture, based on the linear frequency sweeping of transmitted signals, presented the opportunity to design GB-SAR systems with simple electronics. On the contrary, they were characterized by a slow scanning time, many times comparable to the decorrelation of the troposphere medium, thus compromising the quality of focused SAR images for the application of GB-InSAR techniques.

  A further step was taken with the development of GB-SAR sensors based on the use of high-rate SFCW signals, such as the RiskSAR sensor. In contrast to VNA-based solutions, SFCW GB-SAR sensors are able to perform faster scans, reducing the

scanning one order of magnitude (from 10 to 1 min). Faster scans allow significant improvements in GB-InSAR performance for the estimation of ground displacements.

Despite this clear improvement, the characteristics of the illuminated scenario sometimes changes in only few seconds. These changes can be produced by either extremely-rapid local atmospheric disturbances or human activity. For this reason, prior to the application of GB-InSAR techniques, a visual inspection should be carried out in order to discard bad focused images due to instabilities in the AOI.

In this context, the company MetaSensing have recently introduced a novel GB-SAR mode concept, the FastGBSAR, allowing faster scans up to 4 seconds [81]. During the last year, the RiskSAR sensor has been updated with significant improvements in the microwave front-end and today is able to perform a complete fully-polarimetric scan mounted over a linear rail of 2 meters in only 4 seconds.

With this extremely fast acquisition mode, GB-SAR images are expected to be improved in quality and reliability. This improvement is expected to enhance final PSI products, allowing the identification of a higher number of persistent scatterers. Quantifying the improvement of the RiskSAR sensor operating under the FastGBSAR acquisition mode could be another possible future research line.

- **Orbital and ground-based PSI results combination**

  In this PhD Thesis, the use of either space-borne or ground-based SAR sensors has been proposed in order to show the feasibility of these senors for the monitoring of landslides. Nonetheless, the combination of sensors' results, taking advantage of the different acquisition geometry of each one, could be an interesting research line in order to retrieve 3D displacement vectors. Some preliminary results over the landslide of *El Forn de Canillo* are shown in the following publication [205].

A

Appendix A

Landslide Classification and Causes

This appendix shows a complete description of landslide classification and causes to ease some of the geotechnical explanations provided in this PhD Thesis.

A.1 Classification

Landslide classification is based on Varnes system [2], which contemplates two terms: the material type and the type of movement.

On the one hand, the different material types involved in landslides may be classified as follows [206]:

- **Rock**. A hard firm of mass intact and natural placed before the initiation of displacement.

- **Soil**. An aggregate of solid particles, generally minerals and/or rocks. Liquids and gases filling soil's pores are also considered of this category. At the same time soil can be divided in earth and debris:
  - **Earth**. Material containing more than a 80% of sand and finer soil.
  - **Debris**. Material containing more than a 20% of coarse particles larger than 2 mm, which is considered the upper limit of sand particles.

On the other hand, the types of movement describe how the slide movement is distributed through the displaced mass and may be classified in five distinct types [2]:

- **Falls**. Are abrupt movements of masses, such as rocks, that become separated from steep slopes or cliffs. Separation are produced due to discontinuities such as fractures or joints, and the movement occurs by bouncing, free-fall or rolling. Falls are hardly affected and influenced by gravity or mechanical weathering due the presence of interstitial water.
- **Topples**. Topples are characterized by the forward rotation of units about some pivotal point under the gravity influence and/or forces produced by adjacent units or fluids in cracks.
- **Slides**. Although the general term landslide includes many types of mass movements, the more restrictive use of the term is employed where there is a zone of weakness that separates some sliding mass from a more stable subjacent material. There are two major types of slides:
  - *Rotational slide.* When the surface of rupture is curved concavely uphill and the slide movement is approximately rotational from a parallel axis to the ground surface and transverse across the slide movement.
  - *Translational slide.* When the slide mass moves along an approximately planar surface with some little rotation or backward tilting. Typically, the sliding mass consists of a single unit that moves down-slope as a coherent mass.
- **Lateral Spreads**. Lateral spreads are characteristic since they usually occur on gentle slopes or flat areas. The main type of movement is lateral accompanied by shears or fractures. The failure is caused by liquefaction, i.e., the process in which saturated sediments (usually sands and silts) are transformed from a solid into a liquefied state.
- **Flows**. There are five basic categories of flows that may be classified as follows:
  - *Debris Flows.* A debris flow consists of a rapid movement of mass in which a combination of loose soil, rock, organic matter, air and water produces a slurry that moves down-slope. Debris flows are commonly caused by intense surface-water flows (mainly due to heavy rains or snow melt), that erodes and mobilizes loose soil or rock on steep slopes. This phenomenon is often associated with steep gullies. Fires that denude slopes of vegetation intensify the probability of slopes to debris flows.
  - *Debris Avalanche.* This is a category of very rapid to extremely rapid debris flow.
  - *Earth flow.* Earth flows are based on a down-slope viscous flow of fine-grained

Type of Movement	Type of Material		
	Rock	**Debris**	**Earth**
Falls	Rock fall	Debris fall	Earth falls
Topples	Rock topple	Debris topple	Earth topple
Slides	Rock slide	Debris slide	Earth slide
Lateral Spreads	Rock spread	Debris spread	Earth spread
Flows	Rock Flow	Debris flow	Earth flow
Complex	Combination of two o more types of movement		

Table A.1: Mass movement classification based on process type and material (modified from [3]).

materials or clay-bearing rocks on moderate slopes that have been saturated with water, and move under the pull of gravity.

- *Mud Flow.* A mud flow corresponds to a category involving to very rapid from extremely rapid debris flows that have become partially or fully liquefied by the addition of significant amounts of water to the source material (containing at least 50 percent sand-, silt-, and clay-sized particles).
- *Creep.* A creep, sometimes called cold flow, corresponds to the trend of a solid material that moves slowly or displaces permanently under the influence of mechanical stresses, but too small to produce shear failure.

A classification system based on Varnes system is depicted in Table A.1. The most common types of landslides are illustrated in Fig. A.1.

A.2 Causes

Causes of landslides are related to instabilities in slopes, generally over mountainous environments, and are the reasons that a landslide occurred in a certain location at a concrete instant. Landslide causes are listed in table Table A.2, and include geological factors, morphological factors, physical factors and factors associated with human activity.

How these factors are related is of crucial importance for understanding what causes landslides and evaluating the impact of human activity. Typically, several number of elements contribute to activate a landslide, but often there is only one cause that triggers the displacement of the sliding material.

Engineers and geologists should evaluate slope stability and landslide threats during development assessment in order to implement effective and timely remedial measures to ensure the safety of people living in such regions.

GEOLOGICAL CAUSES
(1) Plastic weak materials
(2) Sensitive material
(3) Collapsible material
(4) Weathered material
(5) Sheared material
(6) Jointed or fissured material
(7) Adversely oriented mass discontinuities
(8) Adversely oriented structural discontinuities
(9) Contrast in permeability and its effects on ground water contrast in stiffness
GEO-MORPHOLOGICAL PROCESSES
(1) Tectonic uplift
(2) Volcanic uplift
(3) Glacial rebound
(4) Fluvial erosion of the slope toe
(5) Wave erosion of the slope toe
(6) Glacial erosion of the slope toe
(7) Erosion of the lateral margins
(8) Subterranean erosion (solution, piping)
(9) Deposition loading of the slope or its crest
(10) Vegetation removal (by erosion, forest fire, drought)
PHYSICAL PROCESSES
(1) Intense, short period rainfall
(2) Rapid melt of deep snow
(3) Prolonged high precipitation
(4) Rapid drawdown following floods, high tides or breaching of natural dams
(5) Earthquake
(6) Volcanic eruption
(7) Thawing of permafrost
(8) Freeze and thaw weathering
(9) Shrink and swell weathering of expansive soils
MAN-MADE PROCESSES
(1) Excavation of the slope or its toe
(2) Loading of the slope or its crest
(3) Drawdown (of reservoirs)
(4) Irrigation
(5) Water leakage from services (water supplies, sewers, stormwater drains)
(6) Vegetation removal (deforestation)
(7) Mining and quarrying (open pits or underground galleries)
(8) Creation of dumps of very loose waste
(9) Artificial vibration (including traffic, pile driving, heavy machinery)

Table A.2: Landslide casual factors (modified from [3]).

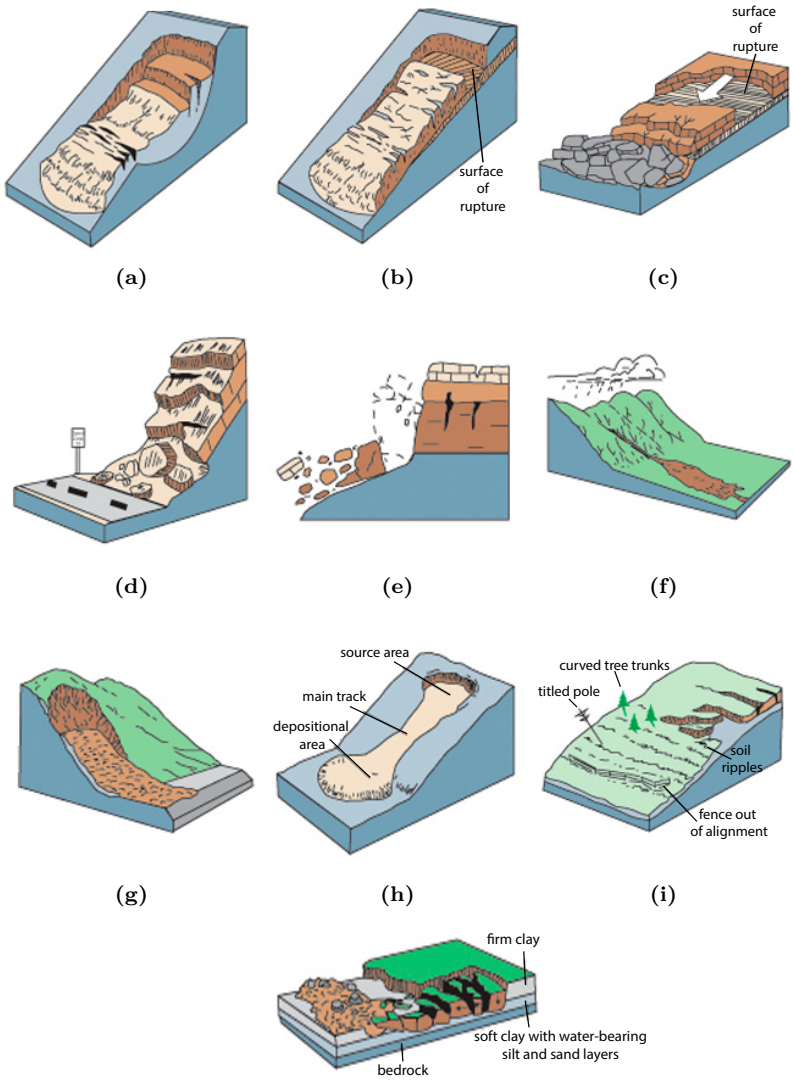

Figure A.1: Examples of different types of landslides movements (modified from [3]). (a) Roational landslide, (b) translational landslide, (c) block slide, (d) rockfall, (e) topple, (f) debris flow, (g) debris avalanche, (h) earthflow, (i) creep and (j) lateral spread.

B

Appendix B

Spotlight SAR Interferometry

High resolution imagery is a key advantage of X-band SAR sensors that are giving place to very detailed information of the Earth surface. In this context, the TerraSAR-X high-resolution sliding-spotlight mode employed in this PhD Thesis offers range and azimuth resolutions up to the meter, which are making SAR images more and more geometrically comparable to optical ones. In this Appendix, the main differences between the conventional interferometric processing of stripmap and spotlight are presented. The adequate algorithms for key processing steps, such as co-registration or azimuth Doppler filtering, are provided. Moreover, the way to extract the essential parameters from the XML TerraSAR-X header products for spotlight SAR Interferometry applications are described.

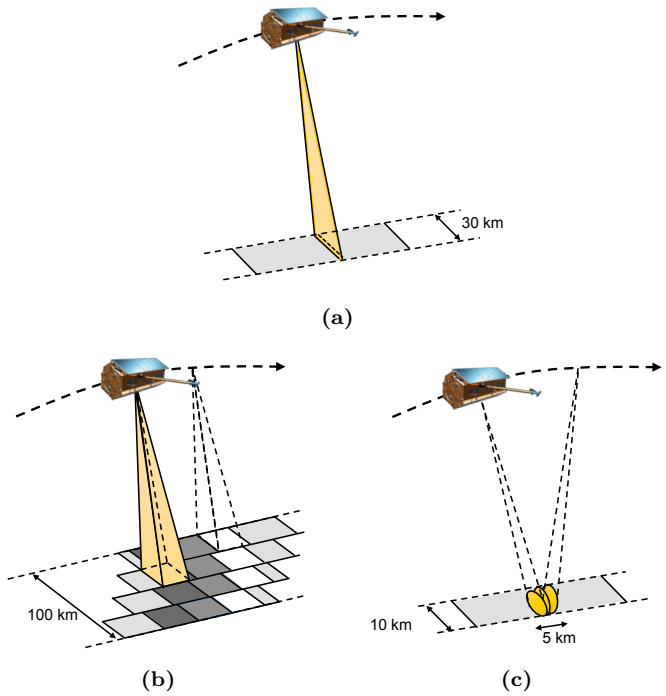

Figure B.1: Imaging SAR modes: (a) stripmap, (b) scanSAR and (c) spotlight.

B.1 SAR imaging modes

SAR sensors timing and pointing can be programmed allowing different imaging modes. Essentially, three imaging modes are typically designed to support a wide range of applications ranging from medium resolution imaging to high resolution mapping.

The different imaging modes are illustrated in Fig. B.1. In the conventional stripmap mode the ground swath is illuminated with a continuous sequence of pulses while the antenna beam is fixed in elevation and in azimuth. This results in an image strip with continuous image quality in azimuth. ScanSAR and spotlight are two operation modes of SAR systems, which improve the standard stripmap mode in two different ways. In scanSAR, the illuminated scene is extended by scanning the antenna in elevation and varying the illumination of several sub-swaths. In this mode, the antenna elevation steering is used to switch after bursts of pulses between swaths with different incidence angles. Due to the switching between the beams only bursts of SAR echoes are received, resulting in a reduced azimuth bandwidth and, therefore, in a reduced azimuth resolution. Finally, in the spotlight mode a phased array beam steering in azimuth direction is used to increase the illumination time, i.e. the synthetic aperture length. The larger aperture results in a higher azimuth resolution at the cost of worsening the azimuth scene size. The main particularities and the key processing steps to take into account to PSI applications are addressed hereinafter.

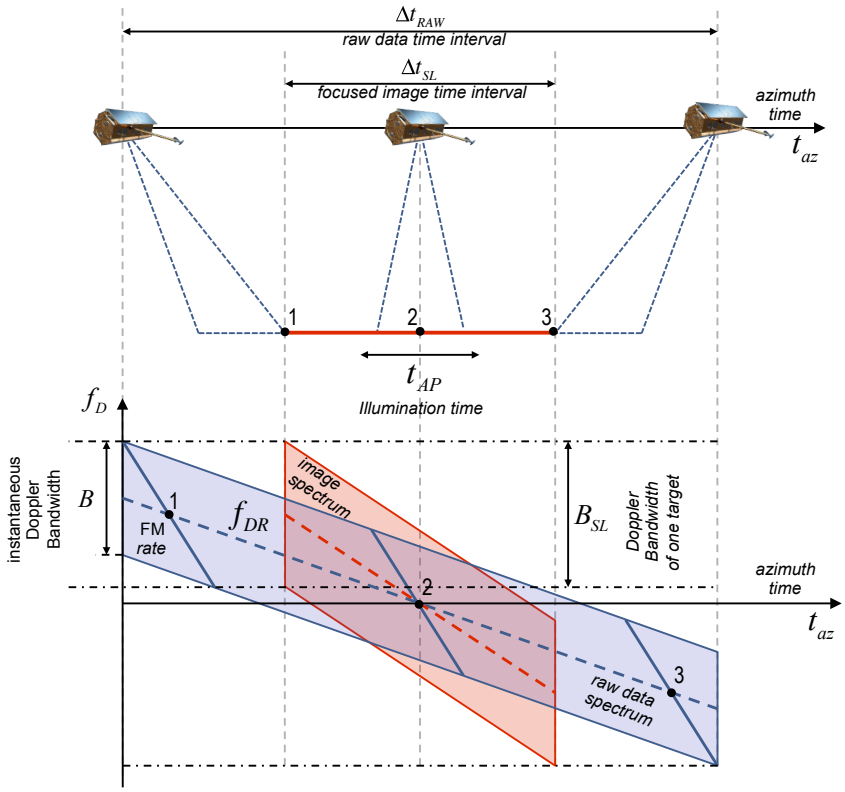

Figure B.2: Variations of the Doppler spectrum along the azimuth time of (blue) sliding-spotlight raw data and (red) the zero-Doppler focused image.

B.2 Spotlight SAR imaging mode

As seen in Section 2.1.3.2 of Chapter 2, the azimuth resolution of a SAR image is mainly determined by the illumination time t_{AP} and the Frequency Modulation (FM) rate. In stripmap mode, the azimuth resolution is roughly half the azimuth of the antenna length, where the Doppler Centroid and Doppler Rate processing parameters are azimuth invariant. It is clear that the antenna length cannot be arbitrarily reduced without the risk of causing azimuth and/or range ambiguities. In order to overcome this limitation, in the spotlight imaging mode the antenna pointing is constantly steered to keep the radar footprint illuminating a fixed spot on the ground during a time period longer than the conventional SAR aperture interval, thus improving the azimuth resolution. Indeed, this improvement is achieved at the expense of worsening the azimuth scene extension. The steering of the antenna causes a negative drift of the Doppler Centroid frequency, as shown for three targets, referred from 1 to 3, in Fig. B.2.

Defining B as the instantaneous Doppler bandwidth set by the azimuth antenna radiation pattern, the maximum synthetic aperture illumination time t_{AP} for the spotlight imaging mode may be defined as follows

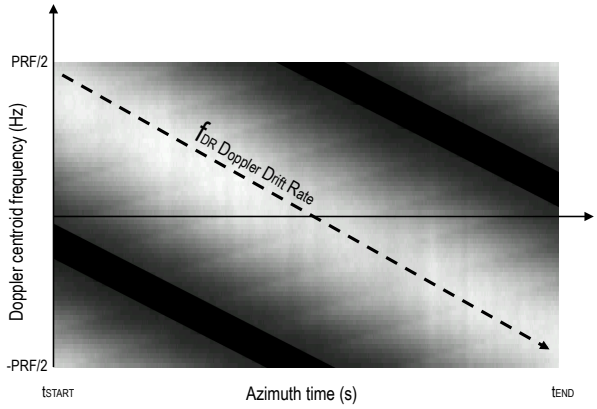

Figure B.3: Wrapped Doppler spectrum in time-frequency representation of a sliding-spotlight TerraSAR-X image corresponding to *El Forn de Canillo*.

$$t_{AP} = \frac{B}{f_{DR} - FM} \tag{B.1}$$

where f_{DR} accounts for the Doppler Drift Rate caused by the beam steering and FM represents the frequency modulation rate. As illustrated in Fig. B.2, the azimuth time interval of the zero-Doppler focused image Δt_{SL} is shorter than the raw data time interval Δt_{RAW} [97]

$$\Delta t_{SL} = \Delta t_{RAW} + \frac{B - \Delta t_{RAW} \cdot f_{DR}}{FM} \tag{B.2}$$

Following this argument, the Doppler bandwidth of the focused image B_{SL} may be expressed as follows

$$B_{SL} = t_{AP} \cdot FM = \frac{B}{f_{DR}/FM - 1} \tag{B.3}$$

As B_{SL} is greater than B, the image is sampled with a higher frequency than the PRF of the raw data. PRF of the focused image in zero-Doppler coordinates is selected to exactly fulfill Nyquist condition and avoid aliasing. However, the final spectrum of the focused image in zero-Doppler coordinates will be considerably wrapped and highly affected by a linear drift of the Doppler Centroid, see Fig. B.3, which is different from the one of the raw data, see Fig. B.2.

Finally, notice that if $f_{DR} = FM$ or $f_{DR} = 0$, equations (B.1) and (B.3) also describe staring-spotlight and stripmap case, respectively. The staring-spotlight imaging mode is reached when the squint velocity and the beam footprint ground velocity are equal. This imaging mode allows improving even more the azimuth resolution at the expense of worsening the azimuth scene extension with respect to the sliding-spotlight case.

Table B.1 show the typical parameters of the sliding-spotlight acquisition mode for the sensor TerraSAR-X employed in this PhD Thesis [97].

Sensor Parameter	Magnitude
Orbit Height	514 km
Orbit Repeat Cycle	11 days
Wavelength	3.1 cm
Full Performance Range Incidence Angle	20°-50°
Bandwidth	150 MHz
Slant Range Resolution	1.2 m
Azimuth Resolution	1.1 m
Sensor PRF	ca. 3000-6000 Hz
Product PRF	8200 Hz
Focused Bandwidth	7316 Hz
Raw Data Scene Duration	3.2 s
Zero Doppler Scene Duration	0.75 s
Azimuth Scene Size	5 km
Range Scene Size	10 km
Number of Azimuth Beams	249
FM-rate	ca. -5700 Hz/s ($@\theta = 35°$)
Antenna Bandwidth	2800 Hz
Doppler Rate f_{DC}	ca. -3600 Hz/s ($@\theta = 35°$)
Spotlight Aperture Time	1.3 s ($@\theta = 35°$)
Squint Angle Range	$\pm 0.75\circ$

Table B.1: Typical parameters of TerraSAR-X sliding-spotlight acquisition mode. Modified from [97].

B.3 Spotlight SAR Interferometry

In order to exploit a data set of coherent spotlight interferograms between SAR acquistions pairs, the standard stripmap interferometric chain (described in Chapter 2) must be adapted to face the azimuth variant spectra explained in the previous Section. In consequence, the center frequency of the interpolation kernels used for interferometric image coregistration must be adjusted in azimuth. In addition, the azimuth common-band spectral filtering needs to be updated accordingly. The latter is illustrated in Fig. B.4. Recall that, as seen in Section 2.4.1.1 of Chapter 2, only the common part of the master and slave spectra contains useful information for either InSAR or DInSAR applications.

Following this argument, the drift rate f_{DR} of the image spectrum may be calculated from the Doppler values and their zero-Doppler time differences through the first and last azimuth time of the focused scene as follows [97]

$$f_{DR} = \frac{f_{DC,n} - f_{DC,1}}{t_{DC,n} - t_{DC,1}} \tag{B.4}$$

where $f_{DC,1}$ and $f_{DC,n}$ account for the first and the last Doppler annotated values in the product and $t_{DC,1}$ and $t_{DC,1}$ their correspondent zero-Doppler corrected times.

In the TerraSAR-X case, it must be taken into account that Doppler parameters f_{DC}

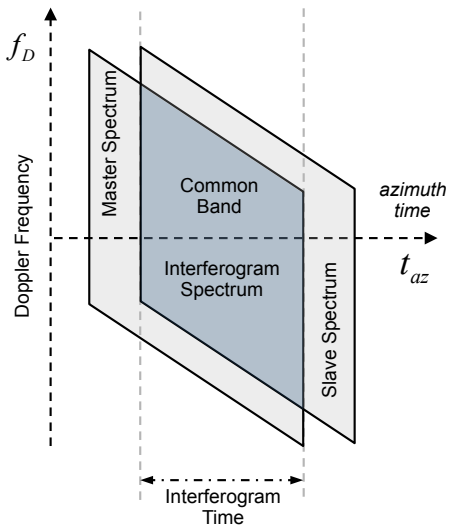

Figure B.4: Doppler spectrum of two sliding-spotlight acquisitions forming an interferogram. Only the overlapping part should be considered for InSAR applications.

in XML products are referenced to the annotated echo receive time system, hence, this axis should be converted into the zero-Doppler time reference system of the focused image as follows

$$t_{sl} = t_{RAW} - \frac{f_{DC}(t_{RAW})}{FM} \tag{B.5}$$

This fact is illustrated in Fig. B.5, which shows the Doppler variation with the azimuth time for an acquisition of *El Forn de Canillo* before and after focusing the image in zero-Doppler coordinates. Notice how the Doppler Drift Rate changes depending on the time reference system.

Once the drift rate of the focused image scene is calculated, each azimuth line is demodulated with the following chirp function parametrized with the drift rate [97]

$$c(t) = e^{-j\pi(t-t_{start})^2 f_{DR}} \tag{B.6}$$

where t_{start} refers to the azimuth start time of the scene.

As illustrated in Fig. B.6a, the spectrum now is centered on the start Doppler value. The base-banding is finally achieved by multiplying the image in the spatial domain by a phase ramp in azimuth parameterized with the zero-Doppler start value, see Fig. B.6b.

Once the image is base-banded, the co-registration, resampling and common-band filtering can be applied. After these steps, both scenes should be modulated back to their original frequency bands by multiplying them with the conjugate chirp $c^*(t)$ and classical stripmap PSI techniques may be employed.

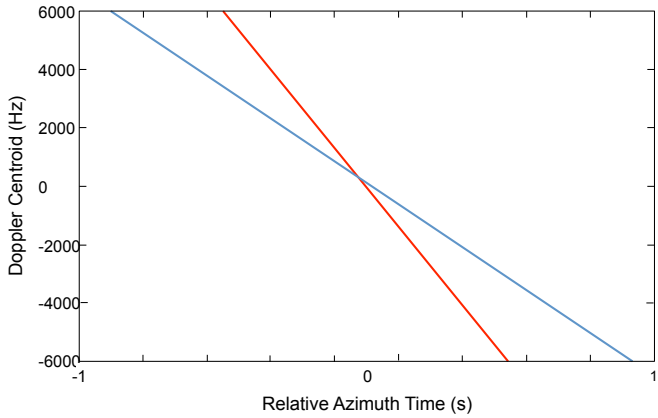

Figure B.5: Doppler variation with the azimuth time for an acquisition of *El Forn de Canillo* in (blue) raw data and in (red) zero-dopppler focused time reference system.

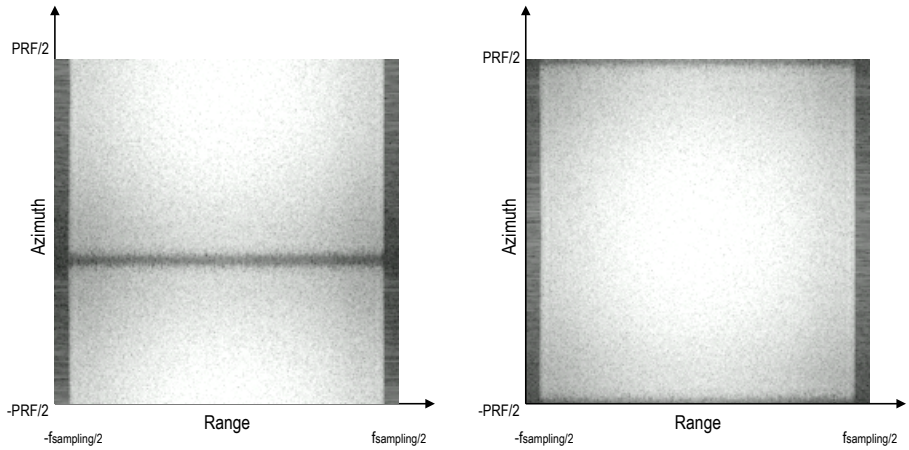

Figure B.6: Base-banding process. (a) Image spectrum after demodulating the image with a chirp function parametrized with the drift rate and (b) after applying a phase ramp to base-band the spectrum.

Finally, it is worth pointing out that sliding-spotlight images may be have different PRFs for different temporal acquisitions. This is because the SAR processor has to adapt to a wide range of incidence angles and imaging modes. Images with different PRFs should be adequately resampled tanking into account the Doppler Drift Rate above mentioned.

B.4 XML-formatted TerraSAR-X products

In this final Section, we briefly describe how the essential Doppler Centroid parameters can be extracted from the XML-formatted TerraSAR-X products and how the time system is converted from the raw data to the focused zero-Doppler time system of products.

The zero-Doppler start time t_{start} of the focused scene is extracted from

$< level1Product... >$
$< productInfo >$
$< sceneInfo >$
$< start >$
$< timeUTC > 2010-11-18T06:02:36.737922Z < /timeUTC >$

The raw data time tags of the estimated Doppler polynomials are extracted from

$< level1Product... >$
$< processing >$
$< Doppler >$
$< DopplerEstimate >$
$< timeUTC > 2010-11-18T06:02:35.410196Z < /timeUTC >$

The polynomial coefficient must be extracted from

$< level1Product... >$
$< processing >$
$< Doppler >$
$< DopplerEstimate >$
$< combinedDoppler >$
$< validityRangeMin > 4.28929386386531480E-03 < /validityRangeMin >$
$< validityRangeMax > 4.34229418434252737E-03 < /validityRangeMax >$
$< referencePoint > 4.31579402410392152E-03 < /referencePoint >$
$< polynomialDegree > 1 < /polynomialDegree >$
$< coefficientexponent = 0 > 5.80369261244272457E+03 < /coefficient >$
$< coefficientexponent = 1 > 2.43525257516052952E+04 < /coefficient >$
$< /combinedDoppler >$

where the Doppler Centroid as a function of the range time can be calculated as follows

$$f_{DC}(t) = < coefficientexponent = 0 > + < coefficientexponent = 1 > \cdot (t - < referencePoint >)$$

In our product, 103 Doppler polynomials were annotated. This number can be extracted from

$< level1Product... >$
$< processing >$
$< processing >$
$< numberOfDopplerRecords > 103 < /numberOfDopplerRecords >$

Finally, the FM rate, which is required to convert echo receive times to zero-Doppler times, is extracted from the two annotated Doppler Rates for the start and the end of the scene. Both Doppler Rates are given as polynomials over range. For time correction purposes, it is sufficient to use the average of the two zero-order coefficients for the whole scene.

$< level1Product... >$
$< processing >$
$< geometry >$
$< dopplerRate >$
$< timeUTC > 2010 - 11 - 18T06 : 02 : 36.103807Z < /timeUTC >$
$< dopplerRatePolynomial >$
$< validityRangeMin > 4.28929386386531480E - 03 < /validityRangeMin >$
$< validityRangeMax > 4.34229418434252737E - 03 < /validityRangeMax >$
$< referencePoint > 4.31579402410392152E - 03 < /referencePoint >$
$< polynomialDegree > 3 < /polynomialDegree >$
$< coefficientexponent = 0 > -5.40278707675475107E + 03 < /coefficient >$
$< coefficientexponent = 1 > 1.28142431956125121E + 06 < /coefficient >$
$< coefficientexponent = 2 > -2.03590115713134974E + 08 < /coefficient >$
$< coefficientexponent = 3 > 8.19900903247779665E - 04 < /coefficient >$
$< /dopplerRatePolynomial >$
$< /dopplerRate >$
$< dopplerRate >$
$< timeUTC > 2010 - 11 - 18T06 : 02 : 38.121489Z < /timeUTC >$
$< dopplerRatePolynomial >$
$< validityRangeMin > 4.28929386386531480E - 03 < /validityRangeMin >$
$< validityRangeMax > 4.34229418434252737E - 03 < /validityRangeMax >$
$< referencePoint > 4.31579402410392152E - 03 < /referencePoint >$
$< polynomialDegree > 3 < /polynomialDegree >$
$< coefficientexponent = 0 > -5.40283723024106803E + 03 < /coefficient >$
$< coefficientexponent = 1 > 1.29454465965671744E + 06 < /coefficient >$
$< coefficientexponent = 2 > -1.51413796442563385E + 08 < /coefficient >$
$< coefficientexponent = 3 > 8.28295731691976699E - 04 < /coefficient >$
$< /dopplerRatePolynomial >$
$< /dopplerRate >$

C

Appendix C

Side-Lobe Cancelation in PSI Applications

This Appendix presents a mathematical description and analysis of the SVA approach employed in this PhD Thesis (Section 3.2.4 of Chapter 3). This methodology has been successfully integrated in the SubSoft processor to improve the performance of the CPT.

C.1 Spatially Variant Apodization basics

SVA is based on a spatial adaptive filtering function to achieve side-lobe reduction with no loss of image resolution [180]. Its idea is similar to Capon's spectral estimator [207], but SVA is simplified by limiting the possible filters to the cosine-on-pedestal family weighting functions.

In the spatial domain, the cosine-on-pedestal family impulse response is given by a 3×3 point function

$$\begin{pmatrix} w_m w_n & w_n & w_m w_n \\ w_m & 1 & w_m \\ w_m w_n & w_n & w_m w_n \end{pmatrix} \tag{C.1}$$

where w_m and w_n are the coefficients in the range and azimuth directions to build the whole $2D$ family of cosine-pedestal functions.

The resulting output weighted pixel is obtained by a convolution in the image domain

$$g'(m,n) = g(m,n) + w_m w_n P + w_m Q_m + w_n Q_n \tag{C.2}$$

where $g'(m,n)$ is the original pixel value, m and n are the data-array pixel indexes. Q_m, Q_n and P may be expressed as follows

$$\begin{aligned} Q_m &= g(m-1,n) + g(m+1,n) \\ Q_n &= g(m,n-1) + g(m,n+1) \\ P &= g(m-1,n-1) + g(m+1,n+1) + g(m-1,n+1) + g(m+1,n-1) \end{aligned} \tag{C.3}$$

The solution is based on finding the weighting factors (w_m, w_n) in range and azimuth directions that minimize the square of the absolute value of the convoluted image in the spatial domain $|g'(m,n)|^2$ with $0 \leqslant \{w_m, w_n\} \leqslant 1/2$ that corresponds to the classical aperture functions.

At this stage, two different approaches may be considered, minimizing the real and the imaginary parts jointly or separately. For simplicity, and due to its computational efficiency, the discussion and examples in this PhD Thesis have concentrated on the separately minimization solution of the algorithm under a simultaneous and uncoupled two dimensional approach.

Notice that equation (C.2) is, for a given w_n, a linear function of w_m. Similarly, for any given w_m, $g'(m,n)$ is a linear function of w_n. Therefore, for any two (w_m, w_n) inside the interval $[0, 1/2] \times [0, 1/2]$, the value of the pair $(w_m, 0)$ $\left(w_m, {}^1\!/_2\right)$ will be lower or equal than the value for (w_m, w_n). Following an analogous arguments it can be easily observed that the maximum and minimum values can be found in one of the four evaluated corners of the interval: (0,0), (0,1/2), (1/2,0) and (1/2,1/2). This allows computing the weighting factors only evaluating the function in the four corners of the interval. Since $g'(m,n)$ is monotone in w_m and w_n, the zero value can only be obtained

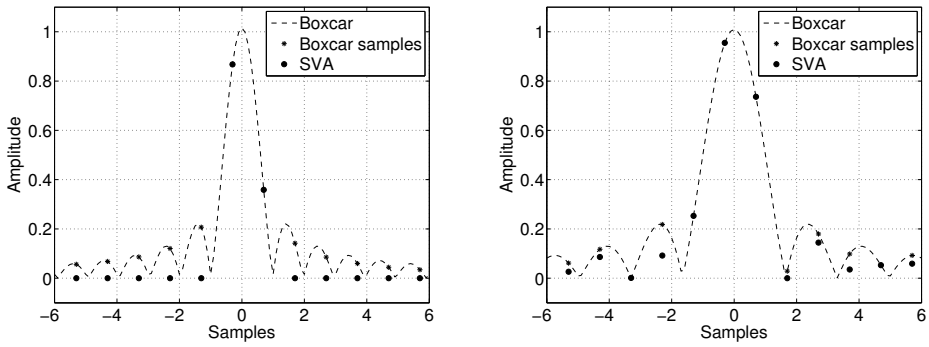

Figure C.1: Apodization with (a) $f_s = BW$ reaching a total side-lobe cancellation and (b) with $f_s = 1.6 \cdot BW$ where a total side-lobe cancellation is not possible.

if there have been changes of sign within the interval. The algorithm implementation can be summarized in the following points:

- Compute $g'(m,n)$ in the four corners of the interval: (0,0), (0,1/2), (1/2,0) and (1/2,1/2).
- If any of them are opposite in sign, set the value of $g'(m,n)$ to zero.
- Otherwise, choose from the evaluated four values these that gives the less magnitude.

Some considerations must be taken into account before applying SVA. On the one hand, data spectrum should present an ideally rectangular-shape. Therefore, any spectral weighting in both range and azimuth should be removed. On the other hand, the spectrum has to be perfectly base-banded and any spectral shift induced by the Doppler Centroid has to be considered. Finally, the first version of the algorithm requires data to be sampled at exactly the Nyquist frequency (or a multiple). Fig. C.1a shows how under ideal conditions a total side-lobe cancellation can be reached. As the sampling rate increases moving away from an integer Nyquist frequency, side-lobe cancellation becomes impossible, as illustrated in Fig. C.1b.

To face this problem the image can be interpolated to have a sampling frequency corresponding to an integer number of the bandwidth [208]. Another option was proposed in [209] by Smith that uses a generalized cosine-on-pedestal weighting family of functions that work for any sampling rate. Fig. C.2 shows its improved performance for the high oversampled case shown in Fig. C.1b.

Despite this improvement, if data is heavily oversampled the algorithm is not able to reach a total side-lobe cancellation. This technique can be improved by increasing the number of degrees of freedom in the optimization process, as it is presented in [210]. Anyway, the version described in [209] reaches an acceptable side-lobe cancellation with moderate oversampling and is the one implemented in this PhD Thesis.

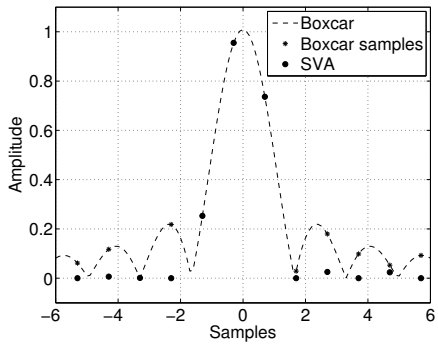

Figure C.2: Apodization with with $f_s = 1.6 \cdot BW$ and Non Integer Nyquist Sampling Rate method. Improved performance in side-lobe cancellation.

C.2 Application of SVA in PSI

C.2.1 Impact of undesired artifacts in the selection of PSCs

As commented above, in a SAR system the PSF of a point target, basically a bi-dimensional *sinc*, extends to more than a single resolution cell. The band limited character of SAR imaging causes the appearance of side-lobes and the image oversampling provoke the main lobe to extend beyond a single pixel. In other words, the contribution of a single scatterer appears not only on the pixel where it is located but also on the neighboring ones.

These undesired artifacts are more visible in urban environments where man-made structures behave as strong scatterers. Despite this, with the arrival of the second generation of SAR sensors (such as the German satellite TerraSAR-X or the Italian constellation CosmoSky-Med), which work at higher frequencies allowing larger bandwidths, the ground resolution has been significantly improved (up to the meter) compared with its predecessors (such as ERS or ASAR). Its seems clear that it is more frequent to find point-like scatterers also in natural environments, i.e, a single dominant scatterer within the resolution cell, such as outcrops or exposed rocks. Whatever the scenario, side-lobes are usually clearly visible when strong scatterers are located in low reflectivity areas and their properties are preserved along the *sinc*.

As seen in Section 3.2.3 of Chapter 3, one of the common methods in PSI is the well-known PS approach [19], which relies in associating the phase stability of the target with its amplitude stability. PSs are characterized by a low temporal amplitude dispersion, D_A, which is defined as the the standard deviation of the pixels' amplitude along time, σ_A, divided by its mean, m_A. As seen in this PhD Thesis, PSs can be selected evaluating their dispersion index and setting an appropriate threshold (typically $D_A < 0.25$). Both the redundant information around the main lobe and the side-lobes of high-quality pixels will be present in the final pixel selection. The same reasoning may be applied to the TSSC approach presented in Chapter 7. If a target is a SCS, its spectral properties will preserved along its PSF and, as a consequence, all these undesired artifacts will belong to the final selection of pixel candidates.

The results showed in this Appendix are addressed to the D_A approach. In Chapter 7, some results are shown for the TSSC approach. A set of 51 TerraSAR-X images of the city of Murcia, Spain, covering the period corresponding from July 2008 to April 2010 have been used in order to illustrate the impact of side-lobes in PSI pixel selection. The D_A threshold has been set to 0.25, which corresponds to a phase standard deviation of about 15°. Fig. C.3a shows an area of the SLC with a high-power scatterer in a region characterized by a low coefficient of back-scattering. As shown in Fig. C.3b, the main lobe and the side-lobes present in the AOI exhibit low values of D_A and, therefore, both undesired artifacts are finally selected as PSCs, see Fig. C.3c.

C.2.2 SVA impact on SAR images

As seen, SVA ideally provides total or partial side-lobe reduction and a significant resolution enhancement while preserving both the amplitude and phase of SLCs. Fig. C.3d shows the impact of using SVA directly in a SLC. Notice how effectively the side-lobes are totally cancelled and how the main lobe broadness is reduced reaching the resolution corresponding to the unweighted image.

When working with real data under complex scattering behaviors, like combinations of different target responses within the same resolution cell, the performance of SVA worsens. In fact, as the target PSF moves away from the ideal bi-dimensional *sinc* of a point-like scatterer, the impact of SVA filtering becomes higher, especially, on the amplitude but also in the phase. The use of SVA filtered images under the PS approach drive to an overestimation of the D_A map and thus to the loss of a considerable amount of pixels candidates. In addition, the phase is also affected but not as much as the amplitude. For this reason, it is proposed to use SVA only to detect the positions of the side-lobes and refine the position of the main lobe but keeping pixels' amplitude and phases from original SLCs.

In order to illustrate this issue, a deterministic point-like scatterer of unitary amplitude has been simulated in its spectral domain by an ideal rectangular-shape spectrum. To simulate the non-idealities of the target, its ideal spectrum has been corrupted adding an uncorrelated complex circular Gaussian noise. The noise standard deviation has been gradually incremented from 0.05 to 1. For each value of noise, 5000 realizations of the amplitude and phase differences between the simulated image before and after applying SVA have been computed. The results are shown in Fig. C.4 where the mean of the differences are represented by the dotted line while the the vertical bars represent the values of dispersion. This study reveals how the amplitude and phase dispersions increase as the spectrum is being distorted. Notice how the amplitude is more affected than the phase since SVA filtering do not preserve the PSF energy.

C.2.3 Side-Lobe Risk Map

In this section, it is proposed a new way to take advantage of SVA filtering through the elaboration of a risk map with information of the side-lobes locations. This mask will is referred as Side Lobe Risk Map (SLRM). Side-lobes can be regarded as a local phenomenon as its impact depends more on the background reflectivity than on the side-

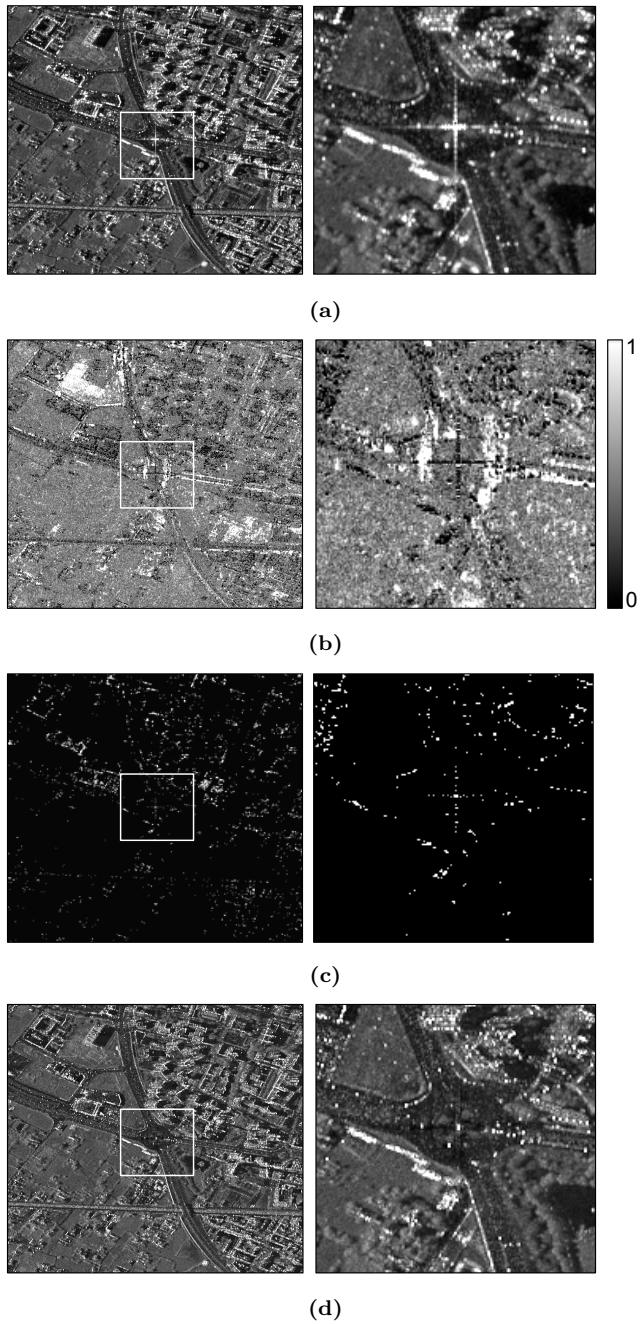

Figure C.3: Effect of (a) high-reflectivity scatterers in PSI pixel selection using the PS approach. (b) D_A index. (c) Pixel selection with a D_A threshold of 0.25. (d) Image after applying SVA showing a clear resolution enhancement and a total side-lobe cancellation.

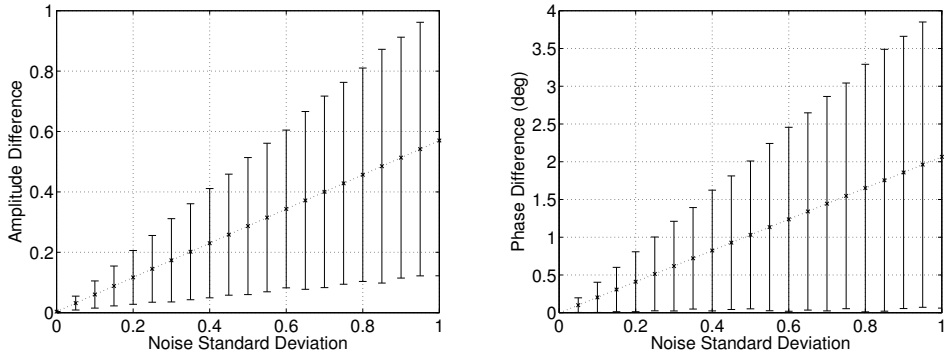

(a) **(b)**

Figure C.4: Effect of SVA filtering in (a) amplitude and (b) phase for non-ideal point-like scatterers.

lobe amplitude itself. Moreover, as the detection is within the frame of PS analysis for a possible side-lobe, the number of occurrences along the stack of images is the key factor. For this reason, the SLRM is generated considering the number of occurrences of the side-lobes along the stack. The algorithm to derive the SLRM can be summarized as follows:

- Starting with the first image of the data-set, when a side-lobe is detected by the SVA algorithm their occurrence is stored. A side-lobe is present when there is a change in the sign of $g'(m,n)$ for any of the four evaluated values of the interval $[0,1/2] \times [0,1/2]$. If not, the stored value is zero because it was not detected any side-lobe.
- The process is repeated for all images of the data set.
- Finally, for each pixel it is made an average of the stored values leading to a map directly related with the number of occurrences along the whole stack.

For instance, an ideal side-lobe present in all images will reach a value of 1 in the SLRM. On the other side, side-lobes appearing only in few images will have values closer to zero. The values of the map can thus be related with the probabilities of being a side-lobe. Pixels set to zero have no risk of being a side-lobe.

Fig. C.5a shows the SLRM obtained in the area of the strong scatterer presented in Fig. C.4. All side-lobes clearly visible in the amplitude image have been selected as side-lobes with a high degree of confidence as well as other candidates with lower back-scattering. There is no rule that clearly indicates where to place the threshold for considering that a detected artifact is a side-lobe or not. Being too restrictive, this is setting the value near to one. On the contrary, setting the threshold to zero will cause to reject pixels that in practice are very unlikely to be side-lobes, for instance because they are considered as side-lobes just in a single image. Thus, it seems reasonable to use thresholds over 0.5 that will correspond to side-lobes present in more than half of the images of the data set. Finally, a mask with those points fulfilling the threshold established above can be applied to the map of PSCs in order to eliminate all these

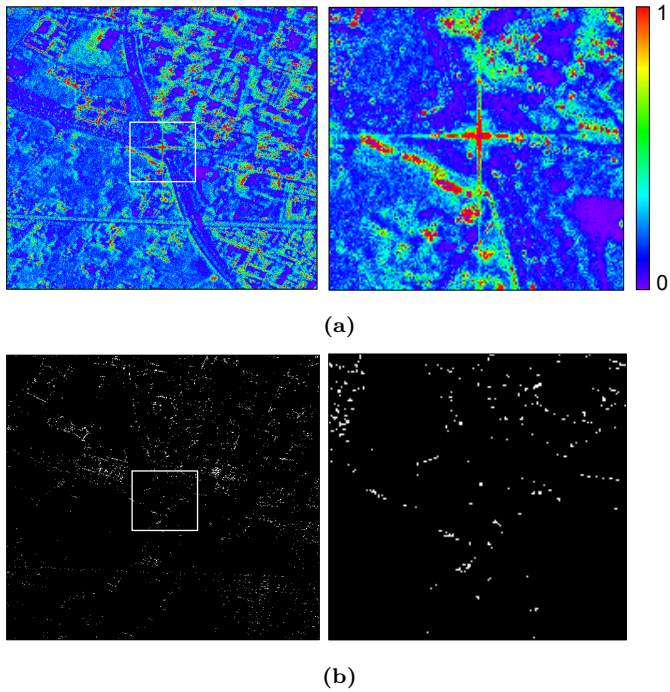

Figure C.5: Total side-lobe cancellation in PSI. (a) SLRM. (b) Selected pixels after applying the method proposed with a SLRM > 0.5.

redundant information from the final pixel selection. Fig. C.5b shows the distribution of surviving pixels after applying the methodology described.

Fig. C.6a shows the histogram of the SLRM values corresponding to potential side-lobes. The zero values, this is no side-lobes, have been removed from the histogram. Most of the detected artifacts correspond to pixels with low probabilities of being a side-lobe. More interesting is the cloud plot of the D_A indexes as a function of the SLRM values shown in Fig. C.6b. As expected, for high SLRM values the D_A index is in general low and as we reduce the SLRM the range of D_A indexes increases. In other words, D_A index is not correlated with SLRM values for pixels with low risk of being a side-lobe.

Finally, Fig. C.7 presents the percentage of surviving pixel candidates applying the SLRM-derived mask for different thresholds. It can be seen how around the 3% of the PSs detected are identified as high-risk side-lobes (SLRM> 0.5). Anyway it is difficult to establish a threshold as in the complex scenario of an urban area it is difficult to distinguish among side-lobes and main lobes. What it is clear that the threshold of 0.5 allows removing those side-lobes clearly visible.

The methodology proposed has been applied in both urban and natural environments presenting an excellent performance. In addition, this technique has been also applied to the TSSC phase quality estimator presented in Chapter 7. As illustrated in this Chapter, excellent results have been obtained using this methodology when either the TSC or the TSE approaches are employed. Finally, it must be pointed out that the loss of range

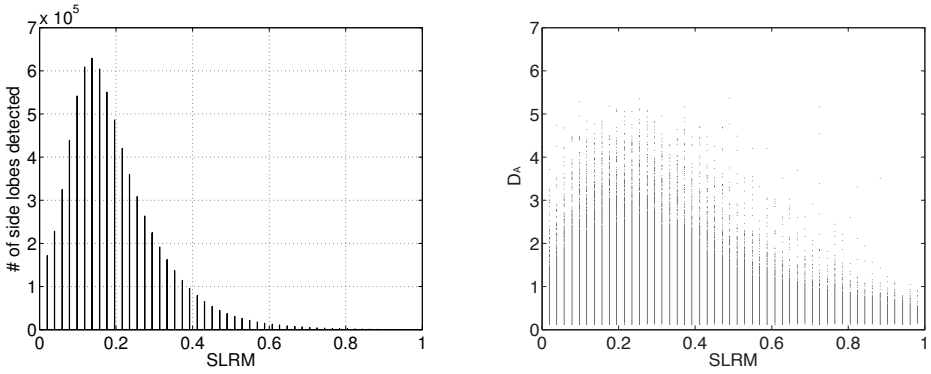

(a) **(b)**

Figure C.6: (a) SLRM histogram distribution. (b) Cloud plot of D_A for different SLRM threshold values.

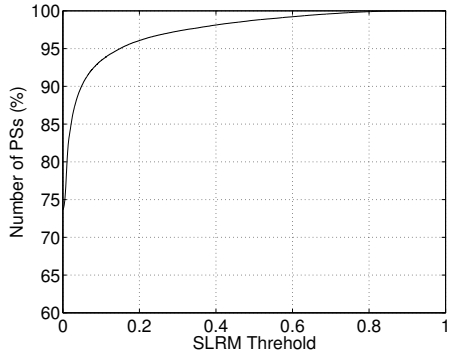

Figure C.7: Number of pixels selected in function of the detected side-lobes removed in terms of SLRM values.

resolution due to the sublook generation may be partially overcome since, owing to the SVA-based method proposed, the selected main lobes present the theoretical resolution of the original image.

This methodology has been published in the journal *IEEE Geoscience and Remote Sensing Letters*. For further information refer to citation [211].

D

Appendix D

Model Adjustment Function Properties

In Section 3.3.2 of Chapter 3, we have seen how the objective of the minimization step of the CPT consists of adjusting a linear phase model to the inteferometric phases in order to find the optimal values of $\{\Delta v, \Delta\varepsilon\}$ that minimizes the MAF. Understanding the dynamics of the MAF is hence of great importance in order to reach a good minimization process. In this Appendix two important considerations are put forward. On the one hand, the sensitivity of MAF to the spatial and temporal baselines distribution is illustrated. Moreover, since the MAF function can be interpreted as a normalized summation of 2D sinusoidal functions at different frequencies, the location of ambiguities is discussed.

D.1 Sensitivity to spatial and temporal baseline distributions

This first Section deals with the impact of spatial and temporal baseline distributions in the shape of the MAF.

As seen in Section 3.3.2 of Chapter 3, the MAF may be expressed as follows

$$\Gamma(arc_{m,n}) = 2 \cdot \left(1 - \tfrac{1}{N_{\text{int}}} \cdot \sum_{i=1}^{N_{\text{int}}} \text{Re}\left\{e^{-j\left(\Delta\varphi_i(T_i,B_{n,i},arc_{m,n}) - \Delta\varphi_i^{\text{model}}(T_i,B_{n,i},arc_{m,n})\right)}\right\}\right), \quad \text{(D.1)}$$

where N_{int} account for the number of interferograms, $\Delta\varphi^i$ refers to the interferometric phase increment of a certain relationship $arc_{m,n}$ for a generic $i{-}th$ interferogram, $\Delta\varphi_i^{\text{model}}$ for its linear model, T_i and B_i are the temporal and spatial baselines, respectively, λ indicates the wavelength, R_i is the sensor to target distance and θ_i refers to the incidence angle.

As seen in (D.1) the MAF function is sensitive to the 2D sampling given by the spatial and temporal baselines distribution of the interferograms involved in the linear block of the CPT. In this context, a poor sampling in either the temporal or the spatial baselines can lead to systematic errors that could propagate and affect the whole estimation over the AOI even over high-coherent scenarios.

The sampling of the spatial and temporal baselines hence provides the accuracy in the estimation of the topographic error and the linear velocity increments, respectively. The maximum values of baseline at both dimensions characterize the width of the valley around the minimum. Data sets characterized by larger baseline limits, always uniformly distributed, will result in narrower valleys, thus leading to a more precise estimation of the linear parameters.

In order to illustrate this, Fig. D.1 is presented. In this figure the MAF over a simulated scenario free of noise composed by 109 interferograms uniformly distributed in terms of temporal baseline (between 11 and 365 days) is presented. R, θ, λ and the revisiting time have been defined according to TerraSAR-X setting parameters. Fig. D.1a and Fig. D.1b illustrates the shape of the MAF employing a spatial baseline distribution between -100 and 100 meters, and -30 and 30 meters, respectively. Notice how smaller baselines lead to broader valleys in the MAF, thus worsening the precision during the estimation of the topographic error increment. As small perturbation due to the presence of noise in Fig. D.1b can lead to a significant error during the minimization. Contrarily, it must be taken into account that increasing the baselines lead to major decorrelation phenomena. There is hence a clear limitation between reaching a good precision of the linear parameters in terms of the valley width and minimizing decorrelation phenomena in terms of interferograms selection. Typically, temporal and spatial baseline limits are fixed in order to minimize decorrelation phenomena. Indeed, if noise is minimized the minimization becomes easier. At the same time, uniform distributions with not too restrictive limits are desired in order to make easier the minimization step in terms of the shape of the MAF.

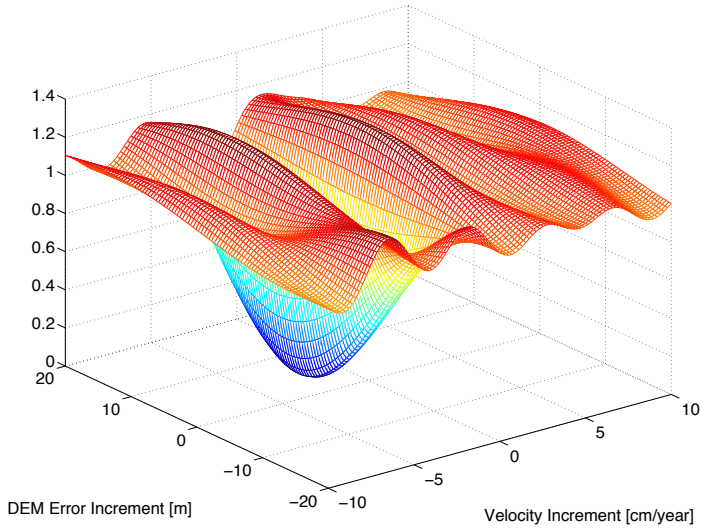

(a)

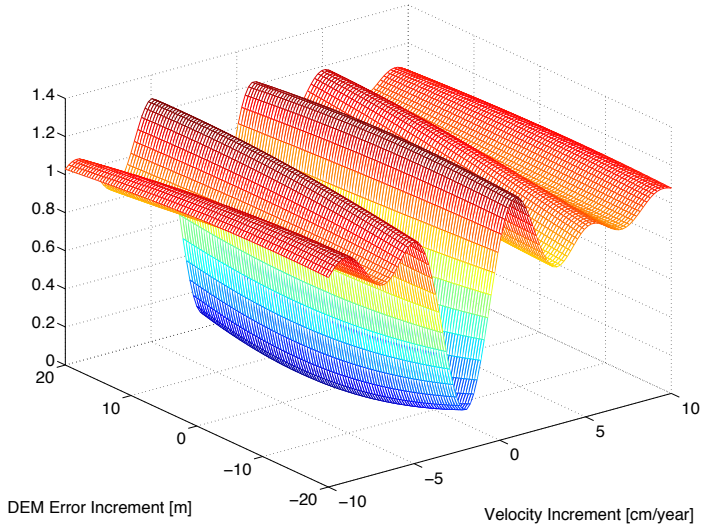

(b)

Figure D.1: MAF shape for different spatial baseline distributions. (a) Spatial baselines distribution between −100 and 100 meters. (b) Spatial baselines distribution between −30 and 30 meters. The link has been generated to present a linear velocity increment equal to −2 cm/year and a topographic error increment of 5 meters.

D.2 Ambiguities

This Section deals with the negative impact of ambiguities during the minimization process.

The MAF function may be seen a normalized sum of 2D sinusoidal functions at different frequencies provided for the temporal and spatial baseline of each interferogram

$$f_i = \left[\frac{2T_i}{\lambda}, \frac{2B_{n,i}}{\lambda R_i \sin\theta_i}\right], \tag{D.2}$$

where T_i and B_i refer to the the temporal and spatial baseline of a generic $i-th$ interferogram, respectively, λ indicates the wavelength, R_i is the sensor to target distance and θ_i refers to the incidence angle. Following this argument, the minimization of the cost function is equivalent to find the bidimensional frequency of the complex sinusoid derived from the linear model seen in (3.21)

$$\Delta\varphi_i^{\text{model}}(T_i, B_{n,i}, arc_{m,n}) = \frac{4\pi}{\lambda}\cdot T_i \cdot \Delta v(arc_{m,n}) + \frac{4\pi}{\lambda}\cdot\frac{B_{n,i}}{R_i\sin\theta_i}\cdot\Delta\varepsilon(arc_{m,n}) \tag{D.3}$$

Since the MAF function is equivalent to a normalized sum of 2D sinusoidal functions at different frequencies (as seen in (D.2)), the presence of ambiguities should be considered in order to obtain reliable results. The period of a function composed by periodic functions (if it makes sense, i.e., when the ratio of periods is rational for all the elements) is defined as the least common multiple of the periods of the component functions. This applies for the linear velocity increment axis, in which the temporal baselines are multiples of the satellite revisiting time, but rarely to the topographic error increment, since the spatial baselines are typically randomly distributed along the orbital tube.

Defining the minimum temporal baseline difference as $\Delta T_{\min}$ the distance between ambiguities is given by the following expression

$$\Delta v_{amb} = \frac{\lambda}{2\cdot\Delta T_{\min}} \tag{D.4}$$

Under this formulation, the search margin during the minimization step must be set between the interval $\left[-\frac{\Delta v_{amb}}{2}, \frac{\Delta v_{amb}}{2}\right]$.

The importance of considering linear velocity increment ambiguities is illustrated in Fig. D.2. Fig. D.2a shows the MAF of a simulated case considering a uniform distribution of temporal baselines between 11 and 132 days, with a revisiting time of 11 days. The number of interferograms has been set to 109. The spatial baselines have been uniformly generated between -500 and 500 meters. The link has been simulated to present a linear velocity increment equal to -2 cm/year and a topographic error increment of 5 meters.

Notice that the minimum temporal baseline difference of 11 days locates an ambiguous minimum separated roughly 50 cm/year from the correct value. Fig. D.2b shows an horizontal profile around the minimum location of the MAF highlighting the ambiguous location of the linear velocity increment. The boundary conditions employed in this case

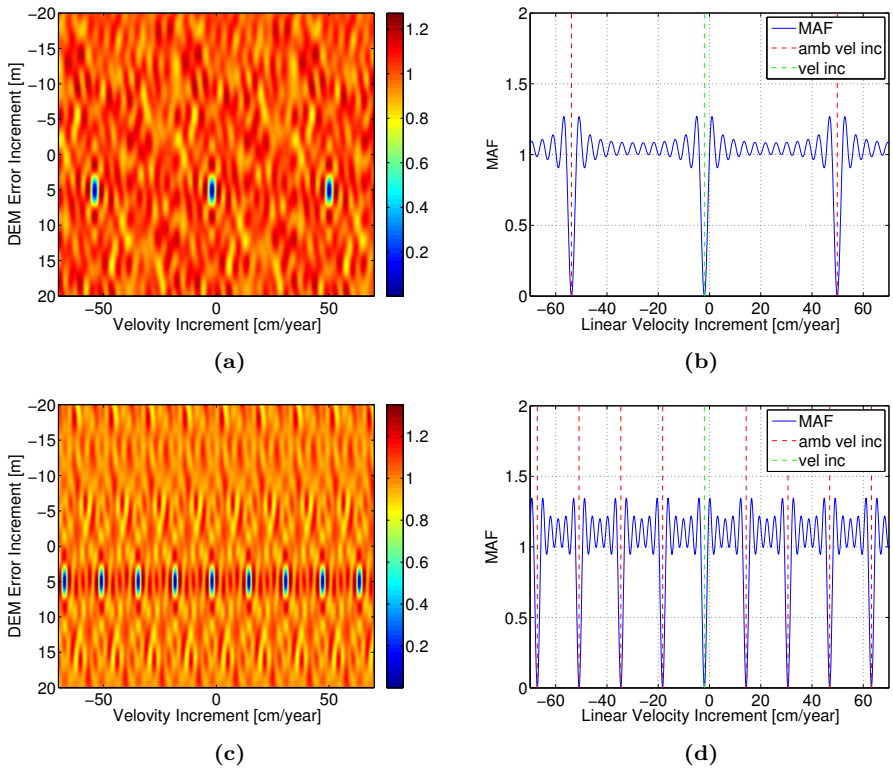

Figure D.2: MAF shape considering different revisiting times. (a) Uniform distribution of temporal baselines between 11 and 132 days, with a revisiting time of 11 days. (b) Horizontal profile of (a).(c) Uniform distribution of temporal baselines between 35 and 145 days, with a revisiting time of 35 days. (d) Horizontal profile of (c). The spatial baselines have been uniformly generated between -500 and 500 meters. The link has been generated to present a linear velocity increment equal to -2 cm/year and a topographic error increment of 5 meters.

are so high that do not represent any real practical constrain. However, Fig. D.2c and Fig. D.2d shows the MAF response for a simulated scenario with a higher revisiting time. For this case, it has been considered a uniform distribution of temporal baselines between 35 and 145 days, with a revisiting time of 35 days. Notice how the minimums are now closer at a distance of roughly 16 cm/year. Depending on the interferogram selection the MAF may present closer minimums that if it is not taken into account can lead to an erroneous estimation of the linear velocity increment.

For both the TerraSAR-X and the GB-SAR data sets employed for the monitoring of *El Forn de Canillo* this limitation does not represent any practical constrain. Since the displacement expected is low the search margin to the velocity increment is set to ± 3 cm/year.

E

Appendix E

Conjugate Gradient Method Formalism

The CGM is the most prominent iterative method for solving sparse systems of linear equations that are too large to be handled by a direct implementation, but also to solve optimization problems, such as minimization. It was mainly developed by Magnus Hestenes and Eduard Stiefe [182]. This method has been employed along this PhD Thesis for both purposes. On the one hand, it has been used in order to improve the minimization step, but also to solve the linear equation system in the integration step during the linear block of the CPT, as shown in Section 3.3.2 and Section 3.3.3 of Chapter 3, respectively. On the other hand, it has also been employed to address polarimetric optimization problem in a efficient way, as seen in Chapter 5. In this Appendix, the mathematical formalism of CGM algorithm to deal with systems of linear equations characterized by square, symmetric and positive-definite matrices of equations, is showed. Moreover, the applications of this theory in the context of this PhD Thesis is addressed. The mathematical developments showed are based in the theory described in [212].

E.1 Algorithm formalism

The CGM is one of the most popular iterative methods for solving large systems of linear equations of the form

$$\begin{cases} b_1 = a_{11}x_1 + a_{12}x_2 + ... + a_{1n}x_n \\ b_2 = a_{21}x_1 + a_{21}x_2 + ... + a_{2n}x_n \\ ... \\ b_n = a_{n1}x_1 + a_{n2}x_2 + ... + a_{nn}x_n \end{cases} \tag{E.1}$$

This system of linear equation can be expressed in matrix form as follows

$$\mathbf{Ax} = \mathbf{b} \tag{E.2}$$

where

$$\mathbf{A} = \begin{bmatrix} a_{11} & a_{12} & \dots & a_{1n} \\ a_{21} & a_{22} & \dots & a_{2n} \\ \vdots & \vdots & \ddots & \vdots \\ a_{n1} & a_{n2} & \dots & a_{nn} \end{bmatrix} \tag{E.3}$$

$$\mathbf{x} = \begin{bmatrix} x_1 \\ x_2 \\ \vdots \\ x_n \end{bmatrix} \tag{E.4}$$

$$\mathbf{b} = \begin{bmatrix} b_1 \\ b_2 \\ \vdots \\ b_n \end{bmatrix} \tag{E.5}$$

$\mathbf{x}$ corresponds to the vector of unknowns, $\mathbf{b}$ is a known vector with the observations and $\mathbf{A}$ refers to a known, square, symmetric, positive-definite matrix defining the system of linear equations. A symmetric matrix is a square matrix if it is equal to its transpose $\mathbf{A} = \mathbf{A}^T$. A matrix is positive-definite if $\mathbf{z}^T\mathbf{Az}$ is positive for every non-zero column vector $\mathbf{z}$.

Throughout this Section, some of the mathematical approaches are illustrated with the following simple sample problem

$$\mathbf{A} = \begin{bmatrix} 3 & 2 \\ 2 & 6 \end{bmatrix}, \ \mathbf{b} = \begin{bmatrix} 2 \\ 8 \end{bmatrix} \tag{E.6}$$

which is depicted in Fig. E.1.

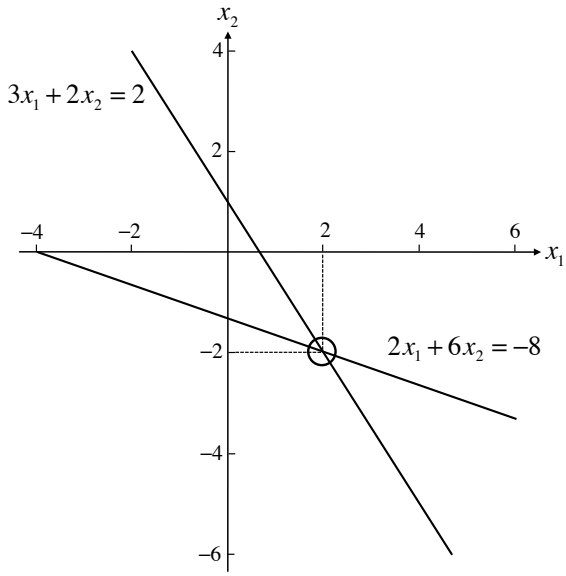

Figure E.1: Representation of the two-dimensional linear system defined in (E.6). The solution lies at the intersection of both equations and corresponds to $\{x_1 = 2, x_2 = -2\}$.

One of the key issues of CGM is to consider that looking for the unknown vector of solutions $\mathbf{x}$ is totally equivalent to find the minimum value of the following quadratic function

$$f(\mathbf{x}) = \frac{1}{2}\mathbf{x}^T\mathbf{A}\mathbf{x} - \mathbf{x}^T\mathbf{b} + c, \tag{E.7}$$

since $f(\mathbf{x})$ presents its minimum value at $\mathbf{A}\mathbf{x} = \mathbf{b}$. This fact is illustrated in Fig. E.2 where the quadratic form $f(\mathbf{x})$, employing the constants of the example defined in (E.6), is depicted. The minimum of $f(\mathbf{x})$ is represented by a white dot in Fig. E.2a. Notice that this localization coincides with the solution of the equation system $\{x_1 = 2, x_2 = -2\}$.

At this point, the gradient $f'(\mathbf{x})$ may be defined as

$$f'(\mathbf{x}) = \begin{bmatrix} \frac{\partial}{\partial x_1} f(\mathbf{x}) \\ \frac{\partial}{\partial x_2} f(\mathbf{x}) \\ \vdots \\ \frac{\partial}{\partial x_n} f(\mathbf{x}) \end{bmatrix}, \tag{E.8}$$

which is a vector field that points in the direction of greatest increase of $f(\mathbf{x})$. Fig. E.3 shows the gradient vectors for the example defined in (E.6). At the bottom of the paraboloid bowl (represented by a white dot), the gradient is zero.

Form equations (E.7) and (E.8) the expression of the gradient $f'(\mathbf{x})$ may be reformulated as follows

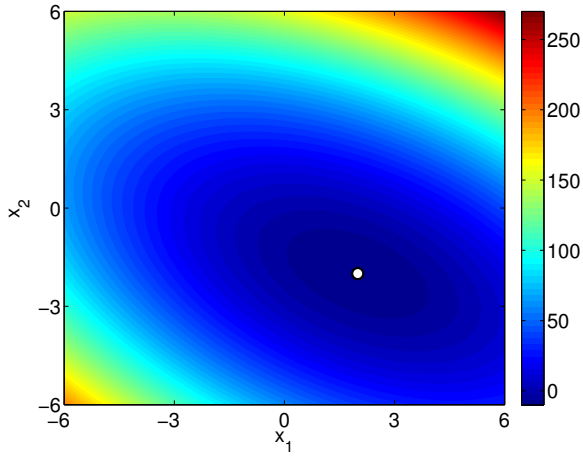

(a)

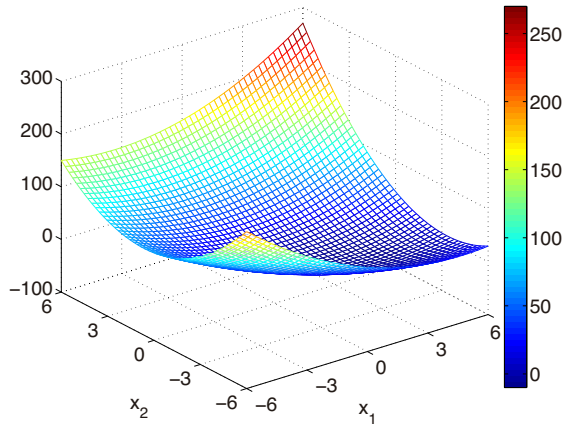

(b)

Figure E.2: Representation of the quadratic form for the two-dimensional linear system defined in (E.6) as (a) an image and as (b) a surface in the 3D space. Notice how the minimum (highlighted with a white dot in (a)) corresponds to $\{x_1 = 2, x_2 = -2\}$ coinciding with the solution of the system of equations $\mathbf{Ax} = \mathbf{b}$ defined in (E.6).

$$f'(\mathbf{x}) = \frac{1}{2}\mathbf{A}^T\mathbf{x} + \frac{1}{2}\mathbf{Ax} - \mathbf{b} \tag{E.9}$$

and if $\mathbf{A}$ is symmetric, this equation reduces to

$$f'(\mathbf{x}) = \mathbf{Ax} - \mathbf{b} \tag{E.10}$$

Notice that setting the gradient to zero, equation (E.2) is obtained, the linear system we wish to solve. Following this argument, the solution to $\mathbf{Ax} = \mathbf{b}$ is then a critical point

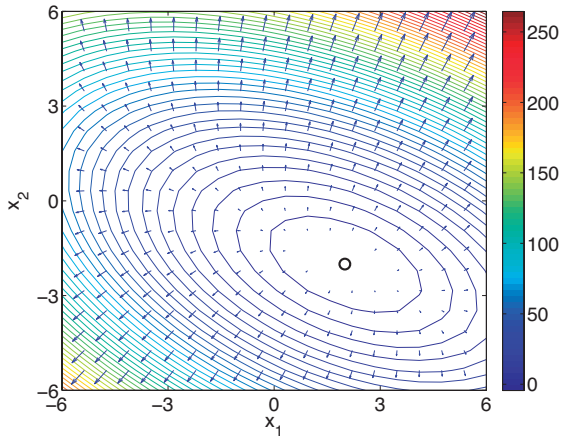

Figure E.3: Gradient $f'(\mathbf{x})$ of the quadratic form $f(\mathbf{x})$ using the constants defined in (E.6). For every point P, the gradient points in the direction of steepest increase of $f(\mathbf{x})$ and is orthogonal to the contour lines. The bottom of the paraboloid bowl is represented by a white dot.

of $f(\mathbf{x})$. If $\mathbf{A}$ is symmetric as well as positive-definite, then the solution of the linear equation system is a minimum of $f(\mathbf{x})$ and, hence, $\mathbf{Ax} = \mathbf{b}$ can be solved finding the $\mathbf{x}$ corresponding to the minimum of $f(\mathbf{x})$.

The different steps to implement CGM algorithm are given hereinafter. Starting with an initial guess, referred to as $\mathbf{x}_0$, we will search for the solution iteratively. In each iteration a metric to tell how closer we are to the solution $\mathbf{x}$ is required. This metric comes from the fact that the solution $\mathbf{x}$ is the unique minimizer of the quadratic function $f(\mathbf{x})$ and, if it becomes smaller in an iteration, this means that we are closer to the final solution. As seen above, this formulation suggests taking a first direction vector $\mathbf{p}_0$ to be the negative of the gradient of $f(\mathbf{x})$ at $\mathbf{x} = \mathbf{x}_0$, i.e., $\mathbf{p}_0 = \mathbf{b} - \mathbf{Ax}_0$. The residual at the k^{th} iteration will be

$$\mathbf{r}_k = \mathbf{b} - \mathbf{Ax}_k \tag{E.11}$$

This line of thought directly leads to the not very efficient algorithm called the steepest descent method. Starting with an initial guess at a point $\mathbf{x}_0$, as many times as needed, move from $\mathbf{p}_i$ to $\mathbf{p}_{i+1}$ by minimizing along the line in the direction of the local downhill gradient.

CGM solves the problem in a more efficient way employing the so-called conjugation constraint. The minimization process is performed through the orthonormal-type constraint, i.e, moving towards the so-called conjugate gradient directions $\mathbf{p}_i$. We say that two non-zero vectors $\mathbf{p}_i$ and $\mathbf{p}_j$ are conjugate (with respect to $\mathbf{A}$) if

$$\mathbf{dp_i^T Ap_j} = \mathbf{0} \tag{E.12}$$

Moreover, the method also require that in the next search the direction will be built

taking into account the current residue and all previous search directions. The conjugation constraint is an orthonormal-type constraint and hence the algorithm bears resemblance to Gram-Schmidt ortho-normalization. This constraint leads to the following expression

$$\mathbf{p}_k = \mathbf{r}_k - \sum_{i<k} \frac{\mathbf{p}_i^T \mathbf{A} \mathbf{r}_k}{\mathbf{p}_i^T \mathbf{A} \mathbf{p}_i} \mathbf{p}_i \tag{E.13}$$

Following that direction, the next optimal location will be located at $\mathbf{x}_{k+1} = \mathbf{x}_k + \alpha_k \mathbf{p}_k$ with

$$\alpha_k = \frac{\mathbf{p}_k^T \mathbf{b}}{\mathbf{p}_k^T \mathbf{A} \mathbf{p}_k} = \frac{\mathbf{p}_k^T (\mathbf{r}_{k-1} + \mathbf{A}\mathbf{x}_{k-1})}{\mathbf{p}_k^T \mathbf{A} \mathbf{p}_k} = \frac{\mathbf{p}_k^T \mathbf{r}_{k-1}}{\mathbf{p}_k^T \mathbf{A} \mathbf{p}_k}, \tag{E.14}$$

where the last equality holds because $\mathbf{p}_k$ and $\mathbf{x}_{k-1}$ are conjugate

Fig. E.4 shows a comparison of the convergence between the steepest descent and CGM approaches for minimizing a quadratic function associated with the linear equation system defined in (E.6). Notice that CGM converges in $n = 2$ steps while the steepest descent presents a slowly performance converging in $n = 21$ steps.

Up to this moment the most straightforward explanation of CGM algorithm has been given. This formulation requires the storage of all searching directions, the residue vectors, as well as many matrix vector multiplications. This leads to a costly computational solution. A more efficient implementation of the algorithm is based in exploiting that $\mathbf{r}_{k+1}$ is conjugate to $\mathbf{p}_i$ for all $i < k$. Following this approach, only one matrix-vector multiplication is required at each iteration. The algorithm described as follows corresponds to an equivalent formulation of the exact procedure described above:

$\mathbf{p}_0 = \mathbf{r}_0 = \mathbf{b} - \mathbf{A}\mathbf{x}_0$
$k = 0$
repeat
$\alpha_k = \dfrac{\mathbf{r}_k^T \mathbf{r}_k}{\mathbf{p}_k^T \mathbf{A} \mathbf{p}_k}$
$\mathbf{x}_{k+1} = \mathbf{x}_k - \alpha_k \mathbf{p}_k$
$\mathbf{r}_{k+1} = \mathbf{r}_k - \alpha_k \mathbf{A} \mathbf{p}_k$
if $\mathbf{r}_{k+1}$ is small than a factor of tolerance $\rightarrow$ exit loop
$\beta_k = \dfrac{\mathbf{r}_{k+1}^T \mathbf{r}_{k+1}}{\mathbf{r}_k^T \mathbf{r}_k}$
$\mathbf{p}_{k+1} = \mathbf{r}_{k+1} + \beta_k \mathbf{p}_k$
$k = k + 1$
end repeat
The result corresponds to $\mathbf{x}_{k+1}$

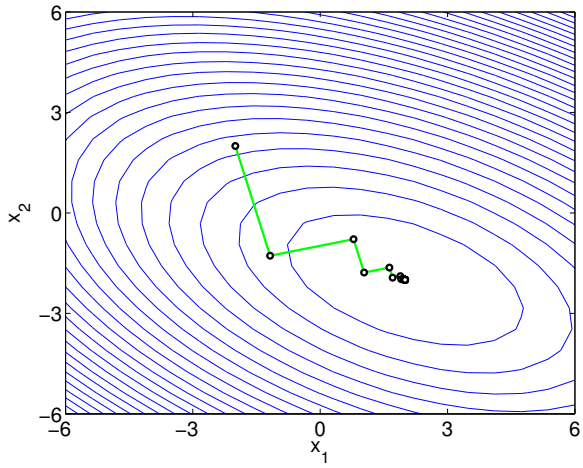

(a)

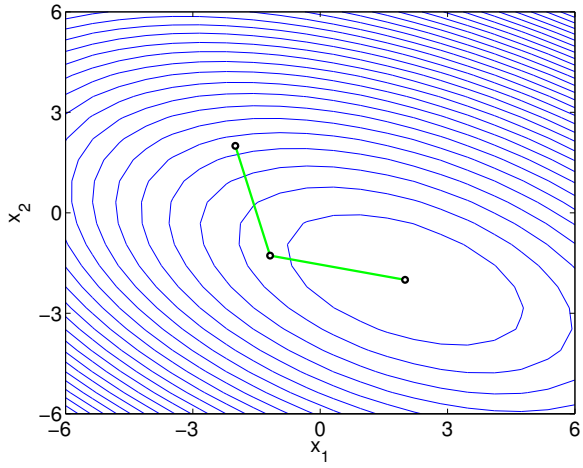

(b)

Figure E.4: A comparison of the convergence of (a) the steepest descent and (b) CGM approaches for minimizing a quadratic function associated with the linear equations system defined in (E.6). CGM converges in $n = 2$ steps. Steepest descent method converges in $n = 21$ steps.

CGM can hence be theoretically viewed as a direct method since it leads to an exact solution after a finite number of iterations lower than the size of the matrix. Nonetheless, it must be pointed out that this method becomes unstable with respect to even small perturbations. Fortunately, CGM is typically used as an iterative method (providing monotonically improving approximations $\mathbf{x}_k$ to the exact solution) and typically reaches the required tolerance after a relatively small number of iterations.

E.2 CGM Minimization in CPT

In this Section, the mathematical formulation behind CGM minimization is given. This approach has been used in order to improve the minimization step in the linear block of the CPT, as shown in Section 3.3.2 of Chapter 3, as well as to address polarimetric optimization problem in a efficient way, as seen in Chapter 5.

As seen in the previous Section, if we want to minimize a multi-dimensional function f along a certain direction $\mathbf{p}$, the gradient of the function must be perpendicular to $\mathbf{p}$ at the minimum, otherwise, the directional derivative would not be zero along that direction. In this framework, a certain function f can be approximated by a quadratic form around its minimum through its Taylor series

$$f(\mathbf{x}) = f(\mathbf{P}) + \sum_i \frac{\partial f}{\partial x_i} x_i + \frac{1}{2} \sum_{i,j} \frac{\partial^2 f}{\partial x_i \partial x_j} x_i + \ldots \approx \frac{1}{2}\mathbf{x}^T \mathbf{A}\mathbf{x} - \mathbf{x}^T \mathbf{b} + c \tag{E.15}$$

$$c = f(\mathbf{P}) \tag{E.16}$$

$$\mathbf{b} = -\nabla f|_{\mathbf{P}} \tag{E.17}$$

$$[a_{ij}] = \left. \frac{\partial^2 f}{\partial x_i \partial x_j} \right|_{\mathbf{P}} \tag{E.18}$$

where the matrix $\mathbf{A}$ refers to the Hessian matrix of the function at $\mathbf{P}$ and its composed by the second partial derivative matrix of the function.

Once the quadratic form is obtained, a parallelism can be followed with respect to the theory seen in the previous Section to solve systems of linear equations. As seen in (E.10), the gradient of f may be easily calculated as $f'(\mathbf{x}) = \nabla f|_{\mathbf{P}} = \mathbf{A}\mathbf{x} - \mathbf{b}$. At this point, given an initial guess $\mathbf{x}_0$, which can be obtained by brute force evaluating the function with a certain coarse sampling, the conjugate constraint (seen in (E.12)) can be applied. Recall that a triumph for that direction is that N line minimizations will put it exactly at the minimum of a quadratic form-like. Following with the development, recall that we want to proceed not along the gradient, but in a direction to be conjugate to the old gradient, and, insofar as possible, to all previous directions traversed. The application of the final implementation of the CGM algorithm seen in the previous Section for the minimization of non-linear functions is detailed hereinafter.

Starting with an arbitrary initial guess vector $\mathbf{r}_0$ and generating two arbitrary equal vectors $\mathbf{p}_0 = \mathbf{r}_0$, the CGM constructs two recursive sequences of vectors as follows

$$\begin{aligned} \mathbf{r}_{k+1} &= \mathbf{r}_k - \alpha_k \mathbf{A}\mathbf{p}_k \\ \mathbf{p}_{k+1} &= \mathbf{r}_{k+1} + \beta_k \mathbf{p}_k \end{aligned} \tag{E.19}$$

where α and β are chosen to a series of vectors $\mathbf{r}$ satisfying orthogonality condition, and a series of vectors $\mathbf{p}$ to be conjugate among them

$$\begin{aligned} \mathbf{g}_{n+1}^T \mathbf{g}_n &= 0 \\ \mathbf{h}_{n+1}^T \mathbf{A}\mathbf{h}_n &= 0 \end{aligned} \tag{E.20}$$

leading to the expressions seen in the last part of the previous Section

$$\begin{aligned} \alpha_k &= \frac{\mathbf{r}_k^T \mathbf{r}_k}{\mathbf{p}_k^T \mathbf{A}\mathbf{p}_k} \\ \beta_k &= \frac{\mathbf{r}_{k+1}^T \mathbf{r}_{k+1}}{\mathbf{r}_k^T \mathbf{r}_k} \end{aligned} \tag{E.21}$$

The expression of β_k seen in (E.21) corresponds to the one proposed by Fletcher-Reeves. In complex practical tests, it has been shown that it leads to a significant slow down of the convergence of the algorithm. For this reason, the CPT minimization is based on the use of Polak-Ribière implementation, which is more efficient

$$\beta_k = \frac{(\mathbf{r}_{k+1} - \mathbf{r}_k)^T \mathbf{r}_{k+1}}{\mathbf{r}_k^T \mathbf{r}_k} \tag{E.22}$$

E.3 CGM Integration in CPT

The CGM integration method employed in the CPT is based on modifying matrix $\mathbf{A}$ in (E.2), in order to apply different weights to each link depending on their quality. These weights directly derive from the calculated values of model coherence. If m accounts for the number of relationships and n the number of PSCs, the linear system equation system is now reformulated as follows

$$\mathbf{W}\mathbf{A}\mathbf{x} = \mathbf{W}\Delta\mathbf{y} \tag{E.23}$$

where $\mathbf{W}$ is a $m \times m$ diagonal matrix containing the weight of each arc, which allows to reduce the impact of low quality links during the integration, $\mathbf{A}$ is a $m \times n$ matrix defining the relationships, $\mathbf{x}$ is a vector of n elements with the unknowns representing either the absolute of linear velocity or topographic error, and $\Delta\mathbf{y}$ is a vector of m elements containing the linear parameter increments of the relationships $\{\Delta v, \Delta\varepsilon\}$.

If the following matrices are defined

$$\begin{aligned} \mathbf{C} &= \mathbf{WA} \\ \Delta\mathbf{y}' &= \mathbf{W}\Delta\mathbf{y} \end{aligned} \tag{E.24}$$

where $\mathbf{C}$ is now a $m \times n$ matrix containing the weighted relationships and $\Delta\mathbf{y}'$ is a $m \times 1$ matrix containing the weighted increments of the relationships, the system equations may be rewritten as follows

$$\mathbf{Cx} = \Delta\mathbf{y}', \tag{E.25}$$

which is totally equivalent to the one seen in (E.2).

Notice that this is an over-determined systems of linear equations, therefore, the theory seen in Section E.1 should be slightly modified as proposed by Mallorquí in [213] and applied by Blanco-Sánchez during this PhD work [214].

As seen in the formulation given in Section E.1, the starting point is an initial unknown vector $\mathbf{x}_0$ and, from this point, $\mathbf{x}_k$ is updated displacing towards the conjugate directions $\mathbf{p}_k$ weighted by the constant coefficient α_k, which indicates how it moves in that direction, as follows $\mathbf{x}_{k+1} = \mathbf{x}_k - \alpha_k\mathbf{p}_k$.

The key step of the algorithm is to choose α_k in order to minimize the error E_k between the observations and unknowns in the $k-th$ estimation

$$E_k = \|\mathbf{Cx}_k - \Delta\mathbf{y}'\|^2 \tag{E.26}$$

where the coefficient α_k which minimizes this error may be expressed as follows

$$\alpha_{k+1} = \frac{\mathbf{r}_k^T\mathbf{Cp}_{k+1}}{\|\mathbf{C}\cdot\mathbf{p}_{k+1}\|^2} \tag{E.27}$$

In that expression $\mathbf{r}_k$ refers to as the $k-th$ residual vector, which now may be defined as

$$\mathbf{r}_k = \mathbf{Cx}_k - \Delta\mathbf{y}' \tag{E.28}$$

The value of the residue is updated recursively

$$\mathbf{r}_{k+1} = \mathbf{r}_k - \alpha_k\mathbf{Cp}_k \tag{E.29}$$

and from this, the conjugate directions $\mathbf{p}_k$ can be calculated departing from

$$\mathbf{p}_0 = \mathbf{r}_0, \tag{E.30}$$

which provides the direction of the gradient at the initial guess $\mathbf{x} = \mathbf{x}_0$. The successive conjugate directions are obtained recursively

$$\mathbf{p}_{k+1} = \beta_k\mathbf{p}_k - \mathbf{C}^T\mathbf{r}_k, \tag{E.31}$$

where

$$\beta_k = \frac{\left\|\mathbf{C}^T\mathbf{r}_k\right\|^2}{\left\|\mathbf{C}^T\mathbf{r}_{k-1}\right\|^2} \tag{E.32}$$

At each iteration the quality of the solution is given by the modulus of the normalized residue as follows

$$N_k = \frac{\|\mathbf{r}_k\|}{\|\Delta\mathbf{y}'\|} = \frac{\|\mathbf{C}\mathbf{x}_k - \Delta\mathbf{y}'\|}{\|\Delta\mathbf{y}'\|} \tag{E.33}$$

and the iterations stop when N_k is considered to converge.

F

Appendix F

Singular Value Descomposition Formalism

The Singular Value Descomposition is based on a factorization of non-square matrices with many useful applications in signal processing and statistics. One of these applications is based on computing matrix pseudoinverse and, hence, it can be used to solve over-determined systems of linear equations [183]. This method has been employed in this PhD Thesis during the NLEB of the CPT, when the interferometric phase residues are translated into they former absolute image phases to derive displacement time-series. This Appendix reviews the mathematical formalism behind the SVD algorithm.

F.1 Algorithm formalism

As stated above, SVD is very useful tool for inverting matrices, and it is based on the decomposition of a non-square matrix as a multiplication of three matrices.

Suppose $\mathbf{A}$ is a $m \times n$ matrix whose entries come from the real numbers. Following this argument, there exists a factorization of the form

$$\mathbf{A} = \mathbf{U} \cdot \Sigma \cdot \mathbf{V}^T = \begin{bmatrix} \mathbf{u}_1 & \dots & \mathbf{u}_m \end{bmatrix}_{m \times m} \cdot \begin{bmatrix} \sigma_1 & & \\ & \ddots & \\ & & \sigma_r \end{bmatrix}_{m \times n} \cdot \begin{bmatrix} \mathbf{v}_1 & \dots & \mathbf{v}_m \end{bmatrix}^T_{n \times n} \quad \text{(F.1)}$$

where:

- $\mathbf{A}$ is a non-square matrix of dimensions $m \times n$.
- $\mathbf{U}$ is a square unitary matrix of dimensions $m \times m$.
- $\mathbf{V}^T$ denotes the transpose of the $n \times n$ unitary matrix $\mathbf{V}$.
- Σ is a matrix of dimensions $m \times n$ with r non-negative real number on the diagonal.

On the one hand, the diagonal entries $(\sigma_1, \sigma_2, \dots, \sigma_r)$ of Σ are known as singular values of $\mathbf{A}$. A common convention is to list the singular values in descending order. In this case, the diagonal matrix Σ is uniquely determined by $\mathbf{A}$. On the other hand, the m columns of $\mathbf{U}$ and the he n columns of $\mathbf{V}$ corresponds to a set of orthonormal vectors, which can be regarded as basis vectors, and are referred to as left-singular and right-singular vectors of $\mathbf{A}$, respectively.

There is a close relationship between the singular value decomposition and the eigen-decomposition:

- The left-singular vectors of $\mathbf{A}$ are eigenvectors of $\mathbf{A}^T\mathbf{A}$.
- The right-singular vectors of $\mathbf{A}$ are eigenvectors of $\mathbf{A}\mathbf{A}^T$.
- The non-zero singular values of $\mathbf{A}$ (found on the diagonal entries of Σ) are the square roots of the non-zero eigenvalues λ of both $\mathbf{A}\mathbf{A}^T$ and $\mathbf{A}^T\mathbf{A}$.

In this context, a non-negative real number σ is a singular value for $\mathbf{A}$ if there exist unit-length vectors $\mathbf{u}$ and $\mathbf{v}$ that fulfills

$$\mathbf{A}\mathbf{v} = \sigma\mathbf{u} \quad \text{(F.2)}$$

$$\mathbf{A}^T\mathbf{u} = \sigma\mathbf{v} \quad \text{(F.3)}$$

In the following Section the way to compute the pseudoinverse of non-square matrix is given.

F.2 Pseudoinverse computation

Applications that employ the SVD include computing the pseudoinverse, least squares fitting, determining the rank of a matrix, etc.

In this PhD Thesis we are interested in computing the pseudoinverse to solve systems of linear equations. In this context, the inversion of $\mathbf{A}$ can be easily calculated as

$$\mathbf{A}^{-1} = \mathbf{V} \cdot \Sigma^{-1} \cdot \mathbf{U}^T \tag{F.4}$$

Notice that the inverse of the orthogonal matrices $\{\mathbf{U}, \mathbf{V}\}$ corresponds to its transpose, whereas the inverse of Σ corresponds to the inverse of its diagonal elements. For this reason, this method is very useful to solve systems of linear equations of the form $\mathbf{Ax} = \mathbf{b}$, in which the solution is based on inverting the matrix $\mathbf{A}$ as seen in (F.4).

Finally, it worth pointing out that there is a problem when solving the system by means the inversion of the matrix of coefficients. When $\mathbf{x}$ belongs to a null space of $\mathbf{A}$, i.e, $\sigma = 0$, the noise is amplified during the inversion of the diagonal elements of Σ. To control this effect the so-called condition number is typically calculated. The condition number corresponds to the ratio C of the largest to smallest singular value in the singular value decomposition of a matrix. This condition number highlights how the noise is amplified in each one of the parameters. If the condition number is high, small noise perturbations on the data will produce large oscillations of the solution. To avoid the amplification of the noise the problem can be truncated with a consequent rank reduction.

G

Appendix G

Complete List of Interferograms

G.1 TerraSAR-X data set

Interferogram Number	**Master Date** dd/mm/yyyy	**Slave Date** dd/mm/yyyy	**Perpendicular Baseline** meters	**Temporal Baseline** days
1	18/11/2010	11/29/2010	-76.3605	11
2	18/11/2010	02/14/2011	74.2942	88
3	18/11/2010	04/21/2011	124.919	154
4	18/11/2010	05/02/2011	-27.5895	165
5	18/11/2010	05/13/2011	16.4280	176
6	18/11/2010	05/24/2011	35.9565	187
7	18/11/2010	06/15/2011	-112.516	209
8	18/11/2010	06/26/2011	29.6292	220
9	18/11/2010	07/07/2011	-38.0220	231
10	18/11/2010	07/18/2011	77.3766	242
11	18/11/2010	07/29/2011	31.8389	253
12	18/11/2010	08/09/2011	33.4652	264
13	18/11/2010	08/20/2011	12.9409	275
14	18/11/2010	08/31/2011	-18.1361	286
15	18/11/2010	09/22/2011	210.970	308
16	18/11/2010	10/03/2011	121.266	319
17	18/11/2010	10/14/2011	-55.5011	330
18	18/11/2010	10/25/2011	45.1707	341
19	18/11/2010	11/05/2011	-51.7316	352
20	18/11/2010	11/16/2011	53.9789	363
21	29/11/2010	02/14/2011	150.210	77
22	29/11/2010	04/21/2011	201.207	143
23	29/11/2010	05/02/2011	52.9172	154
24	29/11/2010	05/13/2011	92.1513	165
25	29/11/2010	05/24/2011	111.863	176
26	29/11/2010	06/15/2011	-38.1672	198
27	29/11/2010	06/26/2011	105.935	209
28	29/11/2010	07/07/2011	39.2576	220
29	29/11/2010	07/18/2011	153.575	231
30	29/11/2010	07/29/2011	107.009	242
31	29/11/2010	08/09/2011	109.826	253
32	29/11/2010	08/20/2011	88.7808	264
33	29/11/2010	08/31/2011	58.5020	275

Interferogram Number	**Master Date**	**Slave Date**	**Perpendicular Baseline**	**Temporal Baseline**
	dd/mm/yyyy	dd/mm/yyyy	meters	days
34	29/11/2010	09/22/2011	287.010	297
35	29/11/2010	10/03/2011	197.052	308
36	29/11/2010	10/14/2011	20.9489	319
37	29/11/2010	10/25/2011	121.530	330
38	29/11/2010	11/05/2011	24.6969	341
39	29/11/2010	11/16/2011	130.344	352
40	14/02/2011	04/21/2011	51.4477	66
41	14/02/2011	05/02/2011	-101.007	77
42	14/02/2011	05/13/2011	-58.1178	88
43	14/02/2011	05/24/2011	-38.3844	99
44	14/02/2011	06/15/2011	-186.780	121
45	14/02/2011	06/26/2011	-44.8129	132
46	14/02/2011	07/07/2011	-111.087	143
47	14/02/2011	07/18/2011	5.54209	154
48	14/02/2011	07/29/2011	-43.2615	165
49	14/02/2011	08/09/2011	-41.8994	176
50	14/02/2011	08/20/2011	-61.5389	187
51	14/02/2011	08/31/2011	-92.4241	198
52	14/02/2011	09/22/2011	136.794	220
53	14/02/2011	10/03/2011	46.9678	231
54	14/02/2011	10/14/2011	-129.536	242
55	14/02/2011	10/25/2011	-30.2347	253
56	14/02/2011	11/05/2011	-125.774	264
57	14/02/2011	11/16/2011	-22.7424	275
58	21/04/2011	05/02/2011	-150.789	11
59	21/04/2011	05/13/2011	-109.074	22
60	21/04/2011	05/24/2011	-89.4000	33
61	21/04/2011	06/15/2011	-237.250	55
62	21/04/2011	06/26/2011	-95.2919	66
63	21/04/2011	07/07/2011	-162.240	77
64	21/04/2011	07/18/2011	-47.6606	88
65	21/04/2011	07/29/2011	-94.5700	99
66	21/04/2011	08/09/2011	-91.6541	110
67	21/04/2011	08/20/2011	-112.420	121
68	21/04/2011	08/31/2011	-142.973	132
69	21/04/2011	09/22/2011	86.4163	154

Interferogram Number	**Master Date**	**Slave Date**	**Perpendicular Baseline**	**Temporal Baseline**
	dd/mm/yyyy	dd/mm/yyyy	meters	days
70	21/04/2011	10/03/2011	-12.6566	165
71	21/04/2011	10/14/2011	-180.386	176
72	21/04/2011	10/25/2011	-79.8035	187
73	21/04/2011	11/05/2011	-176.619	198
74	21/04/2011	11/16/2011	-71.1376	209
75	02/05/2011	05/13/2011	43.9166	11
76	02/05/2011	05/24/2011	63.0308	22
77	02/05/2011	06/15/2011	-86.7548	44
78	02/05/2011	06/26/2011	56.2296	55
79	02/05/2011	07/07/2011	-22.0042	66
80	02/05/2011	07/18/2011	103.684	77
81	02/05/2011	07/29/2011	59.3147	88
82	02/05/2011	08/09/2011	59.2943	99
83	02/05/2011	08/20/2011	40.4435	110
84	02/05/2011	08/31/2011	11.5582	121
85	02/05/2011	09/22/2011	237.149	143
86	02/05/2011	10/03/2011	147.903	154
87	02/05/2011	10/14/2011	-32.3573	165
88	02/05/2011	10/25/2011	71.1369	176
89	02/05/2011	11/05/2011	-28.8751	187
90	02/05/2011	11/16/2011	79.6717	198
91	13/05/2011	05/24/2011	19.7327	11
92	13/05/2011	06/15/2011	-128.712	33
93	13/05/2011	06/26/2011	14.1558	44
94	13/05/2011	07/07/2011	-53.2068	55
95	13/05/2011	07/18/2011	61.4286	66
96	13/05/2011	07/29/2011	15.4165	77
97	13/05/2011	08/09/2011	18.8260	88
98	13/05/2011	08/20/2011	-3.48677	99
99	13/05/2011	08/31/2011	-34.4552	110
100	13/05/2011	09/22/2011	194.899	132
101	13/05/2011	10/03/2011	105.054	143
102	13/05/2011	10/14/2011	-71.4296	154
103	13/05/2011	10/25/2011	29.8422	165
104	13/05/2011	11/05/2011	-67.6648	176
105	13/05/2011	11/16/2011	38.7063	187

Interferogram Number	**Master Date** dd/mm/yyyy	**Slave Date** dd/mm/yyyy	**Perpendicular Baseline** meters	**Temporal Baseline** days
106	24/05/2011	06/15/2011	-148.414	22
107	24/05/2011	06/26/2011	-7.37334	33
108	24/05/2011	07/07/2011	-72.8444	44
109	24/05/2011	07/18/2011	41.7463	55
110	24/05/2011	07/29/2011	-6.09834	66
111	24/05/2011	08/09/2011	-8.24853	77
112	24/05/2011	08/20/2011	-23.1532	88
113	24/05/2011	08/31/2011	-54.0814	99
114	24/05/2011	09/22/2011	175.164	121
115	24/05/2011	10/03/2011	85.3366	132
116	24/05/2011	10/14/2011	-91.1614	143
117	24/05/2011	10/25/2011	11.7035	154
118	24/05/2011	11/05/2011	-87.3973	165
119	24/05/2011	11/16/2011	20.0578	176
120	15/06/2011	06/26/2011	142.137	11
121	15/06/2011	07/07/2011	76.8456	22
122	15/06/2011	07/18/2011	189.888	33
123	15/06/2011	07/29/2011	143.904	44
124	15/06/2011	08/09/2011	145.660	55
125	15/06/2011	08/20/2011	125.297	66
126	15/06/2011	08/31/2011	94.4004	77
127	15/06/2011	09/22/2011	323.500	99
128	15/06/2011	10/03/2011	233.794	110
129	15/06/2011	10/14/2011	57.6003	121
130	15/06/2011	10/25/2011	157.478	132
131	15/06/2011	11/05/2011	61.3114	143
132	15/06/2011	11/16/2011	166.166	154
133	26/06/2011	07/07/2011	-67.1903	11
134	26/06/2011	07/18/2011	47.7539	22
135	26/06/2011	07/29/2011	7.94036	33
136	26/06/2011	08/09/2011	5.19177	44
137	26/06/2011	08/20/2011	-17.2928	55
138	26/06/2011	08/31/2011	-47.7318	66
139	26/06/2011	09/22/2011	181.356	88
140	26/06/2011	10/03/2011	91.7624	99

Interferogram Number	**Master Date** dd/mm/yyyy	**Slave Date** dd/mm/yyyy	**Perpendicular Baseline** meters	**Temporal Baseline** days
141	26/06/2011	10/14/2011	-85.1047	110
142	26/06/2011	10/25/2011	15.7164	121
143	26/06/2011	11/05/2011	-81.3354	132
144	26/06/2011	11/16/2011	24.5834	143
145	07/07/2011	07/18/2011	114.598	11
146	07/07/2011	07/29/2011	67.8466	22.
147	07/07/2011	08/09/2011	71.3568	33
148	07/07/2011	08/20/2011	49.9226	44
149	07/07/2011	08/31/2011	21.4653	55
150	07/07/2011	09/22/2011	247.862	77
151	07/07/2011	10/03/2011	157.860	88
152	07/07/2011	10/14/2011	-19.4526	99
153	07/07/2011	10/25/2011	82.8892	110
154	07/07/2011	11/05/2011	-15.9719	121
155	07/07/2011	11/16/2011	91.7499	132
156	18/07/2011	07/29/2011	-46.9636	11
157	18/07/2011	08/09/2011	-44.3930	22
158	18/07/2011	08/20/2011	-64.7919	33
159	18/07/2011	08/31/2011	-95.4811	44
160	18/07/2011	09/22/2011	133.602	66
161	18/07/2011	10/03/2011	44.3197	77
162	18/07/2011	10/14/2011	-132.801	88
163	18/07/2011	10/25/2011	-32.5420	99
164	18/07/2011	11/05/2011	-129.034	110
165	18/07/2011	11/16/2011	-24.2845	121
166	29/07/2011	08/09/2011	11.8047	11
167	29/07/2011	08/20/2011	-18.9020	22
168	29/07/2011	08/31/2011	-49.7974	33
169	29/07/2011	09/22/2011	180.011	55
170	29/07/2011	10/03/2011	90.0315	66
171	29/07/2011	10/14/2011	-86.4449	77
172	29/07/2011	10/25/2011	17.8012	88
173	29/07/2011	11/05/2011	-82.6929	99
174	29/07/2011	11/16/2011	26.0622	110
175	09/08/2011	08/20/2011	-21.7186	11

Interferogram Number	**Master Date** dd/mm/yyyy	**Slave Date** dd/mm/yyyy	**Perpendicular Baseline** meters	**Temporal Baseline** days
176	09/08/2011	08/31/2011	-51.3950	22
177	09/08/2011	09/22/2011	177.907	44
178	09/08/2011	10/03/2011	88.6444	55
179	09/08/2011	10/14/2011	-88.9208	66
180	09/08/2011	10/25/2011	11.8577	77
181	09/08/2011	11/05/2011	-85.1544	88
182	09/08/2011	11/16/2011	20.5492	99
183	20/08/2011	08/31/2011	-30.9821	11
184	20/08/2011	09/22/2011	198.305	33
185	20/08/2011	10/03/2011	108.490	44
186	20/08/2011	10/14/2011	-68.0292	55
187	20/08/2011	10/25/2011	33.0072	66
188	20/08/2011	11/05/2011	-64.2624	77
189	20/08/2011	11/16/2011	41.8746	88
190	31/08/2011	09/22/2011	229.093	22
191	31/08/2011	10/03/2011	139.404	33
192	31/08/2011	10/14/2011	-37.5678	44
193	31/08/2011	10/25/2011	63.1842	55
194	31/08/2011	11/05/2011	-33.8090	66
195	31/08/2011	11/16/2011	71.9452	77
196	22/09/2011	10/03/2011	-90.0520	11
197	22/09/2011	10/14/2011	-266.298	22
198	22/09/2011	10/25/2011	-166.020	33
199	22/09/2011	11/05/2011	-262.538	44
200	22/09/2011	11/16/2011	-157.448	55
201	03/10/2011	10/14/2011	-176.430	11
202	03/10/2011	10/25/2011	-76.8156	22
203	03/10/2011	11/05/2011	-172.673	33
204	03/10/2011	11/16/2011	-68.5794	44
205	14/10/2011	10/25/2011	100.668	11
206	14/10/2011	11/05/2011	3.77130	22
207	14/10/2011	11/16/2011	109.465	33
208	25/10/2011	11/05/2011	-96.9023	11
209	25/10/2011	11/16/2011	8.86653	22
210	05/11/2011	11/16/2011	105.695	11

G.2 GB-SAR data set

Interferogram Number	**Master Date** dd/mm/yyyy	**Slave Date** dd/mm/yyyy	**Perpendicular Baseline** meters	**Temporal Baseline** days
1	21/10/2010	18/11/2010	0	28
2	21/10/2010	09/02/2011	0	111
3	21/10/2010	07/04/2011	0	168
4	21/10/2010	06/05/2011	0	197
5	21/10/2010	25/05/2011	0	216
6	21/10/2010	09/06/2011	0	231
7	21/10/2010	05/07/2011	0	257
8	21/10/2010	06/09/2011	0	320
9	21/10/2010	05/10/2011	0	349
10	18/11/2010	09/02/2011	0	83
11	18/11/2010	07/04/2011	0	140
12	18/11/2010	06/05/2011	0	169
13	18/11/2010	25/05/2011	0	188
14	18/11/2010	09/06/2011	0	203
15	18/11/2010	05/07/2011	0	229
16	18/11/2010	06/09/2011	0	292
17	18/11/2010	05/10/2011	0	321
18	09/02/2011	07/04/2011	0	57
19	09/02/2011	06/05/2011	0	86
20	09/02/2011	25/05/2011	0	105
21	09/02/2011	09/06/2011	0	120
22	09/02/2011	05/07/2011	0	146
23	09/02/2011	06/09/2011	0	209
24	09/02/2011	05/10/2011	0	238
25	07/04/2011	06/05/2011	0	29
26	07/04/2011	25/05/2011	0	48
27	07/04/2011	09/06/2011	0	63
28	07/04/2011	05/07/2011	0	89
29	07/04/2011	06/09/2011	0	152
30	07/04/2011	05/10/2011	0	181
31	06/05/2011	25/05/2011	0	19
32	06/05/2011	09/06/2011	0	34
33	06/05/2011	05/07/2011	0	60

Interferogram Number	**Master Date**	**Slave Date**	**Perpendicular Baseline**	**Temporal Baseline**
	dd/mm/yyyy	dd/mm/yyyy	meters	days
34	06/05/2011	06/09/2011	0	123
35	06/05/2011	05/10/2011	0	152
36	25/05/2011	09/06/2011	0	15
37	25/05/2011	05/07/2011	0	41
38	25/05/2011	06/09/2011	0	104
39	25/05/2011	05/10/2011	0	133
40	09/06/2011	05/07/2011	0	26
41	09/06/2011	06/09/2011	0	89
42	09/06/2011	05/10/2011	0	118
43	05/07/2011	06/09/2011	0	63
44	05/07/2011	05/10/2011	0	92
45	06/09/2011	05/10/2011	0	29

List of Acronyms

ACR Artificial Corner Reflector
ALOS Advanced Land Operating Satellite
ASF Alaska Satellite Facility
AOI area of interest
APS Atmospheric Phase Screen
ASAR Advanced Synthetic Aperture Radar
ASI Italian Space Agency
BPT Binary Partition Tree
Caltech California Institute of Technology
CCRS Canada Center for Remote Sensing
CGM Conjugate Gradient Method
CNES Centre National d'Études Spatiales
COTS commercially available off-the-shelf
CPT Coherent Pixels Technique
CS Coherent Scatterer
CSA Canadian Space Agency
D_A Amplitude Dispersion
DCRS Danish Center for Remote Sensing
DDS Digital Direct Synthesizer
DEM Digital Elevation Model
DGPS Differential Ground Positioning System
DLR German Aerospace Center
DORIS Delft Object-Oriented Radar Interferometric Software
DSM Digital Surface Model
EC European Commission
ECEF Earth Centered Earth Fixed

ECMWF European Center for Medium-Range Weather Forecast

ENVISAT Environmental Satellite

ERA-I ERA Interim

ERS European Remote Sensing Satellite

ESM Equal Scattering Mechanism

ESA European Space Agency

EWS Early Warning Systems

DInSAR Differential SAR Interferometry

FastGBSAR Fast Ground-Based Synthetic Aperture Radar

FM Frequency Modulation

FMCW Frequency Modulated Continuous Wave

FPLB Final Product Layout Block

GAM Global Atmospheric Models

GAR Global Assessment Report

GB-SAR Ground-Based SAR

GB-InSAR Ground-Based SAR Interferometry

GCP Ground Control Point

GIS Geographic Information System

GPS Global Positioning System

GMES Global Monitoring for Environment and Security

IDS Ingegneria Dei Sistemi

IF intermediate frequency

InSAR SAR Interferometry

ITU International Telecommunication Union

JAXA National Space Development Agency of Japan

JPL Jet Propulsion Laboratories

JRC Joint Research Center

MAF Model Adjustment Function

MCF Minimum Cost Flow

MDA MacDonald Dettwiler and Associates

MERIS Medium-Resolution Imaging Spectrometer

ML multi-look

MLRM Multiple Linear Regression Model

MM5 fifth-generation Penn State/NCAR mesoscale model

MODIS Moderate-Resolution Imaging Spectroradiometer

NASA National Aeronautics and Space Administration

NEST Next ESA SAR Toolbox

NGA National Geospatial-Intelligence Agency

NGI Norwegian Geotechnical Institute

NLEB Non-Linear Estimation Block

NL-InSAR Non-Local Interferometric SAR

NOAA National Oceanic and Atmospheric Administration

LEB Linear Estimation Block

LFM linear frequency modulation

LiSA Linear SAR

LOS line-of-sight

LTP Long-Term Processing

ONERA Office National d'Etudes et de Recherches Aérospatiales

PALSAR Phased Array L-band Synthetic Aperture Radar

PNOTS Spanish National Earth Observation Program

PDF Probability Density Function

PolDInSAR Polarimetric Differential SAR Interferometry

PolInSAR Polarimetric SAR Interferometry

PolSAR Polarimetric SAR

PRF Pulse Repetition Frequency

PRISAR PRecise Interferometric SAR

PS Permanent Scatterer

PSC Persistent Scatterer Candidate

PSF Point Spread Funtion

PSI Persistent Scatterer Interferometry

RAR Real Aperture Radar

RCS Radar Cross Section

RF radio frequency

RG Region Growing

RMSE Root Mean Square Error

ROIPAC Repeat Orbit Interferometry Package

RSLab Remote Sensing Laboratory

SAR Synthetic Aperture Radar

SCS Stable Coherent Scatterer

SFCW Steepest Frequency Continuous Wave

SHR Spatial High Resolution

SIR Spaceborne Imaging Radar

SIR-C/X-SAR Spaceborne Imaging Radar-C/X-Band Synthetic Aperture Radar

SLAR Side-Looking Aperture Radar

SLC Single Look Complex

SLFM-CW Stepped Linear Frequency Modulated Continuous Wave

SLR Spatial Low Resolution

SLRM Side Lobe Risk Map

SNR signal-to-noise ratio

SOM Sub-Optimum Scattering Mechanism

SRTM Shuttle Radar Topography Mission

STFFT short-time fast Fourier transform

STP Short-Term Processing

SubSoft Subsidence Software

SVD Singular Value Decomposition

SVA Spatially Variant Apodization

TanDEM-X TerraSAR-X add-on for Digital Elevation Measurement

TEC Total Electron Content

TOPS Terrain Observation by Progressive Scans

TSC Temporal Sublook Coherence

TSE Temporal Sublook Entropy

TSSC Temporal Sublook Spectral Correlation

UPC Universitat Politècnica de Catalunya

UTM Universal Transverse Mercator

VNA Vector Network Analyzer

WMLE Weighted Maximum Likelihood Estimator

WMLS Weighted Mean Least Squares

ZTD Zenith Total Delay

Bibliography

[1] F. Nadim, O. Kjekstad, P. Peduzzi, C. Herold, and C. Jaedicke, "Global landslide and avalanche hotspots," *Landslides*, vol. 3, no. 2, pp. 159–173, Feb. 2006. (Cited on page 3.)

[2] D. J. Varnes, "Slope movement types and processes," in *Landslide analysis and control*, ser. Transportation Research Board Special Report, R. Schuster and R. Krizek, Eds. National Academy of Sciences, Special Report 176, 1978, pp. 11–33. (Cited on pages 4, 255, and 256.)

[3] D. M. Cruden and D. J. Varnes, "Landslide types and processes," in *Landslide investigation and mitigation*, ser. Transportation Research Board Special Report, A. K. Turner and R. L. Schuster, Eds. National Academy of Sciences, Special Report 247, 1996, pp. 36–71. (Cited on pages 5, 257, 258, and 259.)

[4] A. Ferrero, G. Forlani, and I. Voyat, "Rock slope stability analysis based on photogrammetric surveys," in *Proc. IX International Symposium on Landslides*, Río de Janeiro (Brazil), Jun. 2004. (Cited on page 6.)

[5] J. P. Mills, S. J. Buckley, H. L. Mitchell, P. J. Clarke, and S. J. Edwards, "A geomatics data integration technique for coastal change monitoring," *Earth Surface Processes and Landforms*, vol. 30, no. 6, pp. 651–664, Jun. 2005. (Cited on page 6.)

[6] X. W. Hu, H. M. Tang, and J. S. Li, "General digital camera-based experiments for large-scale landslide physical model measurement," in *Proc. 10th International Symposium on Landslides and Engineered Slopes*, Xian (China), Jun. 2008. (Cited on page 6.)

[7] S. Liu and Z. Wang, "Choice of surveying methods for landslides monitoring," in *Proc. 10th International Symposium on Landslides and Engineered Slopes*, Xian (China), Jun. 2008. (Cited on page 6.)

[8] M. J. Smith, J. Chandler, and J. Rose, "High spatial resolution data acquisition for the geosciences: kite aerial photography," *Earth Surface Processes and Landforms*, vol. 34, no. 1, pp. 155–161, Jan. 2009. (Cited on page 6.)

[9] J. A. Gili, J. Corominas, and J. Rius, "Using Global Positioning System techniques in landslide monitoring," *Engineering Geology*, vol. 55, no. 3, pp. 167–192, Feb. 2000. (Cited on page 8.)

[10] P. D. Savvaidis, "Existing landslide monitoring systems and techniques," *From Stars to Earth and Culture*, vol. 34, no. 1, pp. 242–258, Jan. 2003. (Cited on pages 8 and 10.)

[11] J. Corominas, J. Moya, A. Lloret, J. A. Gili, M. G. Angeli, A. Pasuto, and S. Silvano, "Measurement of landslide displacements using a wire extensometer," *Engineering Geology*, vol. 55, no. 3, pp. 149–166, Feb. 2000. (Cited on page 9.)

[12] C. A. Wiley, "Pulsed Doppler Radar Method and Means," USA Patent, 1954. (Cited on page 11.)

[13] L. J. Cutrona, E. N. Leith, C. J. Palermo, and L. J. Porcello, "Optical data processing and filtering systems," *IEEE Transactions on Information Theory*, vol. 6, no. 3, pp. 386–400, Jun. 1960. (Cited on page 11.)

[14] L. C. Graham, "Synthetic interferometer radar for topographic mapping," *Proceedings of the IEEE*, vol. 62, no. 6, pp. 763–768, Jun. 1974. (Cited on page 11.)

[15] H. A. Zebker and R. M. Goldstein, "Topographic mapping from interferometric synthetic aperture radar observations," *Journal of Geophysical Research: Solid Earth*, vol. 91, no. B5, pp. 4993–4999, Apr. 1986. (Cited on pages 11 and 52.)

[16] D. Massonnet, M. Rossi, C. Carmona, F. Adragna, G. Peltzer, K. Feigl, and T. Rabaute, "The displacement field of the Landers earthquake mapped by radar interferometry," *Nature*, vol. 364, no. 6433, pp. 138–142, Jul. 1993. (Cited on page 12.)

[17] R. M. Goldstein, H. Engelhardt, B. Kamb, and R. M. Frolich, "Satellite radar interferometry for monitoring ice sheet motion: application to an antarctic ice stream," *Science*, vol. 262, no. 5139, pp. 1525–1530, Dec. 1993. (Cited on page 12.)

[18] A. Ferretti, C. Prati, and F. Rocca, "Nonlinear subsidence rate estimation using permanent scatterers in differential SAR interferometry," *IEEE Transactions on Geoscience and Remote Sensing*, vol. 38, no. 5, pp. 2202–2212, Sep. 2000. (Cited on pages 12, 72, and 82.)

[19] ——, "Permanent Scatterers in SAR interferometry," *IEEE Transactions on Geoscience and Remote Sensing*, vol. 39, no. 1, pp. 8–20, Jan. 2001. (Cited on pages 12, 33, 82, 89, 90, 183, 184, 185, and 274.)

[20] O. Mora, J. J. Mallorqui, and J. Duro, "Generation of deformation maps at low resolution using differential interferometric SAR data," in *Proc. IEEE International Geoscience and Remote Sensing Symposium (IGARSS'02)*, Toronto (Canda), Jun. 2002. (Cited on pages 12 and 82.)

[21] P. Berardino, G. Fornaro, R. Lanari, and E. Sansosti, "A new algorithm for surface deformation monitoring based on small baseline differential SAR interferograms," *IEEE Transactions on Geoscience and Remote Sensing*, vol. 40, no. 11, pp. 2375–2383, Nov. 2002. (Cited on pages 12, 72, and 82.)

[22] O. Mora, J. J. Mallorqui, and A. Broquetas, "Linear and nonlinear terrain deformation maps from a reduced set of interferometric SAR images," *IEEE Transactions on Geoscience and Remote Sensing*, vol. 41, no. 10, pp. 2243–2253, Oct. 2003. (Cited on pages 12, 33, 72, 82, 99, 102, 109, and 183.)

[23] C. Werner, U. Wegmuller, T. Strozzi, and A. Wiesmann, "Interferometric point target analysis for deformation mapping," in *Proc. IEEE International Geoscience and Remote Sensing Symposium (IGARSS'03)*, Toulouse (France), Jul. 2003. (Cited on pages 12 and 82.)

[24] A. Arnaud, N. Adam, R. Hanssen, J. Inglada, J. Duro, J. Closa, and M. Eineder, "ASAR ERS interferometric phase continuity," in *Proc. IEEE International Geoscience and Remote Sensing Symposium (IGARSS'03)*, Toulouse (France), Jul. 2003. (Cited on pages 12 and 82.)

[25] A. Hooper, "A new method for measuring deformation on volcanoes and other natural terrains using InSAR persistent scatterers," *Geophysical Research Letters*, vol. 31, no. 23, pp. 23 611–23 616, Dec. 2004. (Cited on pages 12 and 82.)

[26] R. Lanari, O. Mora, M. Manunta, J. J. Mallorqui, P. Berardino, and E. Sansosti, "A small-baseline approach for investigating deformations on full-resolution differential SAR interferograms," *IEEE Transactions on Geoscience and Remote Sensing*, vol. 42, no. 7, pp. 1377–1386, Jul. 2004. (Cited on pages 12, 33, 82, and 183.)

[27] A. Hooper, "A multi-temporal InSAR method incorporating both persistent scatterer and small baseline approaches," *Geophysical Research Letters*, vol. 35, no. 16, pp. 16 302–16 307, Aug. 2008. (Cited on pages 12 and 82.)

[28] G. Fornaro, D. Reale, and F. Serafino, "Four-Dimensional SAR Imaging for Height Estimation and Monitoring of Single and Double Scatterers," *IEEE Transactions on Geoscience and Remote Sensing*, vol. 47, no. 1, pp. 224–237, Jan. 2009. (Cited on pages 12 and 82.)

[29] M. Crosetto, O. Montserrat, R. Iglesias, and B. Crippa, "Persistent Scatterer Interferometry: Potential, Limits and Initial C- and X-band Comparison," *Photogrammetric engineering and remote sensing*, vol. 76, no. 9, pp. 1061–1069, Sep. 2010. (Cited on pages 12 and 82.)

[30] A. Ferretti, A. Fumagalli, F. Novali, C. Prati, F. Rocca, and A. Rucci, "A New Algorithm for Processing Interferometric Data-Stacks: SqueeSAR," *IEEE Transactions on Geoscience and Remote Sensing*, vol. 49, no. 9, pp. 3460–3470, Sep. 2011. (Cited on pages 12, 82, 251, and 252.)

[31] D. Massonnet, P. Briole, and A. Arnaud, "Deflation of Mount Etna monitored by spaceborne radar interferometry," *Nature*, vol. 375, no. 6532, pp. 567–570, Jun. 1995. (Cited on page 12.)

[32] P. Lundgren, S. Usai, E. Sansosti, R. Lanari, M. Tesauro, G. Fornaro, and P. Berardino, "Modeling surface deformation observed with synthetic aperture radar interferometry at Campi Flegrei caldera," *Journal of Geophysical Research*, vol. 106, no. B9, pp. 19 355–19 366, Sep. 2001. (Cited on page 12.)

[33] R. Kwok and M. A. Fahnestock, "Ice sheet motion and topography from radar interferometry," *IEEE Transactions on Geoscience and Remote Sensing*, vol. 34, no. 1, pp. 189–200, Jan. 1996. (Cited on page 12.)

[34] A. Refice, F. Bovenga, L. Guerriero, and J. Wasowski, "DInSAR applications to landslide studies," in *Proc. IEEE International Geoscience and Remote Sensing Symposium (IGARSS'01)*, Sidney (Australia), Jul. 2001. (Cited on page 12.)

[35] S. Kim and J. Won, "Measurements of soil compaction rate by using JERS-1 SAR and a prediction model," *IEEE Transactions on Geoscience and Remote Sensing*, vol. 41, no. 11, pp. 2683–2686, Nov. 2003. (Cited on page 12.)

[36] R. Hanssen, *Radar interferometry: data interpretation and error analysis*. Kluwer,

2001. (Cited on pages 12, 22, 39, 47, 50, 51, 61, 62, 66, 70, 85, and 109.)

[37] D. Di Martire, R. Iglesias, D. Monells, G. Centolanza, S. Sica, M. Ramondini, L. Pagano, J. J. Mallorqui, and D. Calcaterra, "Comparison between Differential SAR interferometry and ground measurements data in the displacement monitoring of the earth-dam of Conza della Campania (Italy)," *Remote Sensing of Environment*, vol. 148, pp. 58–69, May 2014. (Cited on page 12.)

[38] S. R. Cloude and K. P. Papathanassiou, "Polarimetric SAR interferometry," *IEEE Transactions on Geoscience and Remote Sensing*, vol. 36, no. 5, pp. 1551–1565, Sep. 1998. (Cited on pages 13, 78, and 79.)

[39] ——, "Single-baseline polarimetric SAR interferometry," *IEEE Transactions on Geoscience and Remote Sensing*, vol. 39, no. 11, pp. 2352–2363, Nov. 2001. (Cited on page 13.)

[40] S. Guillaso, L. Ferro-Famil, A. Reigber, and E. Pottier, "Building Characterization Using L-Band Polarimetric Interferometric SAR Data," *IEEE Geoscience and Remote Sensing Letters*, vol. 2, no. 3, pp. 347–351, Jul. 2005. (Cited on page 13.)

[41] T. Mette, I. Hajnsek, and K. P. Papathanassiou, "Height-biomass allometry in temperate forests performance accuracy of height-biomass allometry," in *Proc. IEEE International Geoscience and Remote Sensing Symposium (IGARSS'03)*, Toulouse (France), Jul. 2003. (Cited on page 13.)

[42] M. Lavalle, D. Solimini, E. Pottier, and Y. Desnos, "PolInSAR for Forest Biomass Retrieval: PALSAR Observations and Model Analysis," in *Proc. IEEE International Geoscience and Remote Sensing Symposium (IGARSS'07)*, Barcelona (Spain), Jul. 2007. (Cited on page 13.)

[43] T. Landes, M. Gay, E. Trouvé, J. Nicolas, L. Bombrun, G. Vasile, and I. Hajnsek, "Monitoring temperate glaciers by high resolution Pol-InSAR data: First analysis of Argentière E-SAR acquisitions and in-situ measurements," in *Proc. IEEE International Geoscience and Remote Sensing Symposium (IGARSS'08)*, Boston (Massachusetts, USA), Jul. 2007. (Cited on page 13.)

[44] H. A. Zebker, S. N. Madsen, J. Martin, K. B. Wheeler, T. Miller, Y. Lou, G. Alberti, S. Vetrella, and A. Cucci, "The TOPSAR interferometric radar topographic mapping instrument," *IEEE Transactions on Geoscience and Remote Sensing*, vol. 30, no. 5, pp. 933–940, Sep. 1992. (Cited on page 13.)

[45] C. E. Livingstone, A. L. Gray, P. W. Vachon, M. Lalonde, R. K. Hawkins, T. I. Lukowski, K. Mattar, and J. W. Campbell, "The Canadian airborne R&D SAR facility: the CCRS C/X SAR," in *Proc. IEEE International Geoscience and Remote Sensing Symposium (IGARSS'96)*, Lincoln (Nebraska, USA), May 1996. (Cited on page 13.)

[46] E. L. Christensen and J. Dall, "EMISAR: a dual-frequency, polarimetric airborne SAR," in *Proc. IEEE International Geoscience and Remote Sensing Symposium (IGARSS'02)*, Toronto (Canda), Jun. 2002. (Cited on page 13.)

[47] R. Horn, "The DLR airborne SAR project E-SAR," in *Proc. International Geoscience and Remote Sensing Symposium (IGARSS'96)*, Lincoln (Nebraska, USA), May 1996. (Cited on page 13.)

[48] P. Dubois-Fernandez, O. R. du Plessis, D. le Coz, J. Dupas, B. Vaizan, X. Dupuis, H. Cantalloube, C. Coulombeix, C. Titin-Schnaider, P. Dreuillet, J. M. Boutry, J. P. Canny, L. Kaisersmertz, J. Peyret, P. Martineau, M. Chanteclerc, L. Pastore, and J. P. Bruyant, "The ONERA RAMSES SAR system," in *Proc. IEEE International Geoscience and Remote Sensing Symposium (IGARSS'02)*, Toronto (Canda), Jun. 2002. (Cited on page 13.)

[49] L. Pipia, X. Fabregas, A. Aguasca, C. López-Martínez, S. Duque, J. J. Mallorqui, and J. Marturia, "Polarimetric Differential SAR Interferometry: First Results With Ground-Based Measurements," *IEEE Geoscience and Remote Sensing Letters*, vol. 6, no. 1, pp. 167–171, Jan. 2009. (Cited on pages 13, 18, and 138.)

[50] L. Pipia, X. Fabregas, A. Aguasca, C. López-Martínez, and J. J. Mallorqui, "Polarimetric coherence optimization for interferometric differential applications," in *Proc. IEEE International Geoscience and Remote Sensing Symposium (IGARSS'09)*, Cape Town (South Africa), Jul. 2009. (Cited on pages 13 and 138.)

[51] T. Borner, K. P. Papathanassiou, N. Marquart, M. Zink, M. Meininger, P. J. Meadows, A. J. Rye, P. Wright, and B. Rosich Tell, "ALOS PALSAR products verification," in *Proc. IEEE International Geoscience and Remote Sensing Symposium (IGARSS'07)*, Barcelona (Spain), Jul. 2007. (Cited on page 14.)

[52] A. Rosenqvist, M. Shimada, N. Ito, and M. Watanabe, "ALOS PALSAR: A Pathfinder Mission for Global-Scale Monitoring of the Environment," *IEEE Transactions on Geoscience and Remote Sensing*, vol. 45, no. 11, pp. 3307–3316, Nov. 2007. (Cited on page 14.)

[53] S. Buckreuss, W. Balzer, P. Muhlbauer, R. Werninghaus, and W. Pitz, "The TerraSAR-X satellite project," in *Proc. IEEE International Geoscience and Remote Sensing Symposium (IGARSS'03)*, Toulouse (France), Jul. 2003. (Cited on pages 15 and 184.)

[54] S. Buckreuss and A. Roth, "Status Report on the TerraSAR-X Mission," in *Proc. IEEE International Geoscience and Remote Sensing Symposium (IGARSS'08)*, Boston (Massachusetts, USA), Jul. 2008. (Cited on pages 15 and 184.)

[55] L. C. Morena, K. V. James, and J. Beck, "An introduction to the RADARSAT-2 mission," *Canadian Journal of Remote Sensing*, vol. 30, no. 3, pp. 221–234, Apr. 2004. (Cited on page 15.)

[56] R. Venturini, F. Fois, G. Sirocchi, A. Bauleo, A. Bazzoni, L. Borgarelli, P. Capece, L. Cereoli, R. Croci, C. Farina, P. Pepe, C. Scarchilli, A. Torre, A. Capuzi, and F. Caltagirone, "Experimental verification of COSMO-SkyMed SAR capabilities," in *Proc. 2008 IEEE Radar Conference*, Rome (Iyaly), May 2008. (Cited on pages 15 and 184.)

[57] J. H. Gonzalez, M. Bachmann, H. Fiedler, S. Huber, G. Krieger, and M. Zink, "DEM calibration concept for TanDEM-X," in *Proc. IEEE International Geoscience and Remote Sensing Symposium (IGARSS'07)*, Barcelona (Spain), Jul. 2007. (Cited on page 15.)

[58] G. Krieger, M. Zink, H. Fiedler, I. Hajnsek, M. Younis, S. Huber, M. Bachmann, J. H. Gonzalez, D. Schulze, J. Boer, M. Werner, and A. Moreira, "The TanDEM-X

Mission: Overview and status," in *Proc. 2009 IEEE Radar Conference (RADAR'09)*, Pasadena (California), May 2009. (Cited on page 15.)

[59] P. Snoeij, E. Attema, A. Pietropaolo, V. Mastroddi, M. L'Abbate, and C. Bruno, "Analysis of Sentinel-1 mission capabilities," in *Proc. IEEE International Geoscience and Remote Sensing Symposium (IGARSS'09)*, Cape Town (South Africa), Jul. 2009. (Cited on page 16.)

[60] M. Shimada, "ALOS-2 science program," in *Proc. IEEE International Geoscience and Remote Sensing Symposium (IGARSS'13)*, Cape Town (South Africa), Jul. 2013. (Cited on page 16.)

[61] Y. Kankaku, S. Suzuki, and Y. Osawa, "ALOS-2 mission and development status," in *Proc. IEEE International Geoscience and Remote Sensing Symposium (IGARSS'13)*, Melbourne (Australia), Jul. 2013. (Cited on page 16.)

[62] M. J. Gonzalez, E. Vega, N. Alfaro, and B. Gomez, "PAZ ground segment," in *Proc. IEEE International Geoscience and Remote Sensing Symposium (IGARSS'12)*, Munich (Germany), Jul. 2012. (Cited on page 16.)

[63] J. Janoth, S. Gantert, W. Koppe, A. Kaptein, and C. Fischer, "TerraSAR-X2 Mission overview," in *Proc. IEEE International Geoscience and Remote Sensing Symposium (IGARSS'12)*, Munich (Germany), Jul. 2012. (Cited on page 16.)

[64] M. I. Skolnik, *Radar handbook*. Mc Graw-Hill, 1990. (Cited on pages 17 and 44.)

[65] D. Tarchi, H. Rudolf, G. Luzi, L. Chiarantini, P. Coppo, and A. J. Sieber, "SAR interferometry for structural changes detection: a demonstration test on a dam," in *Proc. International Geoscience and Remote Sensing Symposium (IGARSS'99)*, Hamburg (Germany), Jun. 1999. (Cited on pages 17 and 18.)

[66] H. Rudolf, D. Leva, D. Tarchi, and A. J. Sieber, "A mobile and versatile SAR system," in *Proc. IEEE International Geoscience and Remote Sensing Symposium (IGARSS'99)*, Hamburg (Germany), Jun. 1999. (Cited on page 17.)

[67] D. Leva, G. Nico, D. Tarchi, J. Fortuny-Guasch, and A. J. Sieber, "Temporal analysis of a landslide by means of a ground-based SAR interferometer," *IEEE Transactions on Geoscience and Remote Sensing*, vol. 41, no. 4, pp. 745–752, Apr. 2003. (Cited on pages 17, 32, and 122.)

[68] S. C. M. Brown, S. Quegan, K. Morrison, J. C. Bennett, and G. Cookmartin, "High-resolution measurements of scattering in wheat canopies-implications for crop parameter retrieval," *IEEE Transactions on Geoscience and Remote Sensing*, vol. 41, no. 7, pp. 1602–1610, Jul. 2003. (Cited on page 17.)

[69] G. Luzi, M. Pieraccini, D. Mecatti, L. Noferini, G. Guidi, F. Moia, and C. Atzeni, "Ground-based radar interferometry for landslides monitoring: atmospheric and instrumental decorrelation sources on experimental data," *IEEE Transactions on Geoscience and Remote Sensing*, vol. 42, no. 11, pp. 2454–2466, Nov. 2004. (Cited on pages 17 and 18.)

[70] L. Noferini, M. Pieraccini, D. Mecatti, G. Luzi, C. Atzeni, A. Tamburini, and M. Broccolato, "Permanent scatterers analysis for atmospheric correction in ground-based SAR interferometry," *IEEE Transactions on Geoscience and Remote Sensing*, vol. 43, no. 7, pp. 1459–1471, Jul. 2005. (Cited on pages 17 and 122.)

[71] M. Pieraccini, G. Luzi, and C. Atzeni, "Ground-based interferometric SAR for terrain elevation mapping," *Electronics Letters*, vol. 36, no. 16, pp. 1416–1417, Aug. 2000. (Cited on page 17.)

[72] Z. Zhou, W. Boerner, and M. Sato, "Development of a ground-based polarimetric broadband SAR system for noninvasive ground-truth validation in vegetation monitoring," *IEEE Transactions on Geoscience and Remote Sensing*, vol. 42, no. 9, pp. 1803–1810, Sep. 2004. (Cited on page 17.)

[73] C. Del Ventisette, E. Intrieri, G. Luzi, N. Casagli, R. Fanti, and D. Leva, "Using ground based radar interferometry during emergency: the case of the A3 motorway (Calabria Region, Italy) threatened by a landslide," *Natural Hazards and Earth System Science*, vol. 11, no. 9, pp. 2483–2495, Sep. 2011. (Cited on page 17.)

[74] Hoonyol, J. Lee, K. Kim, N. Sung, and S. Cho, "Development of a Truck-Mounted Arc-Scanning Synthetic Aperture Radar," *IEEE Transactions on Geoscience and Remote Sensing*, vol. 52, no. 5, pp. 2773–2779, May 2014. (Cited on page 17.)

[75] G. Bernardini, P. Ricci, and F. Coppi, "A ground based microwave interferometer with imaging capabilities for remote measurements of displacements," in *Proc. Geotelematics Fair*, Castelldefels (Barcelona, Spain), Feb. 2007. (Cited on page 17.)

[76] P. Farina, L. Leoni, F. Babboni, F. Coppi, L. Mayer, and P. Ricci, "IBIS-M , an Innovative Radar for Monitoring Slopes in Open-Pit Mines," in *Proc. Interrnational Symposium on Rock Slope Stability in Open Pit Mining and Civil Engineering*, Vancouver (Canada), Sep. 2011. (Cited on pages 17 and 18.)

[77] P. Farina and N. Coli, "Efficient Real Time Stability Monitoring of Mine Walls: The Çöllolar Mine Case Study," in *Proc. 23rd International Mining Congress and Exhibition of Turkey*, Antalya (Turkey), Apr. 2013. (Cited on pages 17 and 18.)

[78] A. Aguasca, A. Broquetas, J. J. Mallorqui, and X. Fabregas, "A solid state L to X-band flexible ground-based SAR system for continuous monitoring applications," in *Proc. IEEE International Geoscience and Remote Sensing Symposium (IGARSS'04)*, Anchorage (Alaska, USA), Sep. 2004. (Cited on pages 17 and 18.)

[79] L. Pipia, "Polarimetric Differential SAR Interferometry with Ground-Based Sensors," Ph.D. dissertation, Universitat Politècnica de Catalunya, 2009. (Cited on pages 18 and 138.)

[80] C. Werner, T. Strozzi, A. Wiesmann, and U. Wegmüller, "GAMMA's Portable Radar Interferometer," in *Proc. 13th FIG Symposium on Deformation Measurements and Analysis*, Lisbon (Protugal), May 2008. (Cited on page 18.)

[81] S. Rodelsperger, A. Coccia, D. Vicente, and A. Meta, "Introduction to the new metasensing ground-based SAR: Technical description and data analysis," in *Proc. IEEE International Geoscience and Remote Sensing Symposium (IGARSS'12)*, Munich (Germany), Jul. 2012. (Cited on pages 18 and 253.)

[82] K. Lukin and A. Mogyla, "Monitoring of St. Sophia Cathedral interior using Ka-band Ground Based Noise Waveform SAR," in *Proc. 2009 European Radar Conference (EuRAD'2009)*, Rome (Italy), Sep. 2009. (Cited on page 18.)

[83] O. Monserrat, M. Crosetto, and G. Luzi, "A review of ground-based SAR interferometry for deformation measurement," *ISPRS Journal of Photogrammetry and Remote*

Sensing, vol. 93, pp. 40–48, Jul. 2014. (Cited on pages 18 and 19.)

[84] N. Harries, D. Noon, H. Pritchett, and D. Bates, "Slope Stability Radar for Managing Rock Fall Risks in Open Cut Mines," in *Proc. 3rd CANUS Rock Mechanics Symposium*, Toronto (Canada), May 2009. (Cited on page 18.)

[85] D. Mecatti, G. Macaluso, A. Barucci, L. Noferini, M. Pieraccini, and C. Atzeni, "Monitoring Open-Pit Quarries by Interferometric Radar for Safety Purposes," in *Proc. 2010 European Radar Conference (EuRAD'10)*, Paris (France), Sep. 2010. (Cited on page 18.)

[86] D. Tarchi, G. Antonello, N. Casagli, P. Farina, J. Fortuny-Guasch, L. Guerri, and D. Leva, "On the Use of Ground-Based SAR Interferometry for Slope Failure Early Warning: the Cortenova Rock Slide (Italy)," in *Landslides*, K. Sassa, H. Fukuoka, F. Wang, and G. Wang, Eds. Springer Berlin Heidelberg, 2005, pp. 337–342. (Cited on page 18.)

[87] D. Tarchi, "Monitoring landslide displacements by using ground-based synthetic aperture radar interferometry: Application to the Ruinon landslide in the Italian Alps," *Journal of Geophysical Research*, vol. 108, no. B8, pp. 2387–2401, Aug. 2003. (Cited on page 18.)

[88] N. Casagli, F. Catani, C. Del Ventisette, and G. Luzi, "Monitoring, prediction, and early warning using ground-based radar interferometry," *Landslides*, vol. 7, no. 3, pp. 291–301, May 2010. (Cited on page 18.)

[89] M. Pieraccini, G. Luzi, D. Mecatti, M. Fratini, L. Noferini, L. Carissimi, G. Franchioni, and C. Atzeni, "Remote sensing of building structural displacements using a microwave interferometer with imaging capability," *NDT and E International*, vol. 37, no. 7, pp. 545–550, Oct. 2004. (Cited on page 18.)

[90] L. Pipia, X. Fabregas, A. Aguasca, and C. López-Martínez, "Polarimetric Temporal Analysis of Urban Environments With a Ground-Based SAR," *IEEE Transactions on Geoscience and Remote Sensing*, vol. 51, no. 4, pp. 2343–2360, Apr. 2013. (Cited on page 18.)

[91] D. Tarchi, E. Ohlmer, and A. Sieber, "Monitoring of Structural Changes by Radar Interferometry," *Research in Nondestructive Evaluation*, vol. 9, no. 4, pp. 213–225, Jan. 1997. (Cited on page 18.)

[92] O. Montserrat, "Deformation measurement and monitoring with Ground-Based SAR," Ph.D. dissertation, Universitat Politècnica de Catalunya, 2012. (Cited on page 18.)

[93] L. Noferini, D. Mecatti, G. Macaluso, M. Pieraccini, and C. Atzeni, "Monitoring of Belvedere Glacier using a wide angle GB-SAR interferometer," *Journal of Applied Geophysics*, vol. 68, no. 2, pp. 289–293, Jun. 2009. (Cited on page 18.)

[94] J. Corominas and E. Alonso, "Inestabilidad de laderas en el Pirineo catalán. Tipología y causas," in *Proc. Jornadas de trabajo sobre inestabilidad de laderas en el Pirineo*, Barcelona (Spain), Jan. 1984. (Cited on page 19.)

[95] N. Santacana, "Estudi dels grans esllavissaments d'Andorra: Els casos del Forn i del vessant d'Encampadana," Ph.D. dissertation, Universitat Politècnica de Catalunya (UPC), 1994. (Cited on pages 19 and 20.)

[96] I. Torrebadella, I. Villaró, J. Altimir, J. Amigó, J. M. Vilaplana, J. Corominas, and X. Planas, "El Deslizamiento del Forn de Canilloen Andorra. Un Ejemplo de Gestión del Riesgo Geológico en Zonas Habitadas en Grandes Deslizamientos," in *Proc. VII Simposio Nacional sobre Taludes y Laderas Inestables*, Barcelona (Spain), Oct. 2009. (Cited on pages 22 and 113.)

[97] M. Eineder, N. Adam, R. Bamler, N. Yague-Martinez, and H. Breit, "Spaceborne Spotlight SAR Interferometry With TerraSAR-X," *IEEE Transactions on Geoscience and Remote Sensing*, vol. 47, no. 5, pp. 1524–1535, May 2009. (Cited on pages 25, 57, 264, 265, and 266.)

[98] T. Strozzi, P. Farina, A. Corsini, C. Ambrosi, M. Thüring, J. Zilger, A. Wiesmann, U. Wegmüller, and C. Werner, "Survey and monitoring of landslide displacements by means of L-band satellite SAR interferometry," *Landslides*, vol. 2, no. 3, pp. 193–201, Oct. 2005. (Cited on page 30.)

[99] G. Herrera, D. Notti, J. C. Garcia-Davalillo, O. Mora, G. Cooksley, M. Sanchez, A. Arnaud, and M. Crosetto, "Analysis with C- and X-band satellite SAR data of the Portalet landslide area," *Landslides*, vol. 8, no. 2, pp. 195–206, Sep. 2010. (Cited on page 31.)

[100] D. Notti, J. C. Garcia-Davalillo, G. Herrera, and O. Mora, "Assessment of the performance of X-band satellite radar data for landslide mapping and monitoring: Upper Tena Valley case study," *Natural Hazards and Earth System Science*, vol. 10, no. 9, pp. 1865–1875, Sep. 2010. (Cited on page 31.)

[101] M. Liao, J. Tang, T. Wang, T. Balz, and L. Zhang, "Landslide monitoring with high-resolution SAR data in the Three Gorges region," *Science China Earth Sciences*, vol. 55, no. 4, pp. 590–601, Dec. 2011. (Cited on page 31.)

[102] F. Bovenga, J. Wasowski, D. O. Nitti, R. Nutricato, and M. T. Chiaradia, "Using COSMO/SkyMed X-band and ENVISAT C-band SAR interferometry for landslides analysis," *Remote Sensing of Environment*, vol. 119, pp. 272–285, Apr. 2012. (Cited on page 31.)

[103] G. Herrera, J. A. Fernandez-Merodo, J. Mulas, M. Pastor, G. Luzi, and O. Monserrat, "A landslide forecasting model using ground based SAR data: The Portalet case study," *Engineering Geology*, vol. 105, no. 3-4, pp. 220–230, May 2009. (Cited on page 32.)

[104] G. Barla, F. Antolini, M. Barla, E. Mensi, and G. Piovano, "Monitoring of the Beauregard landslide (Aosta Valley, Italy) using advanced and conventional techniques," *Engineering Geology*, vol. 116, no. 3-4, pp. 218–235, Nov. 2010. (Cited on page 32.)

[105] R. Iglesias, X. Fabregas, A. Aguasca, J. J. Mallorqui, C. López-Martínez, J. A. Gili, and J. Corominas, "Atmospheric Phase Screen Compensation in Ground-Based SAR With a Multiple-Regression Model Over Mountainous Regions," *IEEE Transactions on Geoscience and Remote Sensing*, vol. 52, no. 5, pp. 2436–2449, May 2014. (Cited on page 34.)

[106] R. Iglesias, D. Monells, X. Fabregas, J. J. Mallorqui, A. Aguasca, and C. López-Martínez, "Phase Quality Optimization in Polarimetric Differential SAR Interferometry," *IEEE Transactions on Geoscience and Remote Sensing*, vol. 52, no. 5, pp.

2875–2888, May 2014. (Cited on page 34.)

[107] R. Iglesias, A. Aguasca, X. Fabregas, J. J. Mallorqui, D. Monells, C. López-Martínez, and L. Pipia, "Ground-Based Polarimetric SAR Interferometry for the Monitoring of Terrain Displacement Phenomena - Part I: Theoretical Description," *IEEE Journal of Selected Topics in Applied Earth Observations and Remote Sensing*, vol. 8, no. 3, pp. 980–993, Mar. 2015. (Cited on page 34.)

[108] ——, "Ground-Based Polarimetric SAR Interferometry for the Monitoring of Terrain Displacement Phenomena - Part II: Applications," *IEEE Journal of Selected Topics in Applied Earth Observations and Remote Sensing*, vol. 8, no. 3, pp. 994–1007, Mar. 2015. (Cited on page 34.)

[109] R. Iglesias, J. J. Mallorqui, and P. López-Dekker, "DInSAR Pixel Selection Based on Sublook Spectral Correlation Along Time," *IEEE Transactions on Geoscience and Remote Sensing*, vol. 52, no. 7, pp. 3788–3799, Jul. 2014. (Cited on page 34.)

[110] R. Iglesias, D. Monells, C. López-Martínez, J. J. Mallorqui, X. Fabregas, and A. Aguasca, "Polarimetric Optimization of Temporal Sublook Coherence for DInSAR Applications," *IEEE Geoscience and Remote Sensing Letters*, vol. 12, no. 1, pp. 87–91, Jan. 2015. (Cited on page 34.)

[111] R. Iglesias, J. J. Mallorqui, D. Monells, C. López-Martínez, X. Fabregas, A. Aguasca, J. A. Gili, and J. Corominas, "PSI Deformation Map Retrieval by Means of Temporal Sublook Coherence on Reduced Sets of SAR Images," *Remote Sensing*, vol. 7, no. 1, pp. 530–563, Jan. 2015. (Cited on page 34.)

[112] A. Cardama, L. Jofre, J. M. Rius, J. Romeu, and S. Blach, *Antenas.* EDICIONS UPC, 2002. (Cited on pages 38 and 44.)

[113] J. C. Curlander and R. N. McDonough, *Synthetic Aperture Radar: Systems and Signal Processing.* Wiley-Interscience, 1991. (Cited on pages 39, 41, 44, and 46.)

[114] G. Franceschetti and R. Lanari, *Synthetic Aperture Radar Processing.* CRC Press, 1999. (Cited on page 39.)

[115] I. G. Cumming and F. Wong, *Digital Processing of Synthetic Aperture Radar Data: Algorithms and Implementation.* Artech House, 2005. (Cited on page 41.)

[116] R. K. Raney, H. Runge, R. Bamler, I. G. Cumming, and F. H. Wong, "Precision SAR processing using chirp scaling," *IEEE Transactions on Geoscience and Remote Sensing*, vol. 32, no. 4, pp. 786–799, Jul. 1994. (Cited on page 43.)

[117] A. Moreira, J. Mittermayer, and R. Scheiber, "Extended chirp scaling algorithm for air- and spaceborne SAR data processing in stripmap and ScanSAR imaging modes," *IEEE Transactions on Geoscience and Remote Sensing*, vol. 34, no. 5, pp. 1123–1136, Sep. 1996. (Cited on page 43.)

[118] J. Mittermayer, A. Moreira, S. Member, and O. Loffeld, "Spotlight SAR Data Processing Using the Frequency Scaling Algorithm," *IEEE Transactions on Geoscience and Remote Sensing*, vol. 37, no. 5, pp. 2198–2214, Sep. 1999. (Cited on page 43.)

[119] F. T. Ulaby, R. K. Moore, and A. K. Fung, *Microwave Remote Sensing: Active and Passive - Volume II: Radar Remote Sensing and Surface Scattering and Emission Theory.* Addison-Wesley, 1986. (Cited on pages 44 and 47.)

[120] G. Schreier, *SAR geocoding: data and systems*. Wichman, 1993. (Cited on page 45.)

[121] L. Krul, "Principles of radar measurement," in *Radar Calibration*. Provided by the SAO/NASA Astrophysics Data System, 1983, pp. 11–21. (Cited on page 46.)

[122] J. W. Goodman, *Laser Speckle and Related Phenomena*. Springer, 1975. (Cited on page 46.)

[123] J.-S. Lee, "Speckle analysis and smoothing of synthetic aperture radar images," *Computer Graphics and Image Processing*, vol. 17, no. 1, pp. 24–32, Sep. 1981. (Cited on page 46.)

[124] C. López-Martínez, "Multidimensional Speckle Noise, Modelling and Filtering Related to SAR Data," Ph.D. dissertation, Universitat Politècnica de Catalunya, 2003. (Cited on page 47.)

[125] A. Lopes, E. Nezry, R. Touzi, and H. Laur, "Structure detection and statistical adaptive speckle filtering in SAR images," *International Journal of Remote Sensing*, vol. 14, no. 9, pp. 1735–1758, Jun. 1993. (Cited on page 47.)

[126] G. Schreier, *SAR Geocoding: Data and Systems*. Wichmann, 2001. (Cited on page 48.)

[127] E. Sansosti, P. Berardino, M. Manunta, F. Serafino, and G. Fornaro, "Geometrical SAR image registration," *IEEE Transactions on Geoscience and Remote Sensing*, vol. 44, no. 10, pp. 2861–2870, Oct. 2006. (Cited on page 51.)

[128] R. M. Goldstein, H. A. Zebker, and C. L. Werner, "Satellite radar interferometry: Two-dimensional phase unwrapping," *Radio Science*, vol. 23, no. 4, pp. 713–720, Jul. 1988. (Cited on page 54.)

[129] D. C. Ghiglia and L. A. Romero, "Robust two-dimensional weighted and unweighted phase unwrapping that uses fast transforms and iterative methods," *Journal of the Optical Society of America A*, vol. 11, no. 1, pp. 107–117, Jan. 1994. (Cited on page 54.)

[130] U. Spagnolini, "2-D phase unwrapping and instantaneous frequency estimation," *IEEE Transactions on Geoscience and Remote Sensing*, vol. 33, no. 3, pp. 579–589, May 1995. (Cited on page 54.)

[131] G. Fornaro, G. Franceschetti, and R. Lanari, "Interferometric SAR phase unwrapping using Green's formulation," *IEEE Transactions on Geoscience and Remote Sensing*, vol. 34, no. 3, pp. 720–727, May 1996. (Cited on page 54.)

[132] A. Reigber and J. Moreira, "Phase unwrapping by fusion of local and global methods," in *Proc. IEEE International Geoscience and Remote Sensing Symposium (IGARSS'97)*, Singapore (Singapore), Aug. 1997. (Cited on page 54.)

[133] M. Costantini, "A novel phase unwrapping method based on network programming," *IEEE Transactions on Geoscience and Remote Sensing*, vol. 36, no. 3, pp. 813–821, May 1998. (Cited on page 54.)

[134] W. Xu and I. G. Cumming, "A region-growing algorithm for InSAR phase unwrapping," *IEEE Transactions on Geoscience and Remote Sensing*, vol. 37, no. 1, pp. 124–134, Jan. 1999. (Cited on pages 54 and 103.)

[135] A. Pepe and R. Lanari, "On the Extension of the Minimum Cost Flow Algorithm for

Phase Unwrapping of Multitemporal Differential SAR Interferograms," *IEEE Transactions on Geoscience and Remote Sensing*, vol. 44, no. 9, pp. 2374–2383, Sep. 2006. (Cited on page 54.)

[136] C. W. Chen and H. A. Zebker, "Two-dimensional phase unwrapping with use of statistical models for cost functions in nonlinear optimization," *Journal of the Optical Society of America A*, vol. 18, no. 2, pp. 338–351, Feb. 2001. (Cited on page 54.)

[137] T. G. Farr, P. A. Rosen, E. Caro, R. Crippen, R. Duren, S. Hensley, M. Kobrick, M. Paller, E. Rodriguez, L. Roth, D. Seal, S. Shaffer, J. Shimada, J. Umland, M. Werner, M. Oskin, D. Burbank, and D. Alsdorf, "The Shuttle Radar Topography Mission," *Reviews of Geophysics*, vol. 45, no. 2, pp. 1–33, May 2007. (Cited on page 54.)

[138] C. Rossi and M. Eineder, "TanDEM-X mission: raw DEM generation," in *Proc. 8th European Conference on Synthetic Aperture Radar (EUSAR'10)*, Aachen (Germany), Jun. 2010. (Cited on page 54.)

[139] R. Deo, S. Manickam, Y. S. Rao, and S. S. Gedam, "Evaluation of interferometric SAR DEMs generated using TanDEM-X data," in *Proc. IEEE International Geoscience and Remote Sensing Symposium (IGARSS'13)*, Melbourne (Australia), Jul. 2013. (Cited on page 54.)

[140] J. Mittermayer, S. Wollstadt, P. Prats-Iraola, and R. Scheiber, "The TerraSAR-X Staring Spotlight Mode Concept," *IEEE Transactions on Geoscience and Remote Sensing*, vol. 52, no. 6, pp. 3695–3706, Jun. 2014. (Cited on pages 57 and 248.)

[141] R. Bamler and P. Hartl, "Synthetic aperture radar interferometry," *Inverse Problems*, vol. 14, no. 4, pp. 1–54, Aug. 1998. (Cited on pages 61 and 85.)

[142] P. A. Rosen, S. Hensley, I. R. Joughin, F. K. Li, S. N. Madsen, E. Rodriguez, and R. M. Goldstein, "Synthetic aperture radar interferometry," *Proceedings of the IEEE*, vol. 88, no. 3, pp. 333–382, Mar. 2000. (Cited on pages 61 and 85.)

[143] M. S. Seymour and I. G. Cumming, "Maximum likelihood estimation for SAR interferometry," in *Proc. IEEE International Geoscience and Remote Sensing Symposium (IGARSS'94)*, Pasadena (California , USA), Aug. 1994. (Cited on pages 62 and 85.)

[144] R. Touzi, A. Lopes, J. Bruniquel, and P. Vachon, "Coherence estimation for SAR imagery," *IEEE Transactions on Geoscience and Remote Sensing*, vol. 37, no. 1, pp. 135–149, Jan. 1999. (Cited on pages 62, 85, and 86.)

[145] H. A. Zebker and J. Villasenor, "Decorrelation in interferometric radar echoes," *IEEE Transactions on Geoscience and Remote Sensing*, vol. 30, no. 5, pp. 950–959, Sep. 1992. (Cited on pages 63 and 64.)

[146] F. Gatelli, A. Monti Guarnieri, F. Parizzi, P. Pasquali, C. Prati, and F. Rocca, "The wavenumber shift in SAR interferometry," *IEEE Transactions on Geoscience and Remote Sensing*, vol. 32, no. 4, pp. 855–865, Jul. 1994. (Cited on pages 63, 65, and 66.)

[147] A. Reigber, "Range dependent spectral filtering to minimize the baseline decorrelation in airborne SAR interferometry," in *Proc. IEEE International Geoscience and Remote Sensing Symposium (IGARSS'99)*, Hamburg (Germany), Jun. 1999. (Cited on page 66.)

[148] S. Guillaso, A. Reigber, L. Ferro-Famil, and E. Pottier, "Range resolution improvement of airborne SAR images," *IEEE Geoscience and Remote Sensing Letters*, vol. 3, no. 1, pp. 135–139, Jan. 2006. (Cited on page 66.)

[149] R. M. Goldstein, "Atmospheric limitations to repeat-track radar interferometry," *Geophysical Research Letters*, vol. 22, no. 18, pp. 2517–2520, Sep. 1995. (Cited on page 70.)

[150] H. A. Zebker, P. A. Rosen, and S. Hensley, "Atmospheric effects in interferometric synthetic aperture radar surface deformation and topographic maps," *Journal of Geophysical Research: Solid Earth*, vol. 102, no. B4, pp. 7547–7563, Apr. 1997. (Cited on page 70.)

[151] Z. Li, J. Muller, P. Cross, and E. J. Fielding, "Interferometric synthetic aperture radar (InSAR) atmospheric correction: GPS, Moderate Resolution Imaging Spectroradiometer (MODIS), and InSAR integration," *Journal of Geophysical Research: Solid Earth*, vol. 110, no. B3, pp. 1–10, Mar. 2005. (Cited on page 70.)

[152] A. Eff-Darwich, J. C. Pérez, J. Fernández, B. García-Lorenzo, A. González, and P. J. González, "Using a Mesoscale Meteorological Model to Reduce the Effect of Tropospheric Water Vapour from DInSAR Data: A Case Study for the Island of Tenerife, Canary Islands," *Pure and Applied Geophysics*, vol. 169, no. 8, pp. 1425–1441, Aug. 2012. (Cited on page 70.)

[153] C. Delacourt, P. Briole, and J. A. Achache, "Tropospheric corrections of SAR interferograms with strong topography. Application to Etna," *Geophysical Research Letters*, vol. 25, no. 15, pp. 2849–2852, Aug. 1998. (Cited on page 71.)

[154] S. Williams, Y. Bock, and P. Fang, "Integrated satellite interferometry: Tropospheric noise, GPS estimates and implications for interferometric synthetic aperture radar products," *Journal of Geophysical Research: Solid Earth*, vol. 103, no. B11, pp. 27 051–27 067, Nov. 1998. (Cited on page 71.)

[155] P. W. Webley, R. M. Bingley, A. H. Dodson, G. Wadge, S. J. Waugh, and I. N. James, "Atmospheric water vapour correction to InSAR surface motion measurements on mountains: results from a dense GPS network on Mount Etna," *Physics and Chemistry of the Earth*, vol. 27, no. 4–5, pp. 363–370, Nov. 2002. (Cited on page 71.)

[156] F. Beauducel, P. Briole, and J. Froger, "Volcano-wide fringes in ERS synthetic aperture radar interferograms of Etna (1992-1998): Deformation or tropospheric effect?" *Journal of Geophysical Research: Solid Earth*, vol. 105, no. B7, pp. 16 391–16 402, Jul. 2000. (Cited on page 71.)

[157] D. Remy, S. Bonvalot, P. Briole, and M. Murakami, "Accurate measurements of tropospheric effects in volcanic areas from SAR interferometry data: application to Sakurajima volcano (Japan)," *Earth and Planetary Science Letters*, vol. 213, no. 3–4, pp. 299 – 310, Aug. 2003. (Cited on page 71.)

[158] J. Biggs, T. Wright, Z. Lu, and B. Parsons, "Multi-interferogram method for measuring interseismic deformation: Denali Fault, Alaska," *Geophysical Journal International*, vol. 170, no. 3, pp. 1165–1179, Aug. 2007. (Cited on page 71.)

[159] O. Cavalič, C. Lasserre, M.-P. Doin, G. Peltzer, J. Sun, X. Xu, and Z.-K. Shen, "Measurement of interseismic strain across the Haiyuan fault (Gansu, China), by

InSAR," *Earth and Planetary Science Letters* , vol. 275, no. 3–4, pp. 246–257, Nov. 2008. (Cited on page 71.)

[160] G. A. Grell, J. Dudhia, and D. R. Stauffer, *A description of the fifth-generation Penn State/NCAR mesoscale model (MM5).* National Center for Atmospheric Research, 1994. (Cited on page 71.)

[161] J. Foster, B. Brooks, T. Cherubini, C. Shacat, S. Businger, and C. L. Werner, "Mitigating atmospheric noise for InSAR using a high resolution weather model," *Geophysical Research Letters*, vol. 33, no. 16, pp. 16 304–16 309, Aug. 2006. (Cited on page 71.)

[162] G. Nico, R. Tome, J. Catalao, and P. Miranda, "On the Use of the WRF Model to Mitigate Tropospheric Phase Delay Effects in SAR Interferograms," *IEEE Transactions on Geoscience and Remote Sensing*, vol. 49, no. 12, pp. 4970–4976, Dec. 2011. (Cited on page 71.)

[163] R. Jolivet, R. Grandin, C. Lasserre, M.-P. Doin, and G. Peltzer, "Systematic InSAR tropospheric phase delay corrections from global meteorological reanalysis data," *Geophysical Research Letters*, vol. 38, no. 17, pp. 1–6, Sep. 2011. (Cited on page 71.)

[164] P. Mateus, G. Nico, R. Tome, J. Catalao, and P. Miranda, "Experimental Study on the Atmospheric Delay Based on GPS, SAR Interferometry, and Numerical Weather Model Data," *IEEE Transactions on Geoscience and Remote Sensing*, vol. 51, no. 1, pp. 6–11, Jan. 2013. (Cited on page 71.)

[165] M.-P. Doin, C. Lasserre, G. Peltzer, O. Cavalié, and C. Doubre, "Corrections of stratified tropospheric delays in SAR interferometry: Validation with global atmospheric models," *Journal of Applied Geophysics*, vol. 69, no. 1, pp. 35–50, Sep. 2009. (Cited on page 71.)

[166] D. P. Dee, S. M. Uppala, A. J. Simmons, P. Berrisford, P. Poli, S. Kobayashi, U. Andrae, M. A. Balmaseda, G. Balsamo, P. Bauer, P. Bechtold, A. C. M. Beljaars, L. van de Berg, J. Bidlot, N. Bormann, C. Delsol, R. Dragani, M. Fuentes, A. J. Geer, L. Haimberger, S. B. Healy, H. Hersbach, E. V. Hólm, L. Isaksen, P. Kållberg, M. Köhler, M. Matricardi, A. P. McNally, B. M. Monge-Sanz, J.-J. Morcrette, B.-K. Park, C. Peubey, P. de Rosnay, C. Tavolato, J.-N. Thépaut, and F. Vitart, "The ERA-Interim reanalysis: configuration and performance of the data assimilation system," *Quarterly Journal of the Royal Meteorological Society*, vol. 137, no. 656, pp. 553–597, Apr. 2011. (Cited on page 71.)

[167] A. Pepe, P. Berardino, M. Bonano, L. D. Euillades, R. Lanari, and E. Sansosti, "SBAS-Based Satellite Orbit Correction for the Generation of DInSAR Time-Series: Application to RADARSAT-1 Data," *IEEE Transactions on Geoscience and Remote Sensing*, vol. 49, no. 12, pp. 5150–5165, Dec. 2011. (Cited on page 72.)

[168] C. A. Balanis, *Advanced Engineering Electromagnetics.* Wiley, 1989. (Cited on page 73.)

[169] G. Deschamps, "Techniques for Handling Elliptically Polarized Waves with Special Reference to Antennas: Part II-Geometrical Representation of the Polarization of a Plane Electromagnetic Wave," *Proceedings of the IRE*, vol. 39, no. 5, pp. 540–544, May 1951. (Cited on page 76.)

[170] E. Lüneburg, "Principles of radar polarimetry," pp. 1339–1345, Oct 1995. (Cited on pages 76 and 77.)

[171] M. Born and E. Wolf, *Principles of Optics: Electromagnetic Theory of Propagation, Interference and Diffraction of Light*. Cambridge University Press, 1999. (Cited on page 76.)

[172] S. R. Cloude, "Group theory and polarisation algebra," *Optik*, vol. 75, no. 1, pp. 26–36, Jan. 1986. (Cited on page 77.)

[173] J.-S. Lee and E. Pottier, *Polarimetric radar imaging: from basics to applications*. CRC Press, 2009. (Cited on page 77.)

[174] A. Kostinski and W. Boerner, "On foundations of radar polarimetry," *IEEE Transactions on Antennas and Propagation*, vol. 34, no. 12, pp. 1395–1404, Dec. 1986. (Cited on page 77.)

[175] S. Cloude, *Polarisation: applications in remote sensing*. Oxford Uni, 2009. (Cited on pages 78 and 79.)

[176] P. Blanco-Sánchez, J. J. Mallorquí, S. Duque, and D. Monells, "The Coherent Pixels Technique (CPT): An Advanced DInSAR Technique for Nonlinear Deformation Monitoring," *Pure and Applied Geophysics*, vol. 165, no. 6, pp. 1167–1193, Aug. 2008. (Cited on pages 82, 99, 102, and 104.)

[177] I. R. Joughin, D. P. Winebrenner, and D. B. Percival, "Probability density functions for multilook polarimetric signatures," *IEEE Transactions on Geoscience and Remote Sensing*, vol. 32, no. 3, pp. 562–574, May 1994. (Cited on page 87.)

[178] K. W. Hoppel, S. A. Mango, and A. R. Miller, "Intensity and phase statistics of multilook polarimetric and interferometric SAR imagery," *IEEE Transactions on Geoscience and Remote Sensing*, vol. 32, no. 5, pp. 1017–1028, Sep. 1994. (Cited on page 87.)

[179] D. Just and R. Bamler, "Phase statistics of interferograms with applications to synthetic aperture radar," *Applied Optiks*, vol. 33, no. 20, pp. 4361–4368, Jul. 1994. (Cited on page 88.)

[180] H. C. Stankwitz, R. J. Dallaire, and J. R. Fienup, "Nonlinear apodization for sidelobe control in SAR imagery," *IEEE Transactions on Aerospace and Electronic Systems*, vol. 31, no. 1, pp. 267–279, Jan. 1995. (Cited on pages 91, 92, and 272.)

[181] B. N. Delaunay, "Sur la sphère vide," *Bulletin of Academy of Sciences of the USSR*, no. 6, pp. 793–800, 1934. (Cited on page 97.)

[182] M. R. Hestenes and E. Stiefel, "Methods of Conjugate Gradients for Solving Linear Systems," *Journal of Research of the National Bureau of Standards*, vol. 49, no. 6, pp. 409–436, 1952. (Cited on pages 100, 103, and 287.)

[183] O. Alter, P. O. Brown, and D. Botstein, "Singular value decomposition for genome-wide expression data processing and modeling," *Proceedings of the National Academy of Sciences*, vol. 97, no. 18, Aug. 2000. (Cited on pages 110 and 299.)

[184] L. Pipia, X. Fabregas, A. Aguasca, and C. López-Martínez, "Atmospheric Artifact Compensation in Ground-Based DInSAR Applications," *IEEE Geoscience and Remote Sensing Letters*, vol. 5, no. 1, pp. 88–92, Jan. 2008. (Cited on page 122.)

[185] L. Pipia, X. Fabregas, A. Aguasca, and J. J. Mallorqui, "A Comparison of Different Techniques for Atmospheric Artefact Compensation in GBSAR Differential Acquisitions," in *Proc. IEEE International Symposium on Geoscience and Remote Sensing (IGARSS'06)*, Jul. 2006. (Cited on page 122.)

[186] L. Iannini and A. Monti Guarnieri, "Atmospheric Phase Screen in Ground-Based Radar: Statistics and Compensation," *IEEE Geoscience and Remote Sensing Letters*, vol. 8, no. 3, pp. 537–541, May 2011. (Cited on page 122.)

[187] V. D. Navarro-Sanchez, J. M. Lopez-Sanchez, and F. Vicente-Guijalba, "A Contribution of Polarimetry to Satellite Differential SAR Interferometry: Increasing the Number of Pixel Candidates," *IEEE Geoscience and Remote Sensing Letters*, vol. 7, no. 2, pp. 276–280, Apr. 2010. (Cited on page 138.)

[188] V. D. Navarro-Sanchez and J. M. Lopez-Sanchez, "Subsidence monitoring using polarimetric persistent scatterers interferometry," in *Proc. IEEE International Geoscience and Remote Sensing Symposium (IGARSS'11)*, Vancouver (Canada), Jul. 1997. (Cited on page 138.)

[189] ——, "Improvement of Persistent-Scatterer Interferometry Performance by Means of a Polarimetric Optimization," *IEEE Geoscience and Remote Sensing Letters*, vol. 9, no. 4, pp. 609–613, Jul. 2012. (Cited on page 138.)

[190] V. D. Navarro-Sanchez, J. M. Lopez-Sanchez, and L. Ferro-Famil, "Polarimetric Approaches for Persistent Scatterers Interferometry," *IEEE Transactions on Geoscience and Remote Sensing*, vol. 52, no. 3, pp. 1667–1676, Mar. 2014. (Cited on page 138.)

[191] R. Z. Schneider, K. P. Papathanassiou, I. Hajnsek, and A. Moreira, "Polarimetric and interferometric characterization of coherent scatterers in urban areas," *IEEE Transactions on Geoscience and Remote Sensing*, vol. 44, no. 4, pp. 971–984, Apr. 2006. (Cited on page 185.)

[192] P. Prats-Iraola, R. Scheiber, M. Rodriguez-Cassola, J. Mittermayer, S. Wollstadt, F. De Zan, B. Brautigam, M. Schwerdt, A. Reigber, and A. Moreira, "On the Processing of Very High Resolution Spaceborne SAR Data," *IEEE Transactions on Geoscience and Remote Sensing*, vol. 52, no. 10, pp. 6003–6016, Oct. 2014. (Cited on page 249.)

[193] F. De Zan and A. Monti Guarnieri, "TOPSAR: Terrain Observation by Progressive Scans," *IEEE Transactions on Geoscience and Remote Sensing*, vol. 44, no. 9, pp. 2352–2360, Sep. 2006. (Cited on page 250.)

[194] A. Meta, J. Mittermayer, U. Steinbrecher, and P. Prats-Iraola, "Investigations on the TOPSAR acquisition mode with TerraSAR-X," in *Proc. IEEE International Geoscience and Remote Sensing Symposium (IGARSS'07)*, Barcelona (Spain), Jul. 2007. (Cited on page 250.)

[195] A. Meta, P. Prats-Iraola, U. Steinbrecher, J. Mittermayer, and R. Scheiber, "TerraSAR-X TOPSAR and ScanSAR comparison," in *Proc. 7th European Conference on Synthetic Aperture Radar (EUSAR'08)*, Friedrichshafen (Germany), Jun. 2008. (Cited on page 250.)

[196] P. Prats-Iraola, R. Scheiber, L. Marotti, S. Wollstadt, and A. Reigber, "TOPS Interferometry With TerraSAR-X," *IEEE Transactions on Geoscience and Remote*

Sensing, vol. 50, no. 8, pp. 3179–3188, Aug. 2012. (Cited on pages 250 and 251.)

[197] C.-A. Deledalle, L. Denis, and F. Tupin, "Iterative weighted maximum likelihood denoising with probabilistic patch-based weights." *IEEE Transactions on Image Processing*, vol. 18, no. 12, pp. 2661–72, Dec. 2009. (Cited on page 251.)

[198] C.-A. Deledalle, F. Tupin, and L. Denis, "Polarimetric SAR estimation based on non-local means," in *Proc. IEEE International Geoscience and Remote Sensing Symposium (IGARSS'10)*, Honolulu (Hawaii, USA), Jun. 2010. (Cited on page 251.)

[199] C.-A. Deledalle, L. Denis, and F. Tupin, "NL-InSAR: Nonlocal Interferogram Estimation," *IEEE Transactions on Geoscience and Remote Sensing*, vol. 49, no. 4, pp. 1441–1452, Apr. 2011. (Cited on page 251.)

[200] A. Alonso-gonzález, C. López-martínez, S. Member, and P. Salembier, "Filtering and Segmentation of Polarimetric SAR Data Based on Binary Partition Trees," *IEEE Transactions on Geoscience and Remote Sensing*, vol. 50, no. 2, pp. 593–605, Feb. 2012. (Cited on page 251.)

[201] A. Alonso-González, C. López-Martínez, P. Salembier, and X. Deng, "Bilateral Distance Based Filtering for Polarimetric SAR Data," *Remote Sensing*, vol. 5, no. 11, pp. 5620–5641, Oct. 2013. (Cited on page 251.)

[202] F. Raspini, S. Moretti, and N. Casagli, "Landslide Mapping Using SqueeSAR Data: Giampilieri (Italy) Case Study," in *Landslide Science and Practice*, C. Margottini, P. Canuti, and K. Sassa, Eds. Springer Berlin Heidelberg, 2013, pp. 147–154. (Cited on page 252.)

[203] C. Meisina, D. Notti, F. Zucca, M. Ceriani, A. Colombo, F. Poggi, A. Roccati, and A. Zaccone, "The Use of PSInSAR and SqueeSAR Techniques for Updating Landslide Inventories," in *Landslide Science and Practice*, C. Margottini, P. Canuti, and K. Sassa, Eds. Springer Berlin Heidelberg, 2013, pp. 81–87. (Cited on page 252.)

[204] J. Duro, R. Iglesias, P. Blanco-Sánchez, and Albiol, "Improved PSI Performance for Landslide Monitoring Applications," in *9th International Workshop on Advances in the Science and Applications of SAR Interferometry (FRINGE'15)*, Frascati (Rome, Italy), Mar. 2015. (Cited on page 252.)

[205] R. Iglesias, D. Monells, G. Centolanza, J. J. Mallorqui, X. Fabregas, and A. Aguasca, "Down-slope Combination of Orbital and Ground-Based DInSAR for the Efficient Monitoring of Slow-Moving Landslides," in *Proc. 10th European Conference on Synthetic Aperture Radar (EUSAR'14)*, Berlin (Germany), Jun. 2014. (Cited on page 253.)

[206] O. Hungr, *Debris-flow Hazards and Related Phenomena*. Springer, 2005. (Cited on page 255.)

[207] J. Capon, "High-resolution frequency-wavenumber spectrum analysis," *Proceedings of the IEEE*, vol. 57, no. 8, pp. 1408–1418, Aug. 1969. (Cited on page 272.)

[208] D. Yocky, C. V. Jakowatz, and P. H. Eichel, "Interpolated Spatially Variant Apodization in Synthetic Aperture Radar Imagery," *Applied Optics*, vol. 39, no. 14, pp. 2310–2314, May 2000. (Cited on page 273.)

[209] B. H. Smith, "Generalization of spatially variant apodization to noninteger Nyquist

sampling rates." *IEEE Transactions on Image Processing*, vol. 9, no. 6, pp. 1088–93, Jan. 2000. (Cited on page 273.)

[210] C. Castillo-Rubio, S. Llorente-Romano, and M. Burgos-Garcia, "Robust SVA method for every sampling rate condition," *IEEE Transactions on Aerospace and Electronic Systems*, vol. 43, no. 2, pp. 571–580, Apr. 2007. (Cited on page 273.)

[211] R. Iglesias and J. J. Mallorqui, "Side-Lobe Cancelation in DInSAR Pixel Selection With SVA," *IEEE Geoscience and Remote Sensing Letters*, vol. 10, no. 4, pp. 667–671, Jul. 2013. (Cited on page 279.)

[212] W. H. Press, S. A. Teukolsky, W. T. Vetterling, and B. P. Flannery, *Numerical Recipes in C: The Art of Scientific Computing.* Cambridge University Press, 1992. (Cited on page 287.)

[213] J. J. Mallorqui, "Métodos numéricos para aplicaciones biomédicas: problemas directo e inverso electromagnéticos," Ph.D. dissertation, Universitat Politècnica de Catalunya, 1995. (Cited on page 296.)

[214] P. Blanco-Sánchez, "SAR differential interferometry for deformation monitoring under a multi-frequency approach," Ph.D. dissertation, Universitat Politècnica de Catalunya, 2009. (Cited on page 296.)

List of Publications

Journal Articles

[JA1] R. Iglesias, A. Aguasca, X. Fabregas, J. J. Mallorqui, D. Monells, C. López-Martínez, and L. Pipia, "Ground-Based Polarimetric SAR Interferometry for the Monitoring of Terrain Displacement Phenomena - Part I: Theoretical Description," *IEEE Journal of Selected Topics in Applied Earth Observations and Remote Sensing*, vol. 8, no. 3, pp. 980–993, Mar. 2015.

[JA2] ——, "Ground-Based Polarimetric SAR Interferometry for the Monitoring of Terrain Displacement Phenomena - Part II: Applications," *IEEE Journal of Selected Topics in Applied Earth Observations and Remote Sensing*, vol. 8, no. 3, pp. 994–1007, Mar. 2015.

[JA3] R. Iglesias, D. Monells, C. López-Martínez, J. J. Mallorqui, X. Fabregas, and A. Aguasca, "Polarimetric Optimization of Temporal Sublook Coherence for DInSAR Applications," *IEEE Geoscience and Remote Sensing Letters*, vol. 12, no. 1, pp. 87–91, Jan. 2015.

[JA4] R. Iglesias, J. J. Mallorqui, D. Monells, C. López-Martínez, X. Fabregas, A. Aguasca, J. A. Gili, and J. Corominas, "PSI Deformation Map Retrieval by Means of Temporal Sublook Coherence on Reduced Sets of SAR Images," *Remote Sensing*, vol. 7, no. 1, pp. 530–563, Jan. 2015.

[JA5] R. Iglesias, J. J. Mallorqui, and P. López-Dekker, "DInSAR Pixel Selection Based on Sublook Spectral Correlation Along Time," *IEEE Transactions on Geoscience and Remote Sensing*, vol. 52, no. 7, pp. 3788–3799, Jul. 2014.

[JA6] R. Iglesias, X. Fabregas, A. Aguasca, J. J. Mallorqui, C. López-Martínez, J. A. Gili, and J. Corominas, "Atmospheric Phase Screen Compensation in Ground-Based SAR With a Multiple-Regression Model Over Mountainous Regions," *IEEE Transactions on Geoscience and Remote Sensing*, vol. 52, no. 5, pp. 2436–2449, May 2014.

[JA7] R. Iglesias, D. Monells, X. Fabregas, J. J. Mallorqui, A. Aguasca, and C. López-Martínez, "Phase Quality Optimization in Polarimetric Differential SAR Interferometry," *IEEE Transactions on Geoscience and Remote Sensing*, vol. 52, no. 5, pp. 2875–2888, May 2014.

[JA8] D. Di Martire, R. Iglesias, D. Monells, G. Centolanza, S. Sica, M. Ramondini, L. Pagano, J. J. Mallorqui, and D. Calcaterra, "Comparison between Differential SAR interferometry and ground measurements data in the displacement monitoring of the earth-dam of Conza della Campania (Italy)," *Remote Sensing of Environment*, vol. 148, pp. 58–69, May 2014.

[JA9] R. Iglesias and J. J. Mallorqui, "Side-Lobe Cancelation in DInSAR Pixel Selection With SVA," *IEEE Geoscience and Remote Sensing Letters*, vol. 10, no. 4, pp. 667–671, Jul. 2013.

[JA10] M. Crosetto, O. Montserrat, R. Iglesias, and B. Crippa, "Persistent Scatterer Interferometry: Potential, Limits and Initial C- and X-band Comparison," *Photogrammetric engineering and remote sensing*, vol. 76, no. 9, pp. 1061–1069, Sep. 2010.

Conference Articles

[CA1] J. Duro, R. Iglesias, P. Blanco-Sánchez, D. Albiol, and F. Koudogbo, "PSI Wide Area Product (WAP) for measuring Ground Surface Displacements at regional level for multi-hazards studies," in *Proc. EGU General Assembly (EGU'15)*, Vienna (Austria), Apr. 2015.

[CA2] J. Duro, R. Iglesias, P. Blanco-Sánchez, D. Albiol, T. Wright, N. Adam, F. Rodriguez-Gonzalez, R. Brcic, A. Parizzi, F. Novali, and P. Bally, "Strategies for Measuring Large Scale Ground Surface Deformations: PSI Wide Area Product Approaches," in *Proc. 9th International Workshop on Advances in the Science and Applications of SAR Interferometry (FRINGE'15)*, Frascati (Rome, Italy), Mar. 2015.

[CA3] J. Duro, R. Iglesias, P. Blanco-Sánchez, and D. Albiol, "Improved PSI Performance for Landslide Monitoring Applications," in *9th International Workshop on Advances in the Science and Applications of SAR Interferometry (FRINGE'15)*, Frascati (Rome, Italy), Mar. 2015.

[CA4] D. Albiol, R. Iglesias, F. Sánchez, and J. Duro, "Improved Characterization of Slow-Moving Landslides by means of Adaptive NL-InSAR Filtering," in *Proc. SPIE SAR Image Analysis, Modeling, and Techniques XIV (SPIE'14)*, Amsterdam (Netherlands), Sep. 2014.

[CA5] J. Corominas, R. Iglesias, A. Aguasca, J. J. Mallorqui, X. Fabregas, X. Planas, and J. A. Gili, "Comparing Satellite Based and Ground Based Radar Interferometry and Field Observations at the Canillo Landslide (Pyrenees)," in *Proc. International IAEG Congress (IAEG'14)*, Torino (Italy), Sep. 2014.

[CA6] J. Fernández, M. Avellaneda, R. Iglesias, J. J. Mallorqui, E. Sansosti, and A. Morales, "Ground and Space Study and Control of the Leintz Gatzaga (Guipúzcoa, Spain) Landslide," in *Proc. IEEE International Geoscience and Remote Sensing Symposium (IGARSS'14)*, Quebec (Canada), Jul. 2014.

[CA7] R. Iglesias, D. Monells, G. Centolanza, J. J. Mallorqui, X. Fabregas, and A. Aguasca, "Down-slope Combination of Orbital and Ground-Based DInSAR

for the Efficient Monitoring of Slow-Moving Landslides," in *Proc. 10th European Conference on Synthetic Aperture Radar (EUSAR'14)*, Berlin (Germany), Jun. 2014.

[CA8] D. Monells, R. Iglesias, G. Centolanza, and J. J. Mallorqui, "Iterative Solution to Temporal Phase Wrapping in Differential SAR Interferometry for High Displacement Rate Phenomena," in *Proc. 10th European Conference on Synthetic Aperture Radar (EUSAR'14)*, Berlin (Germany), Jun. 2014.

[CA9] J. Corominas, R. Iglesias, A. Aguasca, J. J. Mallorqui, X. Fagregas, X. Planas, and J. A. Gili, "Consideraciones sobre el deslizamiento del Forn de Canillo (Princpipat d'Andorra) a partir de datos de Interferometría radar y nuevas obervaciones," in *Proc. VIII Simposio Nacional sobre Taludes y Laderas Inestables*, Palma de Mallorca (Spain), Jun. 2013.

[CA10] R. Iglesias, D. Monells, X. Fabregas, J. J. Mallorqui, A. Aguasca, and C. López-Martínez, "Phase Quality Optimization Techniques and Limitation in Polarimetric Differential SAR Interferometry," in *Proc. 6th International Workshop on Science and Applications of SAR Polarimetry and Polarimetric Interferometry (POLInSAR'13)*, Frascati (Rome, Italy), Jan. 2013.

[CA11] D. Monells, R. Iglesias, and J. J. Mallorqui, "Performance Comparison Between Dual Polarimetric and Fully Polarimetric Data for Differential SAR Interferometry Subsidence Monitoring," in *Proc. 6th International Workshop on Science and Applications of SAR Polarimetry and Polarimetric Interferometry (POLInSAR'13)*, Frascati (Rome, Italy), Jan. 2013.

[CA12] R. Iglesias, X. Fabregas, A. Aguasca, C. López-Martínez, A. Alonso-González, and J. J. Mallorqui, "Polarimetric Optimization for DInSAR Pixel Selection with Ground-Based SAR," in *Proc. IEEE International Geoscience and Remote Sensing Symposium (IGARSS'12)*, Munich (Germany), Jul. 2012.

[CA13] R. Iglesias, D. Monells, G. Centolanza, J. J. Mallorqui, X. Fabregas, and A. Aguasca, "Landslide Monitoring with Spotlight TerraSAR-X DATA," in *Proc. IEEE International Geoscience and Remote Sensing Symposium (IGARSS'12)*, Munich (Germany), Jul. 2012.

[CA14] D. Monells, R. Iglesias, J. J. Mallorqui, X. Fabregas, and C. López-Martínez, "Phase quality Optimization in Orbital Differential SAR Interferometry with Fully Polarimetric Data," in *Proc. IEEE International Geoscience and Remote Sensing Symposium (IGARSS'12)*, Munich (Germany), Jul. 2012.

[CA15] R. Iglesias, X. Fabregas, A. Aguasca, C. López-Martínez, and A. Alonso-Gonzalez, "Advanced Polarimetric Optimization for DInSAR Applications with Ground-Based SAR," in *Proc. 9th European Conference on Synthetic Aperture Radar (EUSAR'12)*, Nuremberg (Germany), Apr. 2012.

[CA16] R. Iglesias, D. Monells, G. Centolanza, J. J. Mallorqui, X. Fabregas, A. Aguasca, and C. López-Martínez, "Application of High Resolution Spotlight TerraSAR-X Data to Landslide Monitoring," in *Proc. 9th European Conference on Synthetic Aperture Radar (EUSAR'12)*, Nuremberg (Germany), Apr. 2012.

[CA17] X. Fabregas, R. Iglesias, and A. Aguasca, "A New Approach for Atmospheric

Phase Screen Compensation in Ground-Based SAR Over Areas With Steep Topography," in *Proc. 9th European Conference on Synthetic Aperture Radar (EUSAR'12)*, Nuremberg (Germany), Apr. 2012.

[CA18] G. Centolanza, R. Iglesias, D. Monells, and J. J. Mallorqui, "A New Approach to DInSAR Pixel Selection with a Combined Multi Resolution Selection Method," in *Proc. 9th European Conference on Synthetic Aperture Radar (EUSAR'12)*, Nuremberg (Germany), Apr. 2012.

[CA19] R. Iglesias, D. Monells, G. Centolanza, J. J. Mallorqui, and P. López-Dekker, "A New Approach to DInSAR Pixel Selection with Spectral Correlation Along Time Between Sublooks," in *Proc. European Conference on Synthetic Aperture Radar (EUSAR'12)*, Nuremberg (Germany), Apr. 2012.

[CA20] X. Fabregas, R. Iglesias, A. Aguasca, and J. A. Gili, "2D Atmospheric Artifact Compensation with Multiple Regression Model in Ground-Based SAR over Mountainous Areas," in *Proc. 7th International Workshop on Advances in the Science and Applications of SAR Interferometry (FRINGE'11)*, Frascati (Rome, Italy), Sep. 2011.

[CA21] R. Iglesias, D. Monells, G. Centolanza, and J. J. Mallorqui, "DInSAR Pixel Selection Based on Spectral Correlation Along Time Between Sublooks," in *Proc. 7th International Workshop on Advances in the Science and Applications of SAR Interferometry (FRINGE'11)*, Frascati (Rome, Italy), Sep. 2011.

[CA22] G. Centolanza, R. Iglesias, D. Monells, and J. J. Mallorqui, "A New Approach in DInSAR Pixel Selection with a Combined Multi Resolution Selection Method," in *Proc. 7th International Workshop on Advances in the Science and Applications of SAR Interferometry (FRINGE'11)*, Frascati (Rome, Italy), Sep. 2011.

[CA23] J. J. Mallorqui, A. Aguasca, A. Broquetas, X. Fabregas, C. López-Martínez, A. Alonso-Gonzalez, G. Centolanza, R. Iglesias, and D. Monells, "Differential SAR Interferometry with Orbital, Airborne and Ground-Based Sensors," in *Proc. SAR Technologies and Applications Congress*, Madrid (Spain), May 2011.

[CA24] M. Crosetto, O. Monserrat, and R. Iglesias, "PSI Validation Results and Open Issues," in *Proc. 6th International Workshop on Advances in the Science and Applications of SAR Interferometry (FRINGE'09)*, Frascati (Rome, Italy), Dec. 2009.

[CA25] O. Monserrat, M. Crosetto, R. Iglesias, G. Rossi, L. Calcagni, and B. Crippa, "A Tool for 2+1D Phase Unwrapping: Application Examples," in *Proc. 6th International Workshop on Advances in the Science and Applications of SAR Interferometry (FRINGE'09)*, Frascati (Rome, Italy), Dec. 2009.